

**Digital Image Correlation to Evaluate Plastic Shrinkage Cracking in Cement-
Based Materials**

Pengfei Zhao

A Thesis

in

The Department

of

Building, Civil, and Environmental Engineering

Presented in Partial Fulfillment of the Requirements

for the Degree of Master of Applied Science (Civil Engineering) at

Concordia University

Montreal, Quebec, Canada

July 2016

© Pengfei Zhao, 2016

CONCORDIA UNIVERSITY
School of Graduate Studies

This is to certify that the thesis prepared

By: Pengfei Zhao

Entitled: Digital Image Correlation to Evaluate Plastic Shrinkage Cracking in Cement-
Based Materials

and submitted in partial fulfillment of the requirements for the degree of

Master of Applied Science (Civil Engineering)

complies with the regulations of the University and meets the accepted standards with respect to
originality and quality.

Signed by the final Examining Committee:

<u>Dr. Theodore Stathopoulos</u>	Chair
<u>Dr. Suong Van Hoa</u>	Examiner
<u>Dr. Hua Ge</u>	Examiner
<u>Dr. Michelle Nokken</u>	Co-Supervisor
<u>Dr. Attila Michael Zsaki</u>	Co-Supervisor

Approved by

Chair of Department or Graduate Program Director

July 2016

Dean of Faculty

ABSTRACT

Digital Image Correlation to Evaluate Plastic Shrinkage Cracking in Cement-Based

Materials

Pengfei Zhao

Fresh concrete exposed to a drying environment is susceptible to plastic shrinkage cracking, which could result in negative impacts on concrete durability. In the current ASTM standard, plastic shrinkage cracking is evaluated by the average crack width measured at 24 hours after concrete placement, considering that the traditional crack measurement tools cannot be used on fresh concrete. In this project, a non-contact strain measurement technique based on digital image correlation (DIC) was applied to study the behavior of plastic shrinkage cracking. In the experimental program, the effects of air temperature, wind velocity, water to cement ratio (w/c), and substrate roughness on plastic shrinkage cracking were investigated. Several cement paste specimens were tested separately in a controlled environmental chamber. A series of digital images was taken above the specimen surface throughout each experiment. DIC analysis was then performed on these images. The crack areas were also determined based on the images using MATLAB functions. It was found that DIC can provide a series of strain contour maps that helped to understand the process of plastic shrinkage cracking. The accumulations of tensile and compressive strains can be used to illustrate the cracking intensity and the overall shrinkage, respectively. The evolutions of the maximum tensile and compressive strains can be used to indicate the time to first crack and the shrinkage capacity, respectively. The effects of air temperature, wind velocity, w/c, and substrate roughness were well explained by both the DIC analysis results and crack areas computed in MATLAB.

ACKNOWLEDGEMENTS

First and foremost, I would like to express my gratitude to my supervisors, Dr. Michelle Nokken and Dr. Attila Michael Zsaki, for their contributions of time, ideas, and funding to make this project possible. Thanks for giving me a lot of inspiration on how to become an excellent researcher.

My special thanks go to Dr. Suong Van Hoa for letting me use the image correlation software VIC-2D at Concordia Centre for Composites. The support from the lab manager Mr. Heng Wang is also deeply appreciated.

I would like to extend my thanks to the technician Mr. Mark Elie of Engineering Materials Lab for offering me the materials. Thanks to Sajjad Mirvalad and Javad Mirvalad for the fun discussions and the help they provided me in the lab.

Finally, I am deeply grateful to my parents for their love, encouragement, and support.

Table of Contents

List of Figures	viii
List of Tables	xiv
1 INTRODUCTION	1
1.1 Background	1
1.2 Problem statement	5
1.3 Objectives	6
1.4 Significance of research	7
2 LITERATURE REVIEW	8
2.1 Introduction	8
2.2 Early volume change of concrete	8
2.3 Mechanism of plastic shrinkage cracking	10
2.4 Influencing factors of plastic shrinkage cracking	14
2.4.1 Influence of environmental conditions	15
2.4.2 Influence of concrete mixture ingredients and proportions	17
2.5 Restrained plastic shrinkage testing techniques	21
2.5.1 Ring test	21
2.5.2 Longitudinal tests	22
2.5.3 Slab tests	24
2.5.4 Substrate restraint tests	25
2.6 Image analysis techniques	31
2.6.1 Scanning electron microscope (SEM)	31
2.6.2 Crack border detection	32
2.6.3 Particle tracking	37

2.6.4	Digital image correlation (DIC)	41
2.7	Summary	44
3	EXPERIMENTAL PROGRAM	45
3.1	Introduction	45
3.2	Materials	46
3.3	Environmental conditions	46
3.4	Camera specifications	47
3.5	Water evaporation tests	48
3.6	ASTM standard C1579 procedure	49
3.6.1	Specimen geometry	49
3.6.2	Testing procedure	49
3.7	Cement paste testing procedure	51
3.7.1	Specimen geometry	51
3.7.2	Testing procedure	51
3.8	Image analysis techniques	52
3.8.1	MATLAB script to determine crack area	53
3.8.2	VIC-2D	56
4	RESULTS AND DISCUSSION	58
4.1	Introduction	58
4.2	Evaluation of the water evaporation equation	58
4.3	Effect of spray paint on water evaporation rate	61
4.4	Evaluation of the process of plastic shrinkage cracking	62
4.5	Effect of air temperature on plastic shrinkage cracking	75
4.6	Effect of wind velocity on plastic shrinkage cracking	84

4.7	Effect of w/c on plastic shrinkage cracking	92
4.8	Effect of substrate roughness on plastic shrinkage cracking	96
4.9	Evaluation of ASTM Standard C1579 geometry	101
5	CONCLUSIONS AND FUTURE WORK	106
5.1	Conclusions	106
5.2	Suggestions for future work	108
6	REFERENCES	111
	APPENDIX A	119
	APPENDIX B	120

List of Figures

Figure 1.1. Different types of cracking in a hypothetical concrete structure (Mehta and Monteiro, 2006).	2
Figure 1.2. Wind rose plot for Montreal-Trudeau Airport in July during 1971-2000 (Rose des vents, Montréal P. E. Trudeau, Annuel 1971-2000, n.d.).	4
Figure 2.1. Schematic diagrams of chemical shrinkage (a) and self-desiccation shrinkage (b): (1) cement particle, (2) pore water, (3) hydration product, and (4) internal void (Gao et al., 2014). ..	9
Figure 2.2. Developments of plastic shrinkage, settlement, and evaporation in a freshly placed concrete specimen exposed to a drying environment (Turcry and Loukili, 2006).	11
Figure 2.3. Schematic diagram of capillary pressure build-up (Slowik et al., 2008).	13
Figure 2.4. Electron microscope images of a freshly mixed fly ash paste upon drying, 300X (Slowik et al., 2008).	14
Figure 2.5. Effect of concrete and air temperatures, relative humidity, and wind velocity on the rate of evaporation of surface moisture from concrete (ACI 305R-10, 2010).	16
Figure 2.6. Effect of w/c and cement contents on the time to first crack (Almusallam et al., 1998).	18
Figure 2.7. Effect of w/c and cement contents on crack area (Almusallam et al., 1998).	19
Figure 2.8. Effect of coarse aggregate on plastic shrinkage cracking (Banthia and Gupta, 2009).	20
Figure 2.9. Diagram of ring geometry with ribs under air funnel (Bjøntegaard et al., 1998).	22
Figure 2.10. Diagram of longitudinal geometry with triple-bar anchors (Banthia et al., 1995). ..	23
Figure 2.11. Diagram of longitudinal geometry with anchor bolts and a center riser (Mora et al., 2009).	23

Figure 2.12. Diagram of thin slab test with electrical fans (Shaeles and Hover, 1988).	24
Figure 2.13. Diagram of slab test using stud bolts at four ends (Yokoyama et al., 1994).	25
Figure 2.14. Diagram of substrate restraint type test using half exposed aggregate (Banthia et al., 1996).	26
Figure 2.15. Diagram of substrate with uniform semicircle protrusions (Banthia and Gupta, 2006).	27
Figure 2.16. Diagram of plastic shrinkage cracking test setup using a substrate with a grooved structure (Naaman et al., 2005).	28
Figure 2.17. Diagram of specimen mold and stress risers (ASTM Standard C1579-13, 2013). ..	29
Figure 2.18. Diagram of environmental chamber (ASTM Standard C1579-13, 2013).	30
Figure 2.19. Intensity of each RGB component along a typical crack cross-section (Barazzetti and Scaioni, 2009).	33
Figure 2.20. Image analysis procedure: (a) image acquisition, (b) image processing, (c) crack feature determination, and (d) crack measurement (Qi et al., 2003).	34
Figure 2.21. Image processing procedure: (a) grayscale image, (b) intensity distribution histogram, and (c) binary image after cleaning (Qi et al., 2003).	35
Figure 2.22 Crack widths measured by image analysis and optical microscope (Qi et al., 2005).	36
Figure 2.23. Crack area determined by counting the pixels inside the crack (Banthia and Gupta, 2009).	37
Figure 2.24. Steel pin targets for image analysis (Ong and Myint-Lay, 2006).	38
Figure 2.25. Diagram of specimen mold and locations of targets (Ong and Myint-Lay, 2006)...	38

Figure 2.26. Orientation frame and a pair of targets placed on both sides of a crack (Barazzetti and Scaioni, 2009).	39
Figure 2.27. Displacement between targets (Barazzetti and Scaioni, 2009).	40
Figure 2.28. Schematic diagram of the reference and the deformed subimages in an image (Alam et al., 2012).	41
Figure 2.29. Deformation obtained from DIC and LVDT (Choi and Shah, 1997).....	42
Figure 2.30. Apertures in image matching: (a) matching problem, (b) unique matching by placing apertures (Sutton et al., 2009).	43
Figure 3.1. Diagram of test setup.....	47
Figure 3.2. Specimen form with stress risers.....	49
Figure 3.3. Image processing procedure using MATLAB: (a) original image, (b) grayscale image, (c) binary image, (d) cleaned image.....	54
Figure 3.4. Binary images obtained using the level values of 0.25, 0.30, 0.35, and 0.40.	55
Figure 3.5. Partial enlarged view of a speckled image with a grid of 63×63 pixels.....	57
Figure 4.1. Water evaporation rates calculated by mass loss and the water evaporation equation in the first 6 hours.	59
Figure 4.2. Air and concrete temperatures in the first 6 hours.	60
Figure 4.3. Water evaporation rates of the concrete specimens with and without spray paint in the first 6 hours.	61
Figure 4.4. Crack area of the cement paste specimen with the w/c 0.40 over time.....	63
Figure 4.5. Original image (a), binary image (b), contour map of e_{xx} on the cement paste surface (c), and e_{xx} on the horizontal line (d) at the beginning of the experiment.	65

Figure 4.6. Original image (a), binary image (b), contour map of e_{xx} on the cement paste surface (c), and e_{xx} on the horizontal line (d) at 10 minutes after starting the experiment.	66
Figure 4.7. Original image (a), binary image (b), contour map of e_{xx} on the cement paste surface (c), and e_{xx} on the horizontal line (d) at 28 minutes after starting the experiment.	67
Figure 4.8. Original image (a), binary image (b), contour map of e_{xx} on the cement paste surface (c), and e_{xx} on the horizontal line (d) at 30 minutes after starting the experiment.	68
Figure 4.9. Original image (a), binary image (b), contour map of e_{xx} on the cement paste surface (c), and e_{xx} on the horizontal line (d) at 32 minutes after starting the experiment.	69
Figure 4.10. Original image (a), binary image (b), contour map of e_{xx} on the cement paste surface (c), and e_{xx} on the horizontal line (d) at 34 minutes after starting the experiment.	70
Figure 4.11. Original image (a), binary image (b), contour map of e_{xx} on the cement paste surface (c), and e_{xx} on the horizontal line (d) at 40 minutes after starting the experiment.	71
Figure 4.12. Original image (a), binary image (b), contour map of e_{xx} on the cement paste surface (c), and e_{xx} on the horizontal line (d) at 90 minutes after starting the experiment.	72
Figure 4.13. Developments of three peak e_{xx} on the horizontal line and crack area over time. ...	73
Figure 4.14. Original image and contour map of major principal strains at the termination of the experiment.....	75
Figure 4.15. Binary image of the speckle pattern of the cement paste specimen exposed to the high air temperature at the beginning of the experiment.	77
Figure 4.16. Crack areas of the cement paste specimens exposed to three different air temperatures over time.....	79
Figure 4.17. Maximum and minimum strains in the x-direction of the cement paste specimens exposed to three different air temperatures over time.	80

Figure 4.18. Contour maps of e_{xx} of the cement paste specimens exposed to (a) room temperature, (b) medium air temperature, and (c) high air temperature at the termination of the experiments.	83
Figure 4.19. Crack areas of the cement paste specimens exposed to three different wind velocities over time.	86
Figure 4.20. Crack contours of the cement paste specimen exposed to the low wind velocity at the termination of the experiment.	87
Figure 4.21. Maximum and minimum strains in the x-direction of the cement paste specimens exposed to three wind velocities over time.	89
Figure 4.22. Contour maps of e_{xx} of the cement paste specimens exposed to (a) low wind velocity, (b) medium low velocity, and (c) high wind velocity at the termination of the experiments.	91
Figure 4.23. Crack areas of the cement paste specimens with different w/c over time.	93
Figure 4.24. Maximum and minimum strains in the x-direction of the cement paste specimens with different w/c over time.	95
Figure 4.25. Crack areas of the cement paste specimens cast on three different substrate conditions over time.	98
Figure 4.26. Maximum and minimum strains in the x-direction of the cement paste specimens cast on three different substrate conditions over time.	100
Figure 4.27. Contour map of e_{xx} on the concrete surface at the beginning of the experiment. ..	101
Figure 4.28. Contour map of e_{xx} on the concrete surface at 30 minutes after starting the experiment.	102

Figure 4.29. Contour map of ϵ_{xx} on the concrete surface at 90 minutes after starting the experiment..... 102

Figure 4.30. Contour map of ϵ_{xx} on the concrete surface at 360 minutes after starting the experiment..... 103

Figure 4.31. Maximum and minimum strains in the x-direction of the concrete specimen over time. 104

List of Tables

Table 3.1. Concrete mixture proportions.	50
Table 4.1. Average air temperature, relative humidity, and wind velocity during the experiments for the cement paste specimens exposed to three different air temperatures.	76
Table 4.2. Speckle coverages of the cement paste specimens exposed to three different air temperatures.	77
Table 4.3. Average air temperature, relative humidity, and wind velocity during the experiments for the cement paste specimens exposed to three different wind velocities.	85
Table 4.4. Speckle coverages of the cement paste specimens exposed to three different wind velocities.	85
Table 4.5. Speckle coverages of the cement paste specimens with different w/c.	92
Table 4.6. Speckle coverages of the cement paste specimens cast on three different substrate conditions.	97
Table B.1. Air and concrete temperatures, relative humidity, wind velocity, the mass of concrete, and the water evaporation rates calculated by mass loss and the water evaporation equation during the experiment for the concrete specimen without spray paint.	120
Table B.2. Air and concrete temperatures, relative humidity, wind velocity, the mass of concrete, and the water evaporation rates calculated by mass loss and the water evaporation equation during the experiment for the concrete specimen with spray paint.	121
Table B.3. Environmental variables and the water evaporation rates calculated by the water evaporation equation during the experiment for the cement paste specimen exposed to the room temperature.	122

Table B.4. Environmental variables and the water evaporation rates calculated by the water evaporation equation during the experiment for the cement paste specimen exposed to the medium air temperature.	122
Table B.5. Environmental variables and the water evaporation rates calculated by the water evaporation equation during the experiment for the cement paste specimen cast on No. 180 sandpaper, and exposed to the high air temperature and high wind velocity.	123
Table B.6. Environmental variables and the water evaporation rates calculated by the water evaporation equation during the experiment for the cement paste specimen exposed to the low wind velocity.....	123
Table B.7. Environmental variables and the water evaporation rates calculated by the water evaporation equation during the experiment for the cement paste specimen exposed to the medium wind velocity.....	124
Table B.8. Environmental variables and the water evaporation rates calculated by the water evaporation equation during the experiment for the cement paste specimen with the w/c of 0.35.	124
Table B.9. Environmental variables and the water evaporation rates calculated by the water evaporation equation during the experiment for the cement paste specimen with the w/c of 0.40.	125
Table B.10. Environmental variables and the water evaporation rates calculated by the water evaporation equation during the experiment for the cement paste specimen with the w/c of 0.45.	125

Table B.11. Environmental variables and the water evaporation rates calculated by the water evaporation equation during the experiment for the cement paste specimen with the w/c of 0.50.

..... 126

Table B.12. Environmental variables and the water evaporation rates calculated by the water evaporation equation during the experiment for the cement paste specimen cast on duct tape. 126

Table B.13. Environmental variables and the water evaporation rates calculated by the water evaporation equation during the experiment for the cement paste specimen cast on No. 40 sandpaper. 127

1 INTRODUCTION

1.1 Background

Concrete is a composite material that is mainly made up of water, cement, and aggregates. It is known as the most widely used construction material in the world due to its versatility, durability, and economy. In recent decades, considering the inconvenience and high expenses associated with the maintenance and repair of concrete structures, there has been a great research interest in improving the performance and durability of concrete materials.

A major factor that negatively affects the performance and durability of concrete is the frequently observed surface cracking in concrete structures, as shown in Figure 1.1. Cracking in concrete is a common problem which has been recognized worldwide. According to its principal causes, cracking in concrete can be categorized into structural cracking which is mainly caused by applied loading, and non-structural cracking which results from concrete mixture proportions and properties as well as its external environmental conditions and construction practices.

Unlike structural cracking, the occurrence of non-structural cracking generally does not result in structural failure, but it absolutely reduces the service life of a concrete structure. Some types of non-structural cracking may allow the ingress of aggressive agents to the embedded reinforcing steel in concrete, thus leading to the corrosion of the reinforcing steel which causes possible further cracking and spalling in concrete structures.

Non-structural cracking can be observed in concrete both in its plastic state and hardened state. Plastic settlement cracking (A, B and C in Figure 1.1) and plastic shrinkage cracking (D, E and F in Figure 1.1) are two types of pre-hardening cracking that are often observed in freshly placed

concrete elements. Pre-hardening cracking usually occurs within a few hours after concrete placement, and before concrete has reached final set. It is widely accepted that plastic settlement is mainly the result of excessive bleeding, while plastic shrinkage is mainly caused by the rapid surface drying. Cracking occurs when plastic settlement and plastic shrinkage are restrained before fresh concrete has developed sufficient tensile strength to resist this cracking.

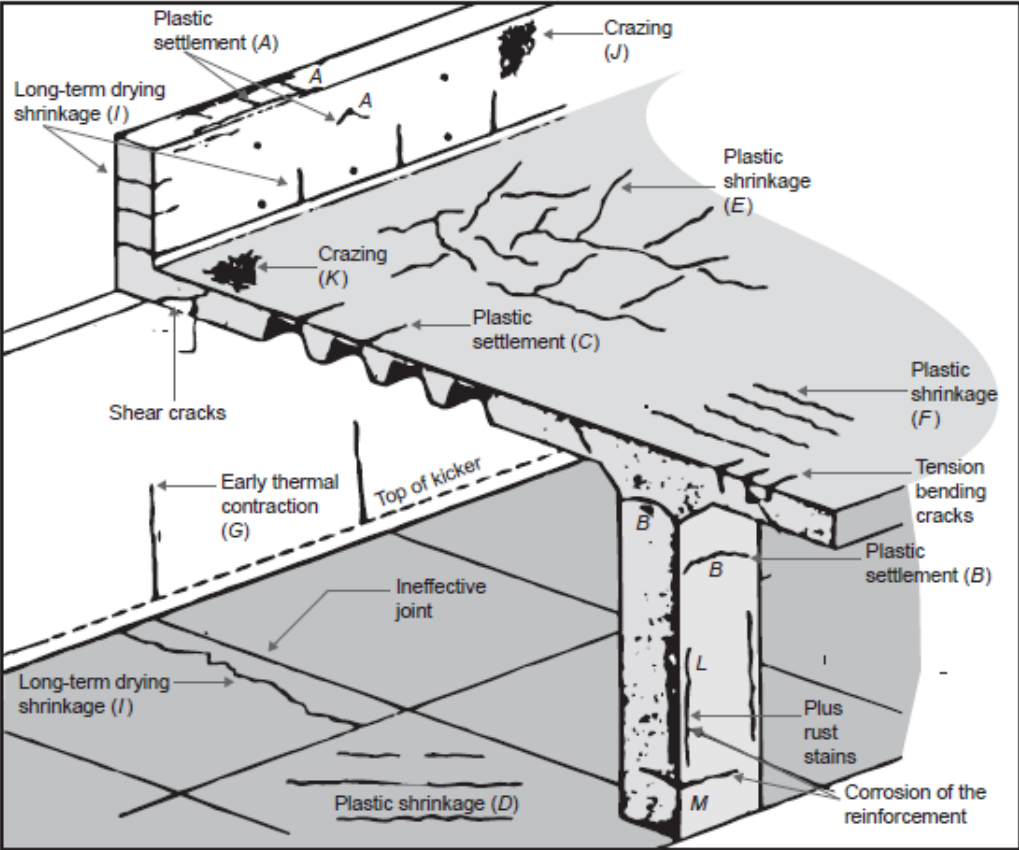


Figure 1.1. Different types of cracking in a hypothetical concrete structure (Mehta and Monteiro, 2006).

All freshly placed concrete elements exposed to a drying environment are susceptible to plastic shrinkage cracking. Plastic shrinkage cracking is usually associated with hot weather concreting. ACI Committee 305 defines “hot weather” as “one or a combination of the following conditions

that tends to impair the quality of freshly mixed or hardened concrete by accelerating the rate of moisture loss and rate of cement hydration, or otherwise causing detrimental results: high ambient temperature; high concrete temperature; low relative humidity; and high wind speed". When wind velocity exceeds 8 km/h, the risk of plastic shrinkage cracking is significantly elevated, and precautions should be applied to concrete elements (Scanlon, 1987). According to the wind rose plot for Montreal-Trudeau Airport in July during 1971-2000, the frequency of wind velocity above 10 km/h was about 56%, as shown in Figure 1.2. The average daily maximum temperature and the highest daily maximum temperature in July during 1981-2010 at Montreal-Trudeau Airport were 26.3 °C and 35.6 °C, respectively (Canadian Climate Normals 1981-2010 Station Data, 2015). The combined windy and hot weather during the summer season in Montreal therefore puts cast-in-place concrete in a great risk of plastic shrinkage cracking.

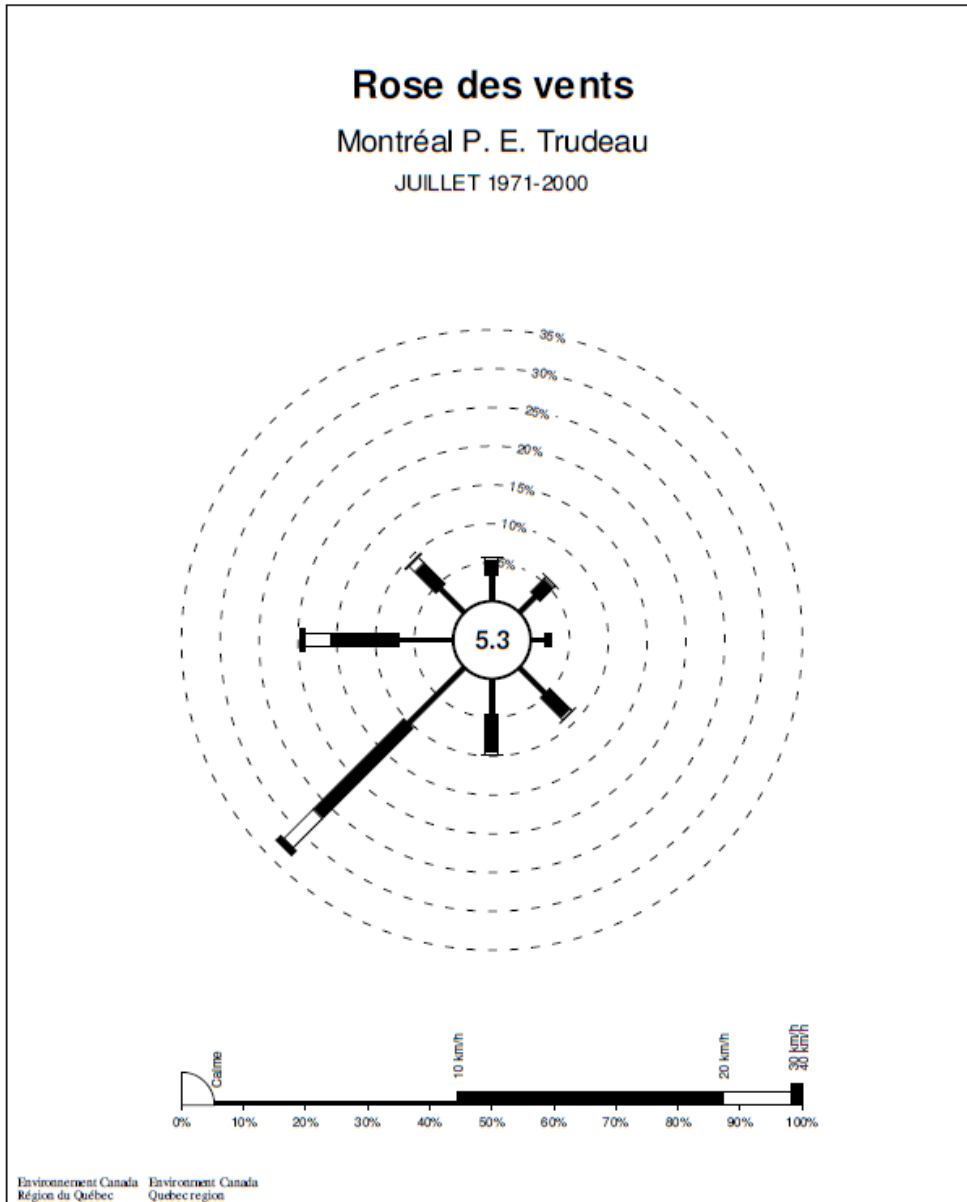


Figure 1.2. Wind rose plot for Montreal-Trudeau Airport in July during 1971-2000 (Rose des vents, Montréal P. E. Trudeau, Annuel 1971-2000, n.d.).

With the growing demand of concrete repair and widespread use of high performance concrete, today's concrete usually has a higher cement content, supplementary cementitious materials, and a lower water to cement ratio (w/c), and is sometimes subjected to a high level of restraint in the

case of concrete repair. These factors make today's concrete more sensitive to plastic shrinkage cracking when exposed to a drying environment. Thus, recent research has been focusing on investigating plastic shrinkage cracking in fresh concrete in order to improve the performance and durability of concrete materials.

1.2 Problem statement

Currently, the only existing ASTM standard related to plastic shrinkage cracking is ASTM Standard C1579. To reduce the risk of plastic shrinkage cracking, a widely accepted solution is to add short and randomly distributed fibers to concrete. In 2006, ASTM Standard C1579 was introduced to evaluate the effect of fibers on reducing plastic shrinkage cracking in concrete materials. In ASTM Standard C1579, a freshly placed fiber reinforced concrete specimen and a plain concrete specimen are prepared in a prescribed manner. The concrete specimens are then exposed to a uniform drying environment to induce cracking. During the experiment, the time to first crack for each specimen is recorded. At 24 hours after starting the experiment, the crack widths are measured at 10 mm intervals along the crack paths on both specimens. The effect of fibers on reducing plastic shrinkage cracking is evaluated by comparing the average crack widths.

Considering traditional crack measurement tools, such as optical hand-held microscope or crack comparator, which may disturb the cracking process in fresh concrete, the crack widths in ASTM Standard C1579 are measured at 24 hours after starting the experiment when concrete is considered stable. However, the crack widths measured at 24 hours after concrete placement may not be appropriate to evaluate the risk of plastic shrinkage cracking in some concrete mixtures. For example, high performance concrete with a relatively low w/c has proved to be more vulnerable to plastic shrinkage cracking because of having less bleeding water. In a severe drying environment,

concrete mixtures with lower w/c crack earlier, but the average crack widths are smaller than those of higher w/c concrete mixtures (Almusallam et al., 1998). Thus, in order to accurately evaluate plastic shrinkage cracking in concrete materials, the formation of plastic shrinkage cracking and the cracking process should be recorded and analyzed.

1.3 Objectives

In recent years, image analysis has been widely applied to cracking assessment due to its non-contact manner, reliable results, high precision, and efficiency. In ASTM Standard C1579, it is also recommended that the crack widths at 24 hours can be measured by an image analysis system.

Digital image correlation (DIC) is an easy to use image analysis technique, which can take full-field strain measurements on an object surface. DIC has been successfully applied to analyze the cracking propagation in hardened concrete under loading. It can provide accurate and detailed information (Gencturk et al., 2014). So far, no work has been reported on analyzing the behavior of plastic shrinkage cracking in fresh concrete by using this advanced technique.

The objectives of this project are:

1. To analyze the propagation of plastic shrinkage cracking in cement-based materials using the DIC technique.
2. To evaluate the effects of air temperature, wind velocity, w/c, and substrate roughness on plastic shrinkage cracking.
3. To substantiate results obtained by DIC using those obtained by image analysis of crack area.

1.4 Significance of research

The DIC analysis results combined with the crack area obtained by image analysis can produce a more comprehensive understanding of the process of plastic shrinkage cracking. Researchers will benefit from the detailed information that DIC provides when evaluating the risk of plastic shrinkage cracking in cement-based materials.

2 LITERATURE REVIEW

2.1 Introduction

This chapter describes different types of early shrinkage in concrete materials, the mechanism of plastic shrinkage cracking, and factors contributing to plastic shrinkage cracking as well as four types of restrained plastic shrinkage cracking testing techniques and currently available image analysis systems for cracking assessment.

2.2 Early volume change of concrete

Volume change of concrete begins immediately after it is cast due to gravity, cement hydration, and its external environment (Bentz, 2008). Early volume change, especially in the first few hours after placement, can have a significant impact on the performance and durability of hardened concrete due to the detrimental cracks induced at this time. In the following paragraphs, different types of early volume change are briefly described.

Chemical shrinkage: Chemical shrinkage refers to the absolute volume change that results from cement hydration. As cement hydrates, the hydration products occupy less absolute volume than the water and cement before their reaction, as shown in Figure 2.1 (a). Chemical shrinkage is a continuous feature of cement-based materials, and occurs as long as cement hydrates. After initial set, cement paste becomes stiff and difficult to deform; therefore, chemical shrinkage is compensated by the formation of internal voids in the cement paste. The presence of these internal voids does not significantly change the dimensions of a concrete element (Kosmatka et al., 2002).

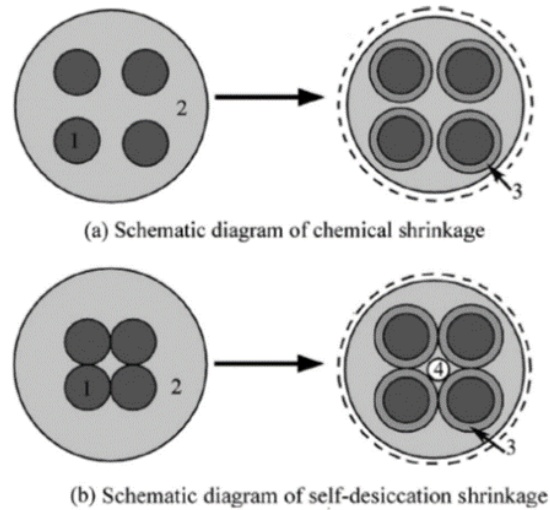


Figure 2.1. Schematic diagrams of chemical shrinkage (a) and self-desiccation shrinkage (b): (1) cement particle, (2) pore water, (3) hydration product, and (4) internal void (Gao et al., 2014).

Autogenous shrinkage: Autogenous shrinkage refers to the apparent volume change that occurs when concrete has no moisture and thermal exchange with an external medium (Mehta and Monteiro, 2006). Autogenous shrinkage is mainly caused by chemical shrinkage and self-desiccation shrinkage (Kosmatka et al., 2002). As discussed above, after initial set, hardened structures are formed in the cement paste as a result of cement hydration, and continuous chemical shrinkage results in the formation of internal voids in the cement paste, as shown in Figure 2.1 (b). In the meanwhile, pore water is continuously consumed by cement hydration, thus leading to the formation of a water–air meniscus in the internal void. A capillary pressure is then generated in the pore water and consequently compresses the internal void. The volume change caused by the capillary pressure compressing the internal voids is referred to as self-desiccation shrinkage (Gao et al., 2014). In the case of high performance concrete with a relatively low w/c and high cement content, autogenous shrinkage is evident which may lead to early cracking (Bentz, 2008).

Plastic Settlement: Plastic settlement refers to the vertical volume change of a freshly placed concrete element before initial set. It is mainly attributed to gravity (bleeding and the expulsion of air voids) and chemical shrinkage. In practice, plastic settlement cracking is often observed in concrete structures with insufficient consolidation of fresh concrete or above embedded reinforcing steel (Kosmatka et al., 2002).

Plastic shrinkage: Plastic shrinkage refers to the volume change when concrete is fluid and plastic. Plastic shrinkage occurs within the first few hours after placement and before final set. Plastic shrinkage results from a combination effect of the rapid surface drying, chemical shrinkage, autogenous shrinkage (Kosmatka et al., 2002), and plastic settlement (Qi et al., 2003).

2.3 Mechanism of plastic shrinkage cracking

The process of plastic shrinkage can be divided into three phases based on the curves of plastic shrinkage and settlement in a freshly placed concrete specimen that was exposed to a drying environment (Turcry and Loukili, 2006), as shown in Figure 2.2. In phase 1, a large settlement was observed while the horizontal shrinkage began to grow. In phase 2, the increase of settlement was relatively small when compared with the horizontal shrinkage which had a significant increase. In phase 3, the curves of settlement and shrinkage were gradually flattened, indicating that the volume change slowed down.

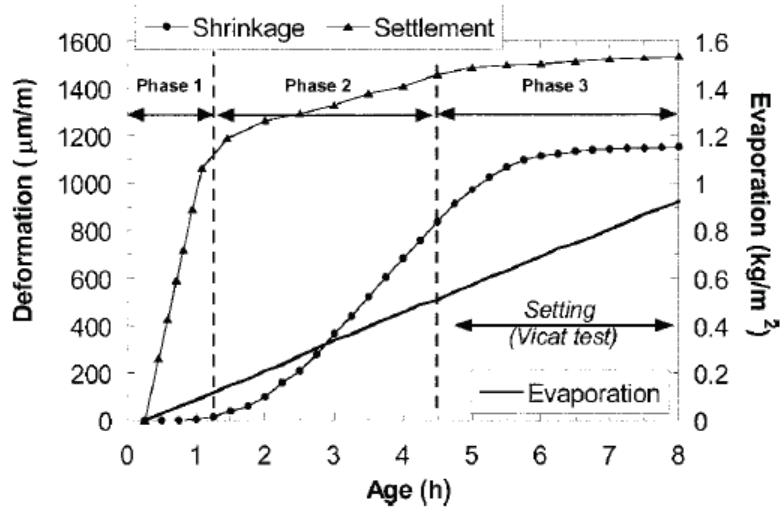


Figure 2.2. Developments of plastic shrinkage, settlement, and evaporation in a freshly placed concrete specimen exposed to a drying environment (Turcry and Loukili, 2006).

This process is commonly explained as the development of a capillary pressure near the top surface of concrete due to the rapid surface drying (Qi et al., 2005). Figure 2.3 schematically shows the process of capillary pressure build-up in a fresh concrete element upon drying. When concrete is cast, solid particles (cement and aggregates) begin to settle due to gravity. A layer of water is then formed on the top surface of fresh concrete. This process is referred to as bleeding (Aldalinsi et al., 2013; Kosmatka et al., 2002), as shown in Figure 2.3 A.

If the fresh concrete element is exposed to a severe drying environment where the water evaporation rate exceeds the bleeding rate of concrete, the thickness of water layer on the top surface of fresh concrete is continuously reduced. Consequently, the solid particles on the top surface are not fully covered by water, thus forming several water-air menisci between the solid particles. A capillary pressure is then developed in the capillary water according to the Young-Laplace equation (Bentz, 2008):

$$p_c = \frac{2\gamma \cos \alpha}{r}$$

Equation 1

Where,

p_c = capillary pressure, Pa;

γ = surface tension of the pore solution, N/m;

α = contact angle between the pore solution and the capillary pore walls, degrees;

r = meniscus radius, m.

The solid particles near the top surface of concrete are then compressed by the capillary pressure. However, at this point, the capillary pressure is relatively low; therefore, no horizontal shrinkage occurs (Aldalinsi et al., 2013), as shown in Figure 2.3 B. This process corresponds to Phase 1 in Figure 2.2.

With the further evaporation of capillary water, the meniscus radius and the contact angle between the capillary water and the solid particles decrease constantly. According to the Young-Laplace equation (Equation 1), capillary pressure p_c increases with a drop in meniscus radius r and contact angle between the pore solution and the capillary pore walls α . The increasing capillary pressure results in continuously compressing the solid particles near the top surface of concrete. Accordingly, the amount of horizontal shrinkage increases, as indicated in Phase 2 in Figure 2.2. This process is referred to as capillary pressure build-up, as shown in Figure 2.3 C.

With the continuous drying of capillary water, the menisci between the solid particles near the top surface of concrete disappear gradually, and the gaps between the solid particles are then penetrated by air. As a result, the capillary pressure drops dramatically. The peak capillary pressure

is defined as the “break-through” pressure (Wittmann, 1976), as shown in Figure 2.3 D. The solid particles are then not compressed by the capillary pressure (Aldalinsi et al., 2013). This process can be interpreted as a shrinkage limit (Saliba et al., 2011), which corresponds to Phase 3 in Figure 2.2.

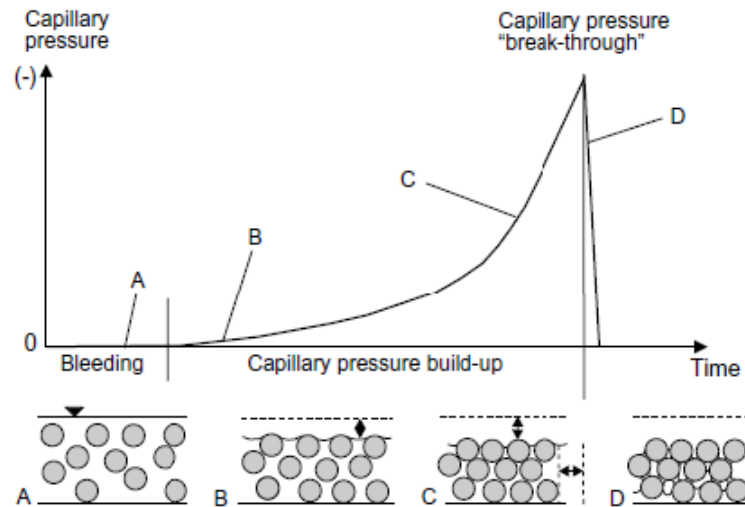


Figure 2.3. Schematic diagram of capillary pressure build-up (Slowik et al., 2008).

When air starts to penetrate the gaps between the solid particles, the risk of plastic shrinkage cracking is considered to reach its maximum (Slowik et al., 2008). At this point, the solid particles at the top surface are no longer bridged by water; therefore, weak points are formed on these locations. In the meanwhile, the part of concrete near the top surface has more shrinkage potential than the part that is still filled with water. In practice, plastic shrinkage could also be restrained by structures, such as foundations, subgrades, or embedded reinforcing steel. The non-homogeneous shrinkage can cause a strain localization developing on the top surface, which may lead to possible cracking.

The cracking process is illustrated by a series of electron microscope images that was taken above a fresh fly ash paste upon drying (Slowik et al., 2008). As shown in Figure 2.4, the first image was somewhat blurry, indicating that there was a thin layer of water on the top surface. With the further drying of surface water, the solid particles were more distinct in the second image. In the third image, some black spots can be seen on the right side of the image as a result of the penetration of air into the gaps between the solid particles. The fourth image was taken right after the third one, which had a crack that was formed on the weak points.

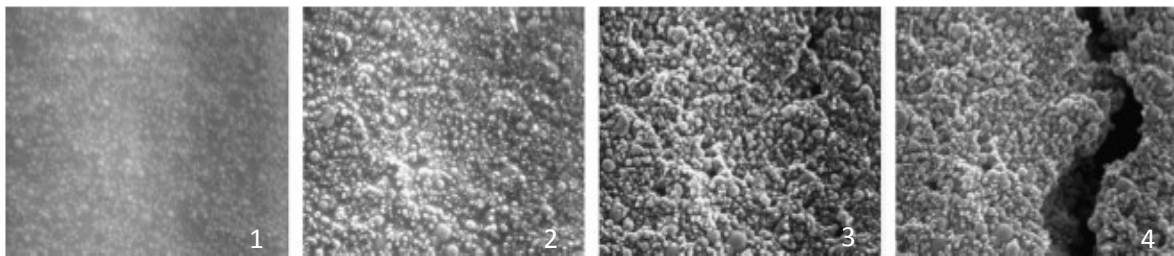


Figure 2.4. Electron microscope images of a freshly mixed fly ash paste upon drying, 300X (Slowik et al., 2008).

The penetration of air into the gaps between the solid particles is essential to the formation of plastic shrinkage cracking. Without the air penetration, plastic shrinkage cracking is impossible (Slowik et al., 2008). However, whether plastic shrinkage cracking occurs or not is also dependent on the level of restrained shrinkage.

2.4 Influencing factors of plastic shrinkage cracking

Plastic shrinkage occurs in a freshly placed concrete element when the water evaporation rate exceeds the bleeding rate of concrete before final set. Plastic shrinkage cracking occurs when air starts to penetrate the gaps between the solid particles, and the tensile stress induced by restraining

plastic shrinkage exceeds the low tensile strength capacity of fresh concrete. Thus, increasing the water evaporation rate of concrete, decreasing the bleeding rate and the tensile strength capacity of fresh concrete could increase the risk of plastic shrinkage cracking in a freshly placed concrete element subjected to a certain restraint.

According to Kosmatka et al. (2002), the water evaporation rate of concrete is determined by its external environmental conditions, while the bleeding rate and the tensile strength capacity of fresh concrete are determined by concrete mixture ingredients and proportions.

2.4.1 Influence of environmental conditions

Plastic shrinkage cracking is often associated with hot weather concreting. The following conditions may increase the risk of plastic shrinkage cracking (Kosmatka et al., 2002):

- High air temperature
- High concrete temperature
- Low relative humidity
- High wind velocity

According to CSA Standard A23.1, when the water evaporation rate of concrete exceeds $1 \text{ kg/m}^2/\text{h}$, plastic shrinkage cracking is likely to occur, and precautions should be applied to the concrete elements. The nomograph shown in Figure 2.5 is commonly used to estimate the water evaporation rate of concrete.

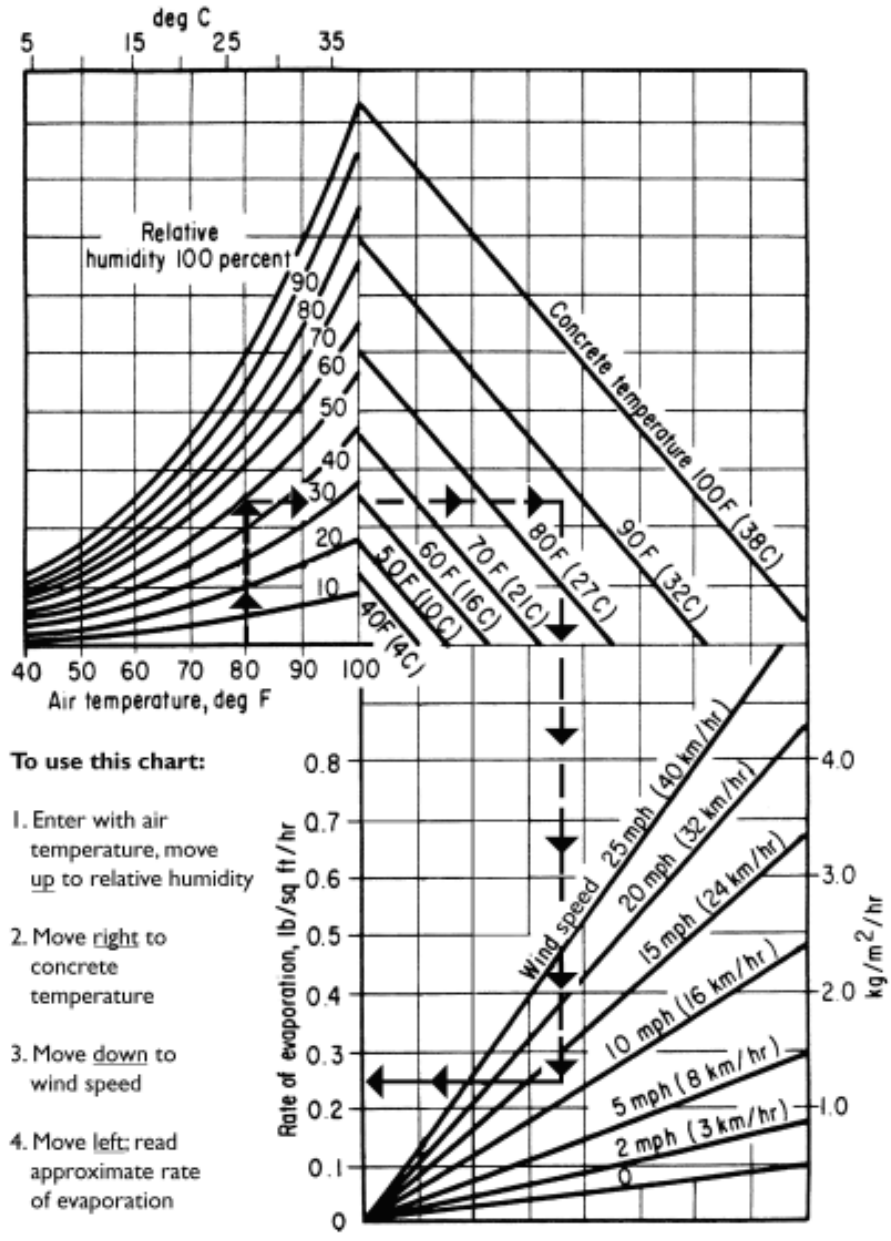


Figure 2.5. Effect of concrete and air temperatures, relative humidity, and wind velocity on the rate of evaporation of surface moisture from concrete (ACI 305R-10, 2010).

The water evaporation rate of concrete can be also estimated by the following equation (Uno, 1998):

$$E = (T_c^{2.5} - rT_a^{2.5})(1 + 0.4V) \times 10^{-6} \quad (\text{Imperial units})$$

$$E = 5([T_c + 18]^{2.5} - r[T_a + 18]^{2.5})(V + 4) \times 10^{-6} \quad (\text{SI units}) \quad \text{Equation 2}$$

Where,

E = evaporation rate, lb/ft²/h (kg/m²/h);

T_c = concrete temperature, °F (°C);

T_a = air temperature, °F (°C);

r = relative humidity, %;

V = wind velocity, mph (km/h).

According to the nomograph and the water evaporation equation, the water evaporation rate of concrete increases when lowering air temperature. However, when relative humidity is relatively low, air temperature has a limited effect on the water evaporation rate of concrete. In practice, concrete temperature is also affected by air temperature, and a high air temperature helps to maintain a high concrete temperature.

2.4.2 Influence of concrete mixture ingredients and proportions

In the following paragraphs, the influence of concrete mixture ingredients and proportions on plastic shrinkage cracking is discussed.

Water to cement ratio (w/c): Almusallam et al. (1998) investigated the effect of different w/c and cement contents on plastic shrinkage cracking in the freshly placed concrete slabs that were exposed to a uniform drying environment. Plastic shrinkage cracking was evaluated by recording the time to first crack and measuring the percentage of total crack area. Figure 2.6 shows the effect

of different w/c and cement contents on the time to first crack. As shown in Figure 2.6, the time to first crack increased with both w/c and cement content (Almusallam et al., 1998). The reason is that increasing w/c and cement content also increased the amount of bleeding water in concrete mixture which delayed the time of air penetration. This effect was also seen by Wang et al. (2001) and Banthia and Gupta (2009).

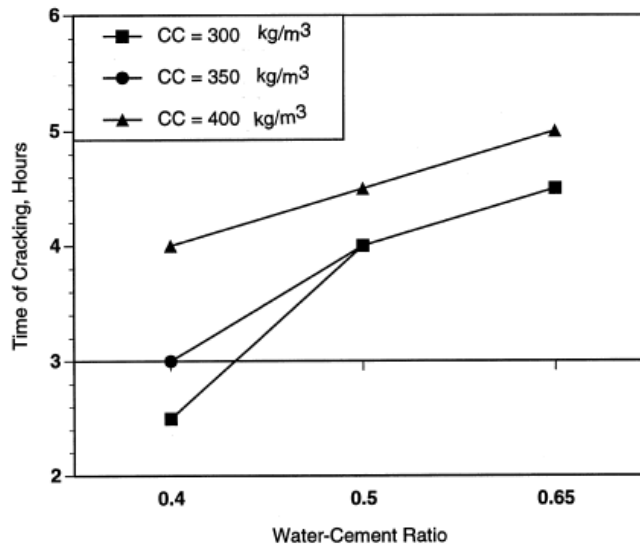


Figure 2.6. Effect of w/c and cement contents on the time to first crack (Almusallam et al., 1998).

Figure 2.7 shows the effect of different w/c and cement contents on the percentage of total crack area. As shown in Figure 2.7, the percentage of total crack area also increased with w/c and cement content (Almusallam et al., 1998). As increasing w/c and cement content increased the amount of bleeding water in concrete mixture, a larger volume change was expected in fresh concrete upon drying, which resulted in a larger crack area. Generally, a concrete mixture with the w/c between 0.50 and 0.60 has the highest contraction due to plastic shrinkage (Wittmann, 1976). However, a slight drop in the percentage of total crack area was observed in the concrete mixture with the w/c

of 0.50 and cement content of 400 kg/m³. This is probably because increasing cement content also increased the tensile strength capacity of fresh concrete to resist cracking.

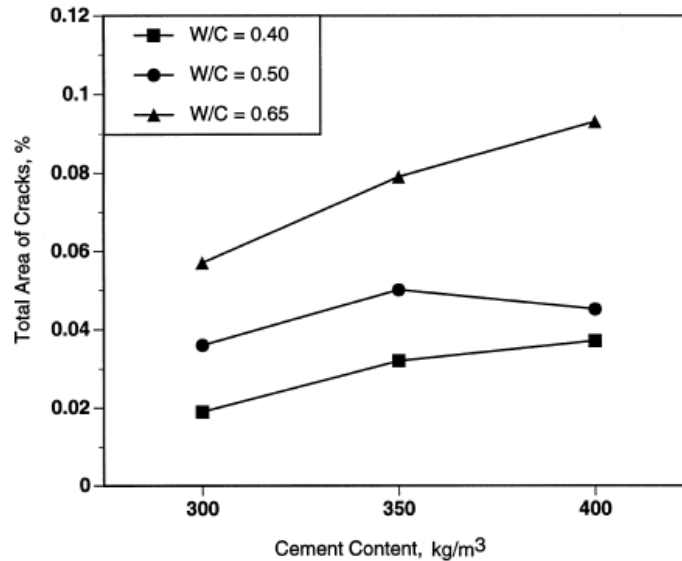


Figure 2.7. Effect of w/c and cement contents on crack area (Almusallam et al., 1998).

Aggregates: Banthia and Gupta (2009) investigated the effect of different coarse aggregate to cement ratios (a/c) on plastic shrinkage cracking in the freshly placed concrete specimens that were exposed to a uniform drying environment. The concrete mixtures had the same w/c and sand to cement ratio. As shown in Figure 2.8, with an increase in a/c, the intensity of plastic shrinkage cracking (maximum crack width and average crack width) decreased. For the concrete mixtures with the same w/c and sand to cement ratio, an increase in coarse aggregate content indicates a drop in water content and cement content which govern early shrinkage in concrete. An increase in coarse aggregate content could also increase the internal friction in concrete mixtures to resist cracking (Banthia and Gupta, 2009), thus reducing the intensity of plastic shrinkage cracking.

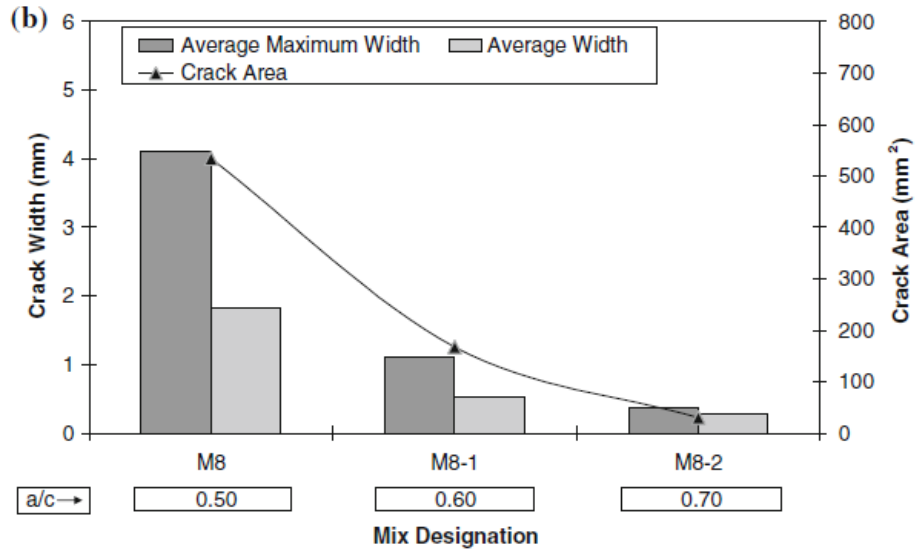


Figure 2.8. Effect of coarse aggregate on plastic shrinkage cracking (Banthia and Gupta, 2009).

Shrinkage-reducing admixture: Shrinkage-reducing admixture is effective in reducing plastic shrinkage cracking in fresh concrete by preventing water loss upon drying and lowering the surface tension of mixing water (Mora-Ruacho et al., 2009; Saliba et al., 2011). According to the Young-Laplace equation (Equation 1), capillary pressure p_c decreases with surface tension of the capillary water γ .

Supplementary cementitious materials: Supplementary cementitious materials reduce the bleeding rate and develop relatively low early strength, which could increase the risk of plastic shrinkage cracking. Concrete containing silica fume is particularly sensitive to plastic shrinkage cracking due to its relatively low bleeding rate. CSA Standard A23.1 requires that when the water evaporation rate of concrete exceeds $0.25 \text{ kg/m}^2/\text{h}$, precautions should be applied to the concrete elements containing silica fume (Kosmatka et al., 2002).

Fibers: The most widely accepted method to control plastic shrinkage cracking is to add short and randomly distributed fibers in concrete mixtures. By adding fibers in concrete, the settlement of fresh concrete is reduced, while the bleeding rate and the tensile strength capacity of fresh concrete are increased (Qi et al., 2005; Rahmani et al., 2012).

2.5 Restrained plastic shrinkage testing techniques

As discussed earlier, whether cracking occurs or not is also dependent on the level of shrinkage restraint. In literature, plastic shrinkage cracking has been evaluated in fresh concrete specimens under a variety of restrained conditions which were designed to induce cracking. Four main specimen geometries have been used to evaluate plastic shrinkage cracking, including ring (Bjøntegaard et al., 1998), longitudinal (Banthia et al., 1995; Mora et al., 2000; Mora-Ruacho et al., 2009), slab (Balaguru, 1994; Kraai, 1985; Shaeles and Hover, 1988; Yokoyama et al., 1994), and substrate restraint (Banthia and Gupta, 2007; Banthia and Gupta, 2006; Berke and Dallaire, 1994; Naaman et al., 2005; Qi et al., 2003; Saliba et al., 2011; Soroushian and Ravanbakhsh, 1998; Turcry and Loukili, 2006).

2.5.1 Ring test

Bjøntegaard and Sellevold (1998) adopted a ring type test to evaluate plastic shrinkage cracking in high performance concrete. Concrete was cast between two concentric steel rings with a depth of 50 mm fixed on a rigid plate. The diameters of two concentric rings were 280 mm and 580 mm, respectively. In order to restrain the shrinkage in fresh concrete between two concentric rings, 12 rigid ribs were attached to the inside of outer ring, and 3 rigid ribs were attached to the outside of inner ring. A controlled air funnel was placed 10 mm above the concrete specimen to provide a

continuous drying environment, as shown in Figure 2.9. In this geometry, plastic shrinkage cracking occurred at the locations near the ribs attached to the rings (Bjøntegaard et al., 1998).

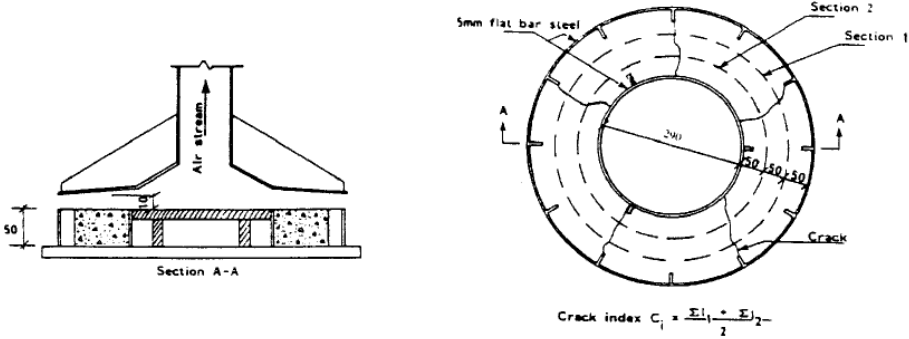


Figure 2.9. Diagram of ring geometry with ribs under air funnel (Bjøntegaard et al., 1998).

2.5.2 Longitudinal tests

Banthia et al. (1995) proposed a longitudinal type test to evaluate plastic shrinkage cracking in fiber reinforced concrete. The size of the specimen was 40×40×500 mm. Two triple-bar anchors installed at the two ends of the specimen mold were designed to restrain the shrinkage, as shown in Figure 2.10. The whole assembly was then exposed to a drying environment to induce cracking (Banthia et al., 1995).

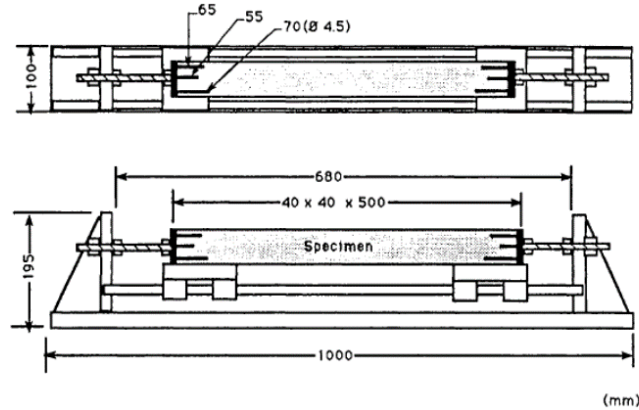


Figure 2.10. Diagram of longitudinal geometry with triple-bar anchors (Banthia et al., 1995).

Mora et al. (2000) proposed a different type of longitudinal test to evaluate the effect of different fibers on plastic shrinkage cracking. Concrete was cast in a specimen mold with a size of 150×150×600 mm. The shrinkage was restrained by several anchor bolts installed at the two ends of the specimen mold. A riser placed in the center of the mold reduced the depth of the concrete specimen and concentrated the tensile stress generated by restraining the shrinkage, as shown in Figure 2.11. The whole assembly was then placed in a wind tunnel. In this geometry, plastic shrinkage cracking occurred at the location above the center riser (Mora et al., 2000; Mora et al., 2009).

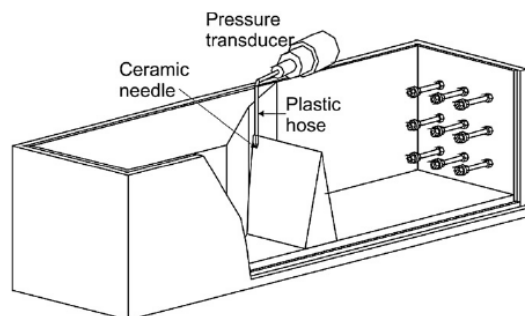


Figure 2.11. Diagram of longitudinal geometry with anchor bolts and a center riser (Mora et al., 2009).

2.5.3 Slab tests

As plastic shrinkage cracking is often observed in concrete structures with a large exposed surface area, such as concrete slabs and pavements, researchers have developed slab type tests in order to simulate plastic shrinkage cracking occurred in such condition.

Kraai (1985) proposed a slab test in which two identical thin concrete slabs with different concrete mixtures were exposed to a drying environment created by two electrical fans, as shown in Figure 2.12. The thin concrete slabs had a large surface area which was 24 inches (610 mm) wide and 36 inches (914 mm) long, while the thickness of the concrete slabs was only $\frac{3}{4}$ inch (19 mm). Due to the thin depth, concrete mixtures cannot contain any coarse aggregate in this geometry. An L-shape hardware cloth was installed around the perimeter of each specimen mold to restrain shrinkage (Balaguru, 1994; Kraai, 1985; Shaeles and Hover, 1988).

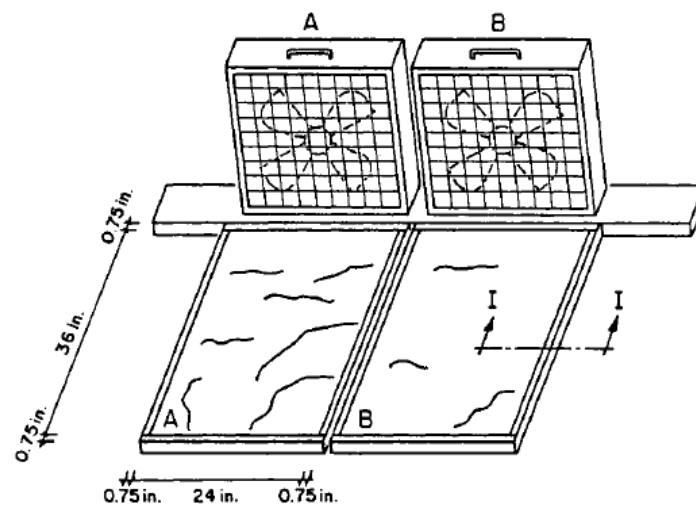


Figure 2.12. Diagram of thin slab test with electrical fans (Shaeles and Hover, 1988).

Yokoyama et al. (1994) proposed a similar slab test which was used to evaluate plastic shrinkage cracking in high performance concrete and self-consolidation concrete. The concrete slab with a large surface area of 600×600 mm and a thickness of 50 mm was exposed to a drying environment. The shrinkage was restrained by the stud bolts installed at the four ends of the specimen mold (Yokoyama et al., 1994), as shown in Figure 2.13.

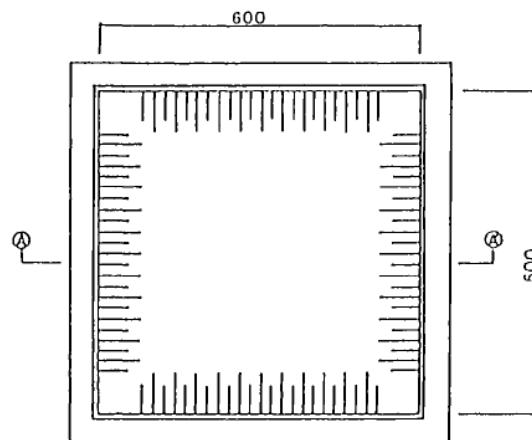


Figure 2.13. Diagram of slab test using stud bolts at four ends (Yokoyama et al., 1994).

2.5.4 Substrate restraint tests

In practice, plastic shrinkage cracking is often observed in overlays in the case of concrete repair. In order to simulate plastic shrinkage cracking occurred in such condition, Wang et al. (2001) used cement paste that was cast in a Plexiglas mold to investigate the effect of fly ash and fibers on plastic shrinkage cracking. The size of the mold was 100×100×8 mm. A fine sandpaper attached to the bottom of the mold was designed to provide restraint. The specimens were then placed in a drying environment to induce cracking.

Banthia et al. (1996) proposed a substrate restraint type test to evaluate plastic shrinkage cracking in fiber reinforced concrete. In the experiment, a 100 mm deep layer of fiber reinforced concrete was cast on a 40 mm deep, 1010 mm long and 100 mm wide high strength concrete substrate which was prepared earlier. The substrate had a rough surface provided by the half exposed coarse aggregate. The shrinkage was restrained by the rough surface of the substrate. The whole assembly was then exposed to a drying environment to induce cracking (Banthia et al., 1996), as shown in Figure 2.14. The drawback of this test is that the restraint provided by half exposed aggregate may vary from substrate to substrate.

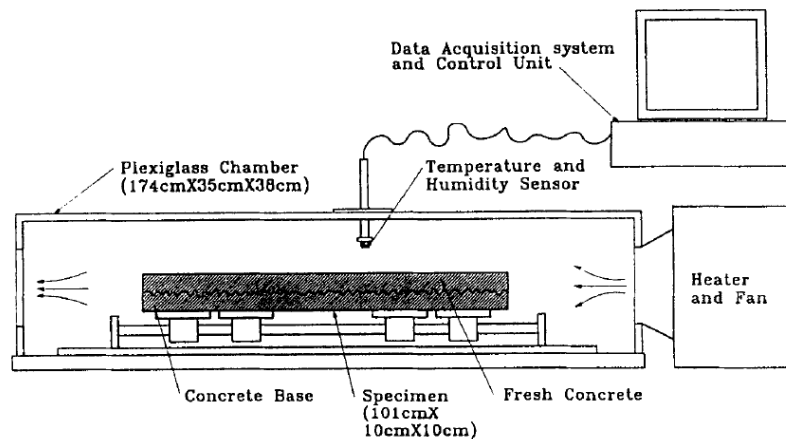


Figure 2.14. Diagram of substrate restraint type test using half exposed aggregate (Banthia et al., 1996).

Banthia and Gupta (2006) then made some modifications to the substrate restraint test. In this experiment, a 60 mm deep layer of concrete was cast on a 40 mm deep, 95 mm wide, and 325 mm long substrate, as shown in Figure 2.15. The rough surface was provided by several uniform semicircular protrusions with a diameter of 18.5 mm instead of half exposed aggregate, so the amount of restraint can be quantified (Banthia and Gupta, 2006; Banthia and Gupta, 2007).

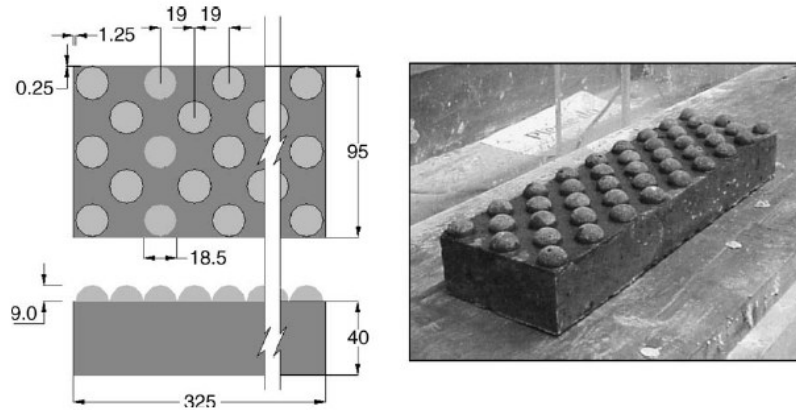


Figure 2.15. Diagram of substrate with uniform semicircle protrusions (Banthia and Gupta, 2006).

As plastic shrinkage cracking is often observed at locations in concrete structures with different depths, Naaman et al. (2005) proposed a different type of substrate restraint test which was used to evaluate the effect of different fibers on plastic shrinkage cracking in fresh concrete. The substrate in this test had a grooved structure, which was prepared with high strength and low shrinkage concrete, as shown in Figure 2.16. Concrete cast on the grooved substrate had alternating depths of 38.1 mm and 50.8 mm. With a surface area of 76.2×1016 mm, the whole assembly was exposed to a drying environment which was designed to induce cracking (Naaman et al., 2005). In this geometry, plastic shrinkage cracking is caused by a combined effect of surface drying and plastic settlement.

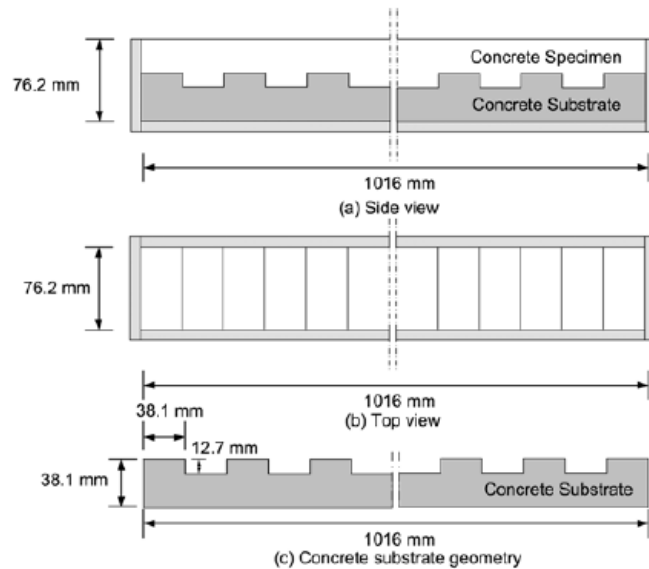


Figure 2.16. Diagram of plastic shrinkage cracking test setup using a substrate with a grooved structure (Naaman et al., 2005).

Berke and Dallaire (1994) proposed a riser type of substrate restraint test to simulate the condition that plastic shrinkage cracking occurred above the embedded reinforcing steel in concrete structures. In this test, plastic shrinkage was restrained by two minor stress risers placed inward from the two ends of the mold, while a center riser reduced the depth of concrete slab and concentrated the tensile stress. Plastic shrinkage cracking in this geometry occurred at the location above the center riser (Berke and Dallaire, 1994; Qi et al., 2003; Soroushian and Ravanbakhsh, 1998). In the riser type of substrate restraint test, the restraint provided by the risers, which simulates the embedded reinforcing steel, is more realistic than the other types of tests (Soroushian and Ravanbakhsh, 1998). As the cracking occurs at a predetermined location, it is also easier to evaluate the cracking. In addition, the mold with risers can be demolded easily and reused.

In 2006, ASTM Standard C1579 was introduced based on the riser type of substrate restraint test, which was intended to compare plastic shrinkage cracking behavior in concrete mixtures with

different types of fibers (Rahmani et al., 2012) or admixtures (Leemann et al., 2014; Rahmani et al., 2012). In the ASTM Standard C1579, the mold dimensions for a concrete mixture with maximum coarse aggregate size less than 19 mm are 100 ± 5 mm deep, 355 ± 10 mm wide, and 560 ± 10 mm long. Two 32 ± 1 mm high minor stress risers and a 64 ± 2 mm high center stress riser are bent from a piece of sheet metal, as shown in Figure 2.17.

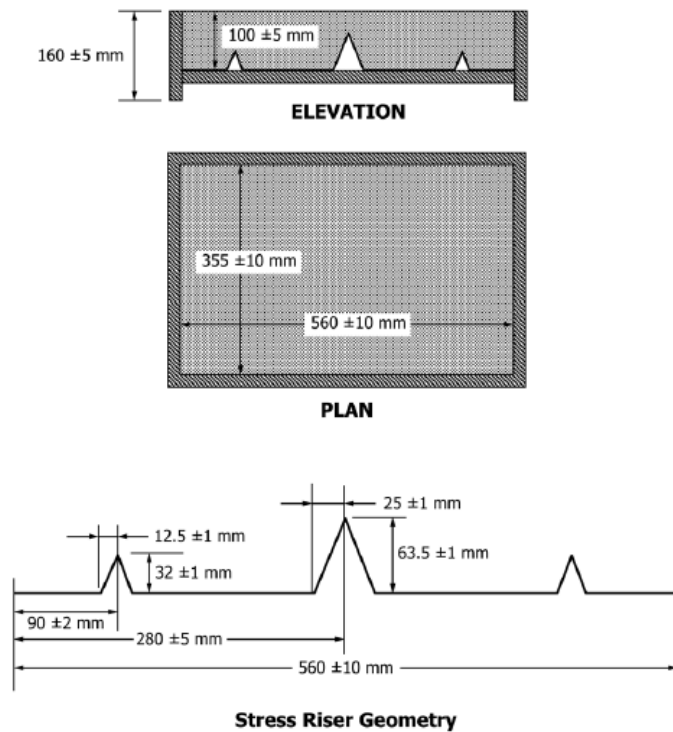


Figure 2.17. Diagram of specimen mold and stress risers (ASTM Standard C1579-13, 2013).

In order to increase the likelihood of plastic shrinkage cracking in this geometry, an environmental chamber is designed to be able to provide a constant temperature of $36 \pm 3^\circ\text{C}$, a relative humidity of $30 \pm 10\%$, and a minimum wind velocity of 4.7 m/s, as shown in Figure 2.18. During the experiment, a minimum water evaporation rate of $1.0 \text{ kg/m}^2/\text{h}$ must be reached, which is measured from water loss in a pan placed next to the concrete specimen in the environmental chamber.

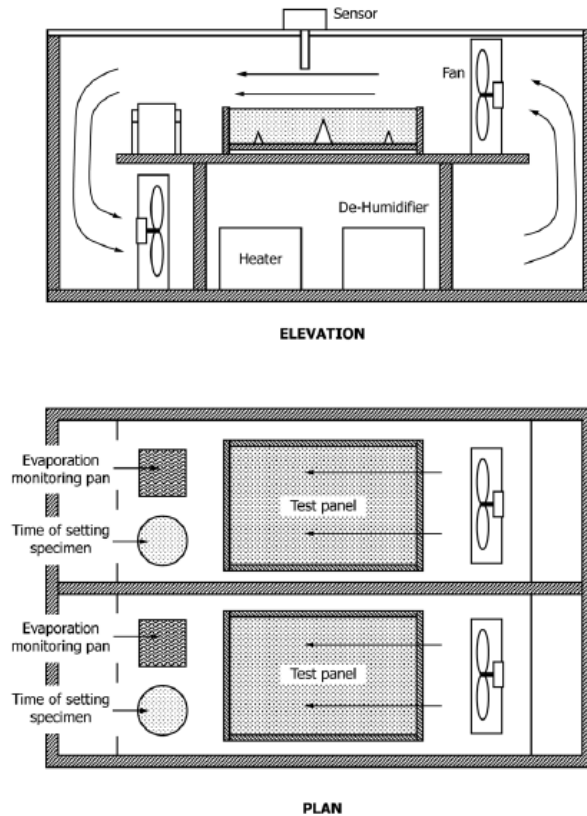


Figure 2.18. Diagram of environmental chamber (ASTM Standard C1579-13, 2013).

In the standard test, the setting time of the concrete mixtures placed in the environmental chamber is determined according to ASTM Standard C403/C403M. At the time of final set, the environmental chamber is turned off. At 24 hours after the concrete specimens are placed in the environmental chamber, the cracking is considered stable. The crack widths are then measured at 10 ± 1 mm intervals along the crack path. The effect of fibers on plastic shrinkage cracking is evaluated by a cracking reduction ratio (CRR) which is calculated by the following equation (ASTM Standard C1579-13, 2013):

$$CRR = \left[1 - \frac{\text{Average Crack Width of Fiber Reinforced Concrete Mixture}}{\text{Average Crack Width of Control Concrete Mixture}} \right] \times 100\% \quad \text{Equation 3}$$

2.6 Image analysis techniques

In the discussed four main specimen geometries, plastic shrinkage cracking is evaluated either by measuring the crack dimensions in hardened concrete specimens, such as the maximum crack width, average crack width, total crack length, and total crack area (average crack width multiplied by total crack length), or recording the cracking process, such as the number of cracks at different points in time throughout the cracking process and the time to first crack (Bentur and Kovler, 2003). Researchers have used several tools to take such measurements. In ASTM Standard C1579, it is suggested that optical hand-held microscope, crack comparator, or image analysis system can be used. Among these crack measurement tools, image analysis system has been found to be an effective tool for the systematic characterization of cracking in concrete materials (Qi et al., 2003) due to its reliable results and high precision (Barazzetti and Scaioni, 2009). In the following sections, several available image analysis techniques for cracking assessment in fresh concrete as well as hardened concrete are reviewed.

2.6.1 Scanning electron microscope (SEM)

Mindess and Diamond (1980) developed a special device that allowed for hardened concrete under loading to be observed within the sample chamber of an SEM. Due to the high resolution of the SEM, the development of cracking was clearly observed in hardened concrete under loading, and the cracking process was well understood (Mindess and Diamond, 1980). However, the drawbacks of using an SEM to observe the cracking process are the limitation of sample size and additional cracks induced under vacuum at the preparation stage (Mauroux et al., 2012).

2.6.2 Crack border detection

With the developments of digital image analysis techniques, researchers have used a “crack border detection” function (Barazzetti and Scaioni, 2009) to extract crack contours from a digital image taken above the crack on the surface of a concrete element. When a crack occurs on the surface of a concrete element, it changes the surface texture of the concrete element. Consequently, when a digital image is taken above the crack, the image texture is also changed by the presence of the crack. The principal idea of crack border detection is to recognize crack contours by detecting the changes in the surface texture of a concrete element in a digital image.

To be specific, three primary colors, namely red, green, and blue (RGB), are combined together to display a variety of colors in the digital system. Figure 2.19 shows the intensity of each RGB component along a typical crack cross-section. As shown in Figure 2.19, the intensity of each RGB component experiences a significant decrease in the presence of the crack, and relatively small fluctuations outside the crack. For each RGB component, the minimum intensity is located in the center of the crack. The deviations in the intensity of each RGB component correspond exactly to the crack borders; therefore, the crack borders can be extracted by recognizing the deviations in the intensity of each RGB component (Barazzetti and Scaioni, 2009).

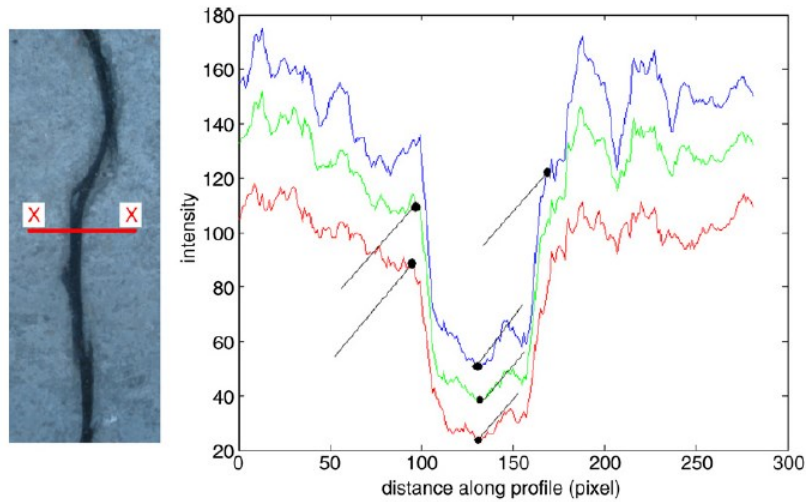


Figure 2.19. Intensity of each RGB component along a typical crack cross-section (Barazzetti and Scaioni, 2009).

In practice, this process can be achieved by the following steps. First, the RGB image is converted to a grayscale image which only carries intensity information. Then, a thresholding function is applied to the grayscale image to filter the intensity inside the crack. The pixels with the intensity values less than the threshold value are replaced by the black pixel, while the pixels with the intensity values higher than the threshold value are replaced by the white pixel. By doing so, crack contours are extracted, and the grayscale image is converted to a binary image which only carries two colors, black and white (Barazzetti and Scaioni, 2009; Qi et al., 2003).

Based on the function of crack border detection, Qi et al. (2003) proposed a semi-automatic image analysis technique to evaluate plastic shrinkage cracking in fiber reinforced concrete. Figure 2.20 provides an overview of the image analysis procedure that was used.

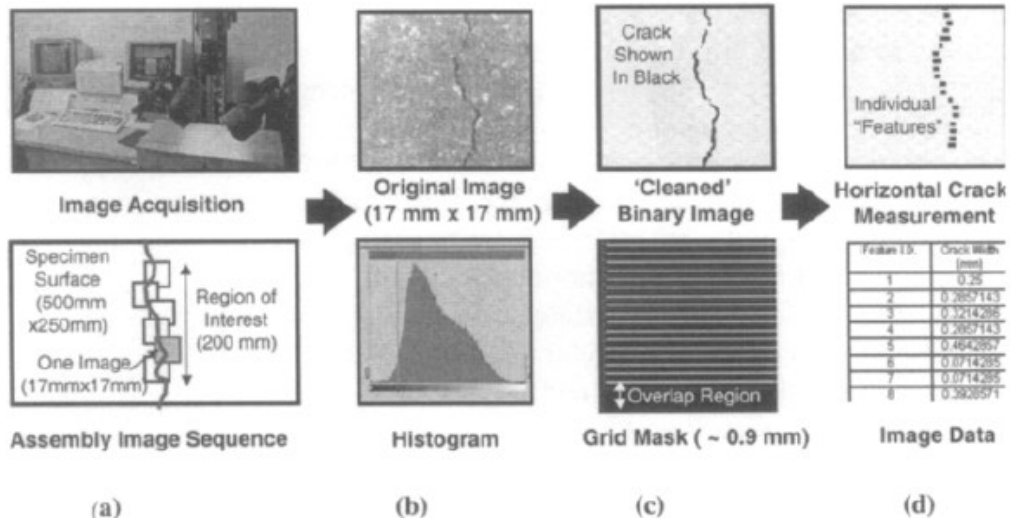


Figure 2.20. Image analysis procedure: (a) image acquisition, (b) image processing, (c) crack feature determination, and (d) crack measurement (Qi et al., 2003).

First, images were taken above a crack on the surface of a concrete specimen by a charge-coupled device camera (digital camera), as shown in Figure 2.20 (a). The digital camera used in the experiment provided a resolution of 480×480 pixels in a 17×17 mm image (0.0354 mm/pixel), so the crack widths less than 0.0354 mm cannot be detected.

Then, the images were converted to the grayscale images. Figure 2.21 (a) shows a typical grayscale image. An intensity distribution histogram for each grayscale image was generated, as shown in Figure 2.21 (b). The threshold value used in this experiment that extracted the crack contours from the concrete background was 80% of the intensity value at the peak frequency.

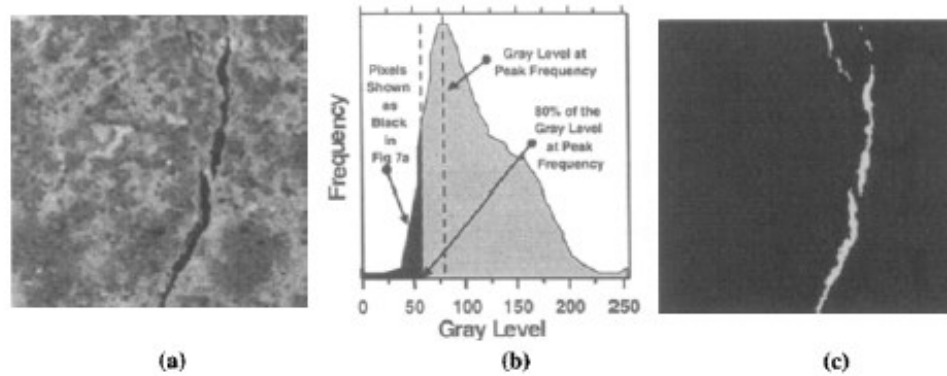


Figure 2.21. Image processing procedure: (a) grayscale image, (b) intensity distribution histogram, and (c) binary image after cleaning (Qi et al., 2003).

Generally, a finished concrete surface may have some air pockets or defects that have similar grayscale intensities to the crack. These points were also extracted by applying the thresholding function. To minimize such problems, these points were removed in an image-editing program, such as Photoshop. Thus, only the crack contours were preserved. Figure 2.21 (a) and (c) provide a comparison between the grayscale image and the binary image with the crack contours after the thresholding and cleaning process. It can be seen that two images corresponded well.

After the crack contours were extracted, a grid with uniform intervals was applied to the binary image. The crack widths were measured as the lengths of the grid intercepted by the crack contours (Qi et al., 2003), as shown in Figure 2.20 (c) and (d).

Qi et al. (2005) compared the crack widths that were measured by the semi-automatic image analysis technique and an optical microscope, and found that the crack widths measured by the optical microscope were slightly larger than those measured by the semi-automatic image analysis, as shown in Figure 2.22. The reason was that the optical measurements were taken on the top surface, while the semi-automatic image analysis technique was based on the crack contours that

were extracted lower than top surface of the concrete specimen (Qi et al., 2005). However, this image analysis technique was an effective tool to measure the crack widths rapidly at numerous locations without human error.

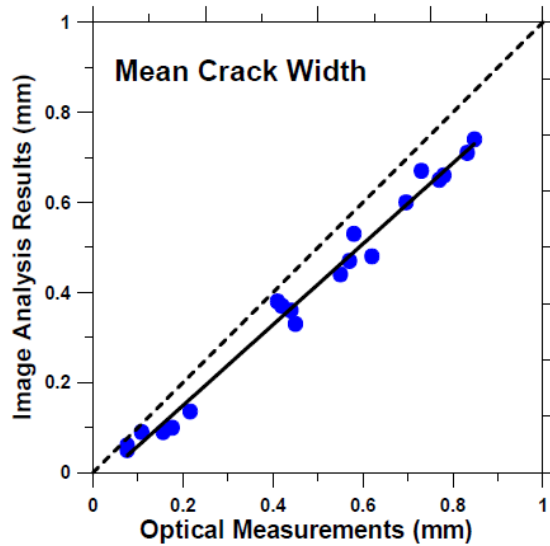


Figure 2.22 Crack widths measured by image analysis and optical microscope (Qi et al., 2005).

Banthia and Gupta (2009) proposed a similar image analysis technique based on the function of crack border detection to evaluate the development of plastic shrinkage cracking in fresh concrete by measuring the crack area at different time points throughout the experiment. A series of high resolution images was taken above the top surface of a freshly placed concrete specimen that was exposed to a drying environment at constant time intervals by a fixed digital camera. The crack was first extracted by the thresholding function. Technically, when a binary image is created, the pixels of a single color can be counted. The black pixels which represented the crack were then counted, as shown in Figure 2.23. The pixels in a known area on the top surface of the concrete specimen were also counted in order to establish a calibration factor. By applying the calibration factor to the black pixels inside the crack, the crack area was determined (Banthia and Gupta,

2009). The development of plastic shrinkage cracking was then evaluated by the crack areas at different time points.

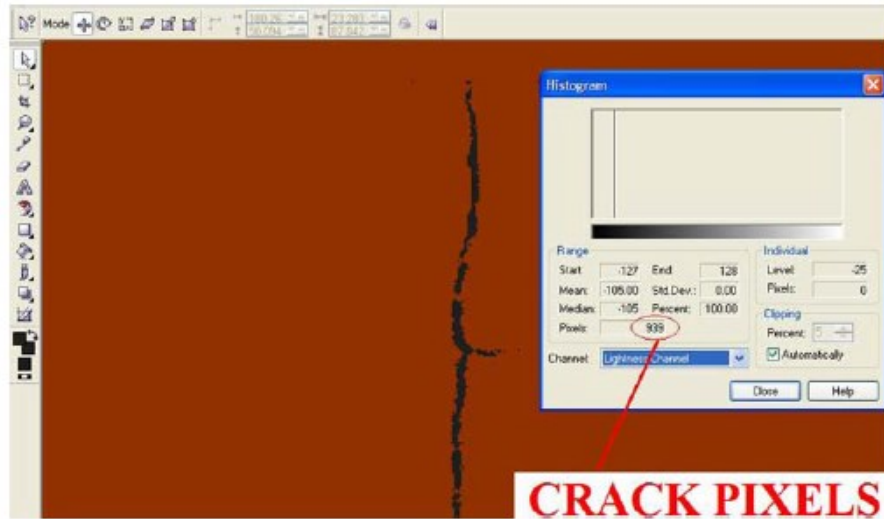


Figure 2.23. Crack area determined by counting the pixels inside the crack (Banthia and Gupta, 2009).

2.6.3 Particle tracking

Ong and Myint-Lay (2006) proposed a test method to evaluate plastic shrinkage of concrete by analyzing the movement of targets which were installed in a freshly placed concrete specimen. The targets used in this experiment were made of 100 mm long steel pins with 0.5 mm in diameter. An inked target was glued on the top of the pin, as shown in Figure 2.24.

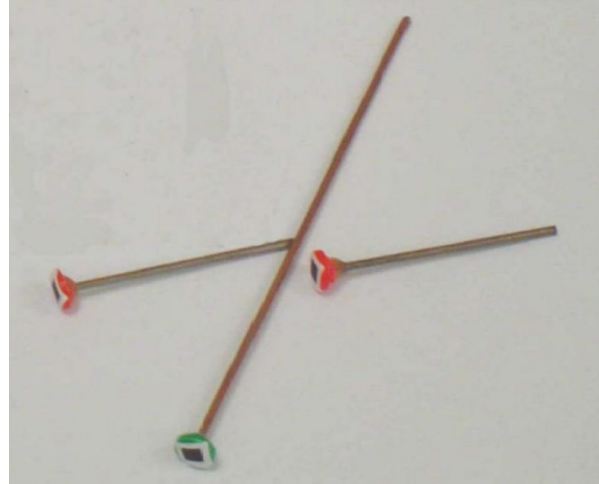


Figure 2.24. Steel pin targets for image analysis (Ong and Myint-Lay, 2006).

In the experiment, concrete was cast in a mold with a size of 100×100×500 mm. Three pairs of targets spaced approximately 400 mm apart were inserted into the freshly placed concrete specimen. The pairs of targets were penetrated full depth of the freshly placed concrete specimen to ensure that the targets can move along with fresh concrete, as shown in Figure 2.25. The movement of each pair of targets was monitored by capturing a series of images by a fixed digital camera with a resolution of 6.3 megapixels (3072×2048 pixels).

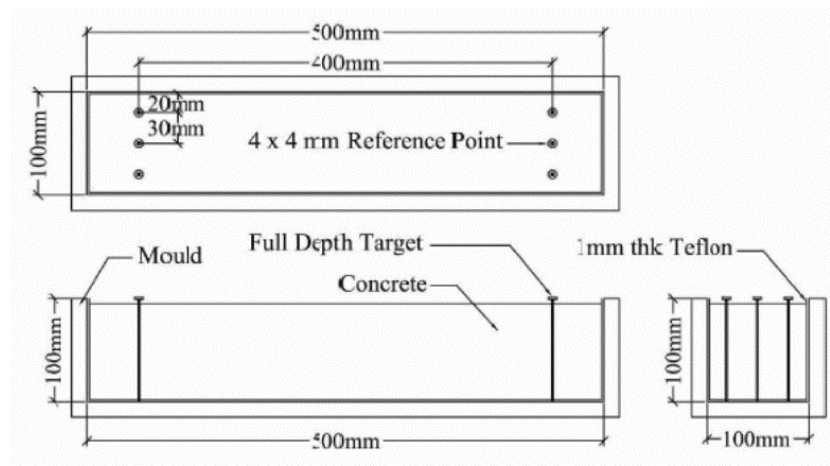


Figure 2.25. Diagram of specimen mold and locations of targets (Ong and Myint-Lay, 2006).

The targets were first extracted from the concrete background by applying the thresholding function to these images. The pixel coordinates of targets in each image were then identified. The shrinkage strain can be calculated by dividing the change in pixels between each pair of targets by the original distance in pixels (Ong and Myint-Lay, 2006). However, the shrinkage at the top and the bottom of the freshly placed concrete specimen may not be identical due to the different water evaporation rates. Thus, additional friction may be induced in the freshly placed concrete specimen due to the full depth penetration of the pins.

Barazzetti and Scaioni (2009) proposed a similar image analysis technique to evaluate the development of an existing crack in hardened concrete based on particle tracking. The experiment setup used in this method was made of a digital camera, an orientation frame, and a pair of targets (Barazzetti and Scaioni, 2009), as shown in Figure 2.26.

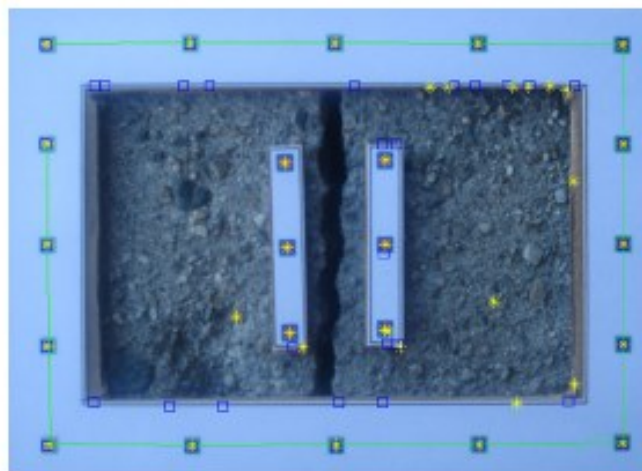


Figure 2.26. Orientation frame and a pair of targets placed on both sides of a crack (Barazzetti and Scaioni, 2009).

In order to establish an object reference system, the orientation frame with several targets in set distances was laid around the crack, and a pair of targets were laid on the both sides of the crack.

By the thresholding function, the targets in the orientation frame and the targets laid on the both sides of the crack were extracted from the concrete background. The pixel coordinates of the targets were then obtained. As the targets in the orientation frame and the pair of targets laid on the both sides of the crack were known in the image and object space, it allowed to transform the coordinates of other points from the image space to the object space. By evaluating a series of images at different time points, the crack deformation can be obtained (Barazzetti and Scaioni, 2009), as shown in Figure 2.27.

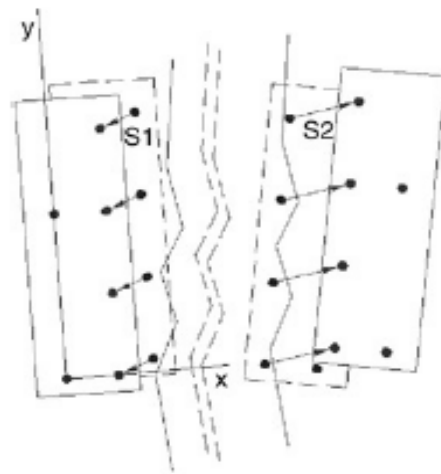


Figure 2.27. Displacement between targets (Barazzetti and Scaioni, 2009).

This image analysis technique can be used to monitor the development of an existing crack on the surface of a hardened concrete element. The advantage is that the camera does not have to be fixed. However, the cracking pattern of concrete is complicated, the orientation frame and the pair of targets attached to the concrete specimen may disturb the cracking process. Moreover, it cannot be used to analyze a crack deformation before the presence of the crack, because it is challenging to decide where to lay the orientation frame and the pair of targets.

2.6.4 Digital image correlation (DIC)

Recently, a non-contact and full-field shape and deformation measurement technique based on DIC has been widely used to examine the deformation in metallic or ceramic materials (Mauroux et al., 2012). It is commercially available in 2D and 3D version (VIC-2D and VIC-3D from Correlated Solutions for example). The principal idea of DIC is to compare two images taken before and after a deformation, which are called the “reference image” and the “deformed image”, respectively. The deformation measurements are based on the correlation made between any two reference image and deformed image.

To be specific, the reference image and the deformed image are first divided into a finite number of subimages. If the images show a unique texture pattern, the subimages in the reference image can be recognized in the deformed image by using a pattern-matching algorithm; therefore, the displacements of the subimages can be obtained, and many strain tensors can be computed (Mauroux et al., 2012), as shown in Figure 2.28.

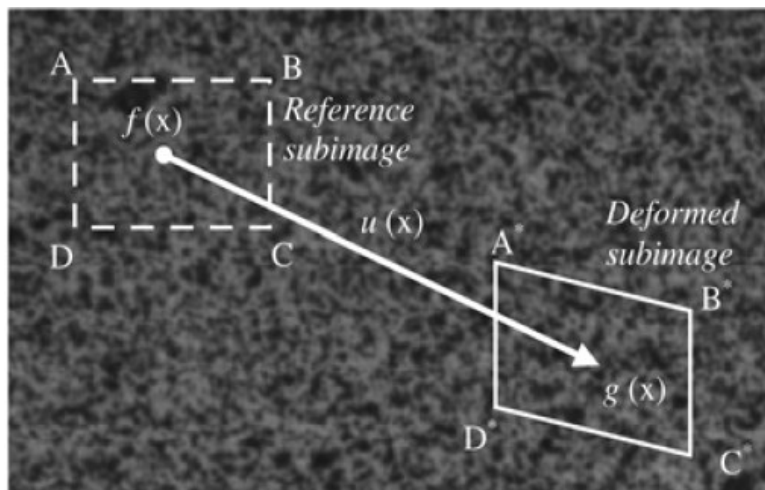


Figure 2.28. Schematic diagram of the reference and the deformed subimages in an image (Alam et al., 2012).

Choi and Shah (1997) first applied 2D-DIC in concrete materials for the study of compressive failure behavior of concrete. The deformation of the concrete slab with a size of 125×125×25 mm under loading was obtained from both DIC and the linear variable differential transducer (LVDT). The results showed a high correlation between both methods, as shown in Figure 2.29. In addition, the deformation measured by DIC can be described as a strain contour map, which provided more detailed information.

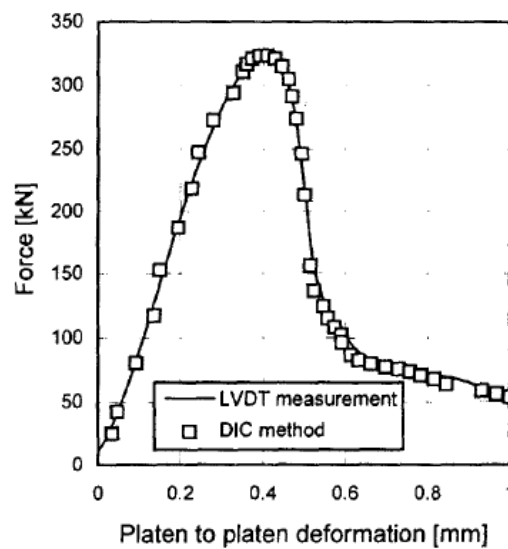


Figure 2.29. Deformation obtained from DIC and LVDT (Choi and Shah, 1997).

However, the precision of deformation measurements by DIC is significantly dependent on the quality of image texture (Mauroux et al., 2012). Technically, it is difficult to find the subimages in the reference image in the deformed image for a textureless structure. As shown in Figure 2.30 (a), in a textureless image, a point on the line can be matched to several points in the displaced line. This problem can be solved by placing several apertures over the image. By placing the apertures to the line, the ends of the line are revealed. Thus, the motion vectors can be uniquely

determined, as shown in Figure 2.30 (b). In practice, to solve the correspondence problem, a speckle pattern is usually applied to the textureless structure (Sutton et al., 2009). However, currently, there are no widely accepted guidelines for how to select the speckle pattern and how to apply the speckle pattern to a specimen surface.

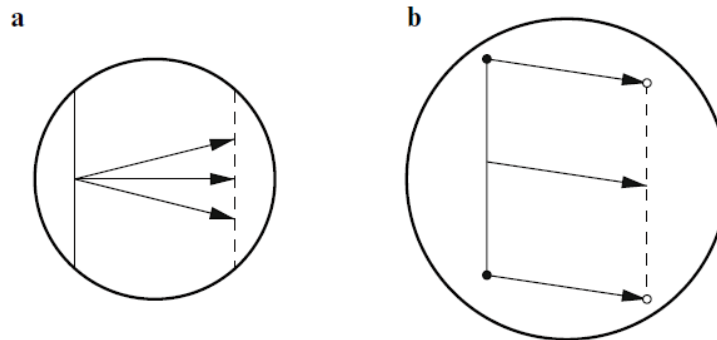


Figure 2.30. Apertures in image matching: (a) matching problem, (b) unique matching by placing apertures (Sutton et al., 2009).

Generally, concrete surface is considered as a textureless structure. To apply the speckle pattern to the surface of a concrete specimen, a black or white spray paint is usually applied onto the surface of the concrete specimen (Alam et al., 2012; Boulekbache et al., 2015; Choi and Shah, 1997; Corr et al., 2007; Mauroux et al., 2012). Alam et al. (2012) mentioned that an effective speckle pattern should contain small black speckles with the sizes around 10 pixels, medium black speckles around 20 pixels, and large black speckles around 30 pixels, while Sutton et al. (2009) suggested that for accurate matching, the sizes of speckles should be larger than 3×3 pixels.

Generally, when concrete is under loading, a small amount of out-of-plane motion may occur in the concrete surface. When using 2D-DIC, the out-of-plane motion therefore induces image plane

displacement gradients, which may cause false correlations. This problem can be solved by using 3D-DIC system or a telecentric lens in 2D-DIC system (Sutton et al., 2009).

Gencturk et al. (2014) used 3D-DIC technique to evaluate a prestressed concrete structure under loading and summarized the advantages and limitation of DIC technique. DIC technique is a non-contact method, and can provide accurate and detailed information in full-field strain measurements, while the limitation is that the crack dimensions cannot be measured by DIC.

2.7 Summary

In the literature, the evaluation of plastic shrinkage cracking was generally based on characterization of the cracks in term of maximum width, average width, total length, or total area in hardened concrete. Due to the limitation of the traditional crack measurement tools, only a few research projects were conducted to evaluate the process of plastic shrinkage cracking. By using image analysis technique of crack border detection, Banthia and Gupta (2009) evaluated the development of plastic shrinkage cracking in fresh concrete by measuring the crack area at different time points throughout the experiment. In recent years, DIC has been successfully applied to analyze the cracking propagation in hardened concrete under loading because the deformation measured by DIC can be described as a series of strain contour maps, which provided more detailed information. So far, no work has been conducted on analyzing the development of strains using DIC method on the surface of concrete or cement paste during the process of plastic shrinkage cracking.

3 EXPERIMENTAL PROGRAM

3.1 Introduction

As ASTM standard C1579 is the only existing ASTM standard in regards to plastic shrinkage cracking, experiments were first conducted conforming to ASTM standard C1579. Several concrete specimens that were cast in the standard form were tested separately in a drying environment; however, no cracking occurred. Although not successful, the chapter begins with experiments performed on concrete. Later, cement paste specimens that were cast in a much smaller form adopted from Wang et al. (2001) were tested in this project. A series of images was taken above the specimen surface throughout each experiment. DIC analysis was then performed on these images. As DIC cannot measure the crack dimensions, the images were also processed using MATLAB to determine the crack areas.

As discussed in the literature review, plastic shrinkage cracking is influenced by concrete mixture ingredients and proportions as well as its external drying environment and restraint conditions. In the experimental program, cement paste specimens with the same w/c that were exposed to different air temperatures, wind velocities were tested and investigated first. Then, cement paste specimens with different w/c that were exposed to a uniform drying environment were studied. Finally, research was conducted on cement paste specimens with the same w/c that were cast on different restraint conditions and tested in a uniform drying environment.

In this chapter, the information on the materials, environmental conditions, and camera specifications is provided. Specimen geometries, mixture proportions, and testing procedures are described for each purpose separately. A MATLAB script developed to determine the crack area and the image correlation software VIC-2D are presented as well.

3.2 Materials

The cement used in this work was commercially available Type GU Portland cement. The mixing water was from two separate hot and cold taps in the laboratory, and its temperature was controlled at 30 °C. Locally available crushed limestone with the nominal maximum size of 14 mm and natural sand with the fineness modulus of 2.48 were used as coarse and fine aggregates, respectively. Sieve analysis of the coarse and fine aggregates was conducted according to ASTM Standard C136/C136M-14, and both the coarse and fine aggregates met the grading requirements specified in ASTM Standard C33/C33M-13. The coarse aggregate had an oven-dry rodded bulk density of 1470 kg/m³, an oven-dry specific gravity of 2.51, and an absorption of 0.8%. The bulk density, specific gravity, and absorption of the coarse aggregate were tested according to ASTM Standard C29/C29M-09 and ASTM Standard C127-15. The fine aggregate had an oven-dry specific gravity of 2.44 and an absorption of 1.0%. The specific gravity and absorption of the fine aggregate were tested according to ASTM Standard C128-15. The cement, coarse aggregate and fine aggregate were stored in the laboratory environment more than 24 hours before use. Corrections were made to compensate for moisture in and on the aggregates before mixing concrete.

3.3 Environmental conditions

An environmental chamber was fabricated to provide a hot, dry, and windy environment, as shown in Figure 3.1. Two electrical fan heaters placed in the environmental chamber were used to control air temperature. An electrical fan with three speed settings placed in the environmental chamber was used to achieve a minimum wind velocity of 4.7 m/s specified in ASTM Standard C1579-13. Air temperature, relative humidity, and wind velocity were measured at an elevation about 10 cm above the specimen surface by a Kestrel 4300 construction weather tracker. Concrete temperature

was measured by a dial pocket thermometer, while cement paste temperature was monitored by an infrared thermometer.

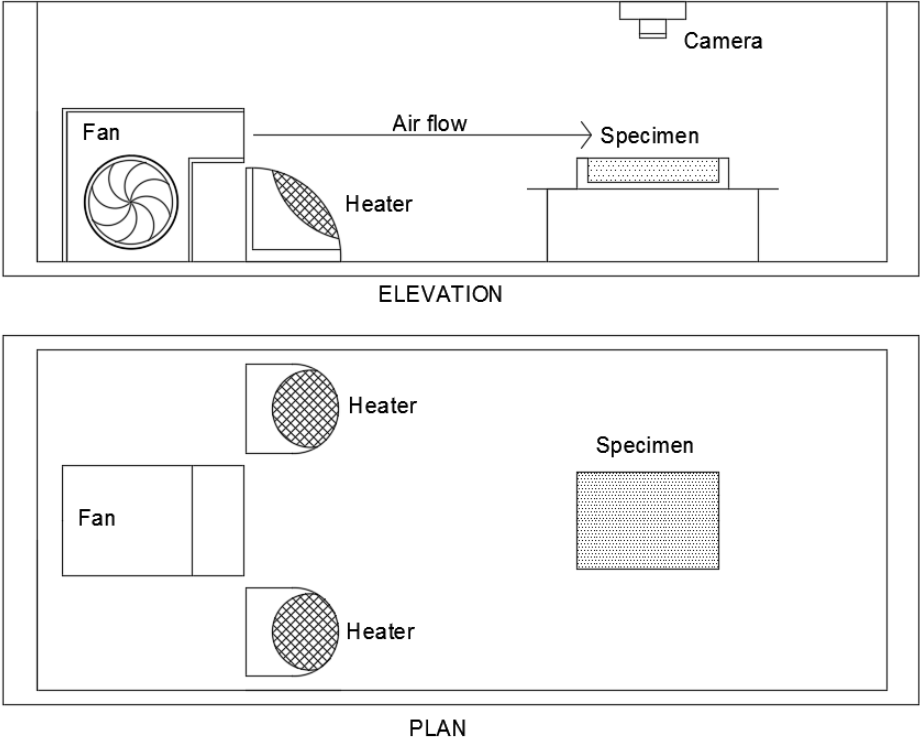


Figure 3.1. Diagram of test setup.

3.4 Camera specifications

The camera used in this work was a digital single-lens reflex camera (Canon EOS 5D) with a standard prime lens. Canon EOS 5D has a full-frame CMOS sensor which can provide a resolution approximately 12.8 megapixels. The standard prime lens has a fixed focal length of 50 mm. The f-stop, ISO, exposure time were set at 4, 400, and 1/20 second, respectively. These settings were found by trial and error to ensure proper exposure under the laboratory lighting conditions. All images were taken and saved in Canon’s CR2 raw format.

3.5 Water evaporation tests

As discussed in the literature review, the concrete or cement paste surface is considered as a textureless structure. In order to evaluate the strain evolution on a freshly cast concrete or cement paste surface by using DIC, a black or white spray paint has to be applied onto the concrete or cement paste surface to create a unique spackle pattern. In this project, a commercially available white spray paint was selected to create the speckle pattern. (An explanation is given in section 3.8.) However, plastic shrinkage cracking is highly dependent on the rapid surface drying. The spray paint applied onto the surface of a freshly cast concrete or cement paste specimen may delay or prevent the surface drying. Thus, it is necessary to study the effect of the spray paint on the water evaporation rate of concrete in the first place.

A digital scale with a capacity of 8 kg and an accuracy of 0.1 g was used to measure the mass of the concrete specimen upon drying. Due to the capacity of the digital scale, concrete was cast in a 325 mm long, 215 mm wide, and 60 mm deep plastic form. Freshly cast concrete specimens with and without the spray paint were then separately placed on the digital scale in the environmental chamber for the first 6 hours after placement. The mass of concrete specimen, air temperature, relative humidity, wind velocity, and concrete temperature were recorded every 30 minutes. The water evaporation rate of concrete was determined by dividing the mass loss between two successive mass determinations by the surface area of the concrete specimen and the 30-minute time interval. The water evaporation rate was also calculated by the water evaporation equation (Equation 2) for comparison.

3.6 ASTM standard C1579 procedure

3.6.1 Specimen geometry

The specimen geometry used in this section was adopted from ASTM Standard C1579-13, as shown in Figure 3.2. The four sides of the form were fabricated from plywood, while the base of the form and the risers were made of a rigid PVC sheet. The form was 560 mm long, 355 mm wide, and 100 mm deep. A 63.5 mm high stress riser was placed in the center of the form, and two 32 mm high stress risers were placed 90 mm inward from both ends.



Figure 3.2. Specimen form with stress risers.

3.6.2 Testing procedure

The concrete used in this work was made up of water, cement, and aggregates, which did not contain any supplementary cementitious materials or admixtures. A cement content of 460 kg/m³ was selected, which was intended to increase the likelihood of plastic shrinkage cracking. The concrete mixture design is shown in Table 3.1.

Table 3.1. Concrete mixture proportions.

w/c	Cement (kg/m ³)	Water (kg/m ³)	Coarse Aggregate (dry) (kg/m ³)	Fine Aggregate (dry) (kg/m ³)
0.50	460	230	853	693

Concrete was mixed by a pan-type mixer in the laboratory conforming to ASTM Standard C192/C192M-14. First, the coarse aggregate and some mixing water were added to the mixer, and mixed for a few revolutions. Then, the cement, fine aggregate, and the rest of mixing water were added to the mixer. All ingredients were mixed for 3 minutes, followed by a 3 minutes rest, and a 2 minutes final mixing.

Freshly mixed concrete was then cast into the form in one layer. Next, the concrete specimen was consolidated by a vibrating table for about 20 seconds. After consolidation, a straightedge was used to screed the concrete specimen for three times. The motion of screeding was perpendicular to the stress riser. In order to obtain a smooth surface, the concrete specimen was floated by a trowel.

After finishing the concrete, the spray paint was applied onto the finished concrete surface. The concrete specimen was then placed in the environmental chamber. In order to capture the whole surface area of the concrete specimen, the camera was fixed to a wood frame approximately 95 cm above the concrete surface. Images were captured from then onwards at 10-minute intervals. Air temperature, relative humidity, wind velocity, and concrete temperature were recorded every 30 minutes.

According to ASTM Standard C1579-13, the experiment is terminated at the time of final set. Generally, the time of final set is less than 6 hours for normal concrete, so it is not necessary to determine the time of final set (Aldalinsi et al., 2013). In the experiment, the image acquisition was terminated at 6 hours after the concrete specimen was placed in the environmental chamber.

3.7 Cement paste testing procedure

3.7.1 Specimen geometry

The plastic form adopted from Wang et al. (2001) had a surface area of 179×137 mm, and a depth of 6 mm. A piece of sandpaper was attached to the bottom of the form using double-sided tape. In order to eliminate the effect of water absorption by sandpaper, a type of waterproof sandpaper was selected. Different grits of sandpaper were used to investigate restraint.

3.7.2 Testing procedure

The cement paste used in this work was made up of cement and water. Cement and water were mixed for 30 seconds by an electrical mixer conforming to ASTM Standard C305-14. The cement paste was then cast into the form with the sandpaper attached to the bottom. A straightedge was used to level the surface of the cement paste specimen. After finishing the cement paste specimen, the spray paint was applied onto the cement paste surface. The cement paste specimen was then placed in the environmental chamber. The camera was fixed to a copy stand approximately 46 cm above the cement paste surface. Images were captured from then onwards at 10-minute intervals. After the time to first crack, images were captured at 1-minute interval for 10 minutes. Air temperature, relative humidity, wind velocity, and cement paste temperature were recorded every

30 minutes. The duration of drying for the cement paste specimen was set as 90 minutes based on the size of the cement paste specimen.

For the set of experiments to evaluate the effect of air temperature on plastic shrinkage cracking, cement paste specimens with a w/c of 0.45 were tested separately in the environmental chamber with three different air temperatures. Different air temperatures were achieved by adjusting the settings of two electrical fan heaters inside the environmental chamber.

For the set of experiments to evaluate the effect of wind velocity on plastic shrinkage cracking, cement paste specimens with a w/c of 0.45 were tested separately in the environmental chamber with three different wind velocities. Different wind velocities were achieved by running the electrical fan on different speeds.

For the set of experiments to evaluate the effect of w/c on plastic shrinkage cracking, cement paste specimens with w/c of 0.35, 0.40, 0.45, and 0.50 were tested separately in the environmental chamber with the same air temperature, relative humidity, and wind velocity.

For the set of experiments to evaluate the effect of substrate roughness on plastic shrinkage cracking, cement paste specimens with a w/c of 0.45 were cast on duct tape (without sandpaper), No. 180 sandpaper (fine), and No. 40 sandpaper (coarse), and tested separately in the environmental chamber with the same air temperature, relative humidity, and wind velocity.

3.8 Image analysis techniques

In this project, two image analysis techniques were used to evaluate the behavior of plastic shrinkage cracking in cement-based materials. DIC is based on tracking speckle patterns before and after a deformation. As discussed in the literature review, the concrete or cement paste surface

is considered as a textureless structure; therefore, a unique speckle pattern has to be applied onto the concrete or cement paste surface. However, the principal idea of the MATLAB script is to extract the crack contours by replacing pixels depending on grayscale intensity. In a grayscale image, the weakest intensity is black, while the strongest is white. As discussed in section 2.6.2, the minimum intensity value is located in the center of the crack. In order to eliminate the effect of the speckle pattern on the results of crack areas computed in MATLAB, white spray paint was selected in this project.

For image analysis purposes, Canon's CR2 raw images were converted to TIF format, and lens distortion of each image was corrected in an image-editing program, such as Photoshop. All the images of the cement paste specimens were cropped to a size of 3003×2336 pixels only including the cement paste surface. In the following sections, the details on the MATLAB script and the software VIC-2D are presented.

3.8.1 MATLAB script to determine crack area

The MATLAB script was written based on Qi et al. (2003) and Banthia and Gupta (2009). Figure 3.3 shows an example of the image processing procedure using MATLAB.

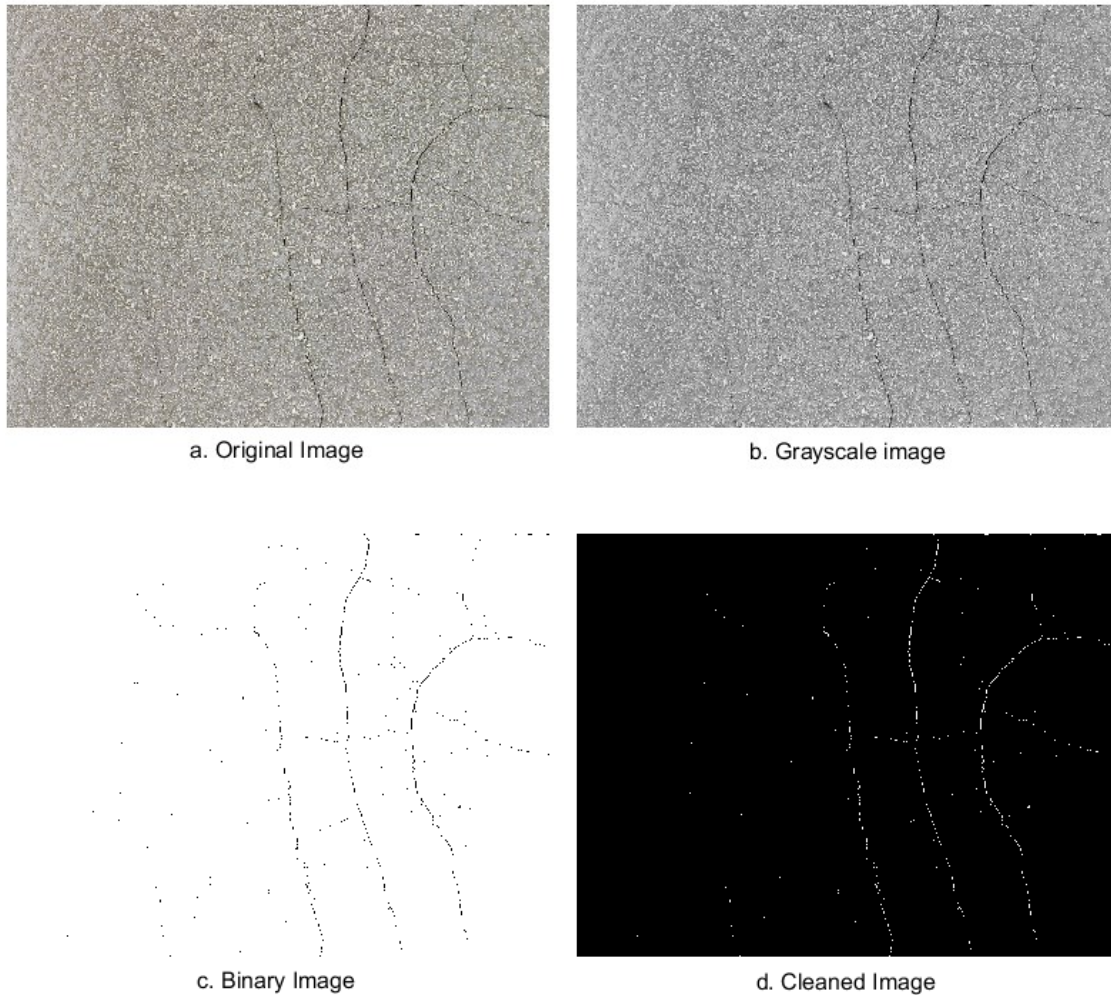


Figure 3.3. Image processing procedure using MATLAB: (a) original image, (b) grayscale image, (c) binary image, (d) cleaned image.

First, the original image was converted to a grayscale image, as shown in Figure 3.3 (a) and (b). Then, the grayscale image was converted to a binary image, as shown in Figure 3.3 (c). To complete this step, a level value ranging between 0 and 1 should be specified in MATLAB. The pixels with the intensity values less than the level were replaced by the black pixel (value 0), and all other pixels were replaced by the white pixel (value 1). Thus, the crack was extracted as a black contour in a white background. The selection of the level value was dependent on the operator's

judgement. In this project, a level value of 0.30 was selected based on the comparison between the crack contours in the original image and the binary images obtained using different level values. As shown in Figure 3.4, the crack contours displayed in the binary image obtained using the level value of 0.30 were relatively clear, while some crack contours were eroded when using the level value of 0.25, and the crack contours were hard to distinguish from the background when using the level values of 0.35 and 0.40.

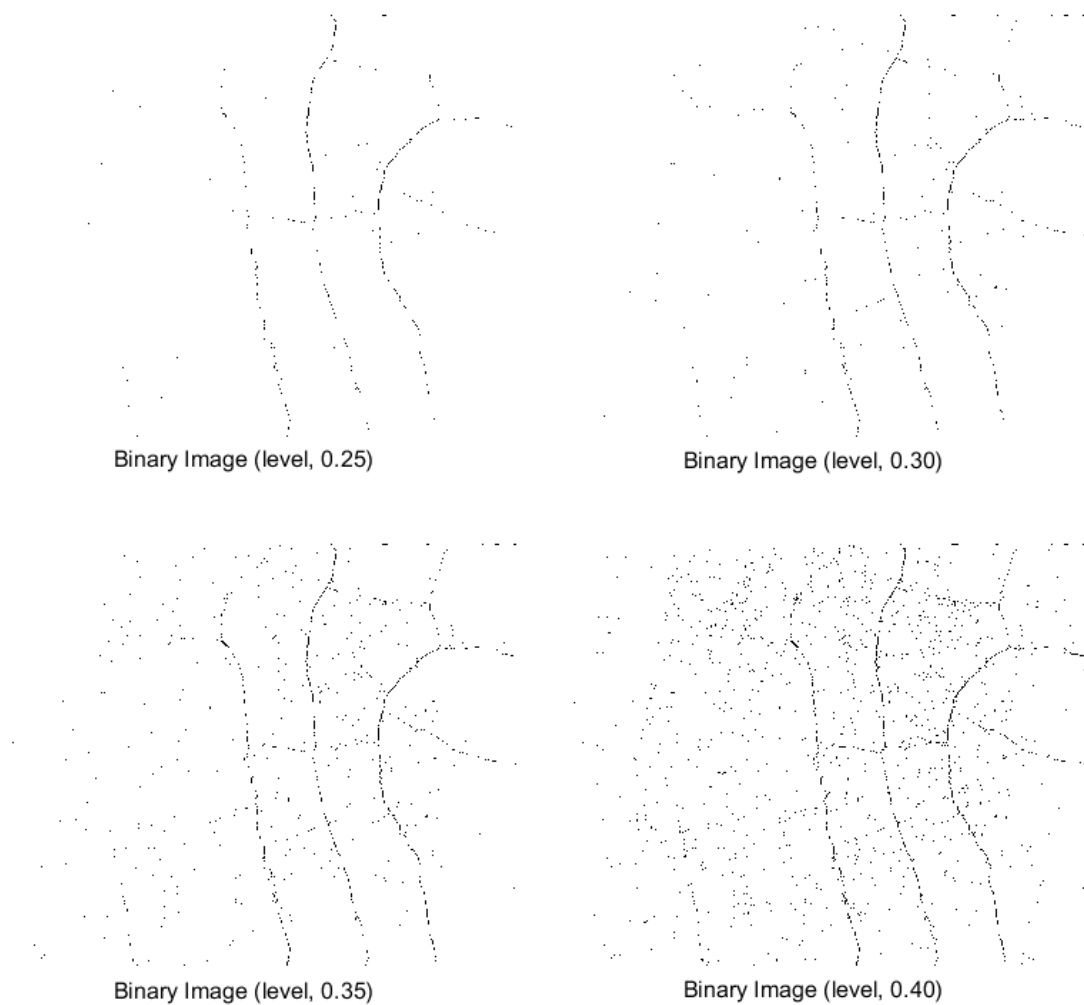


Figure 3.4. Binary images obtained using the level values of 0.25, 0.30, 0.35, and 0.40.

In order to count the pixels inside the cracks, black pixels (value 0) and white pixels (value 1) were reversed. As shown in Figure 3.3 (c), other than the crack contours, some black points were also extracted in the binary image because of the surface voids that were formed during the drying process showing similar grayscale intensities to the cracks. Thus, the binary image was cleaned by a MATLAB function, which the objects fewer than 8 pixels (default value) were removed, as shown in Figure 3.3 (d). By doing so, the pixels inside the cracks can be counted. Before starting the experiment, a crack comparator was placed beside the cement paste specimen. A calibration factor can be established by counting the pixels in a known area in the crack comparator; therefore, the crack area can be determined. The MATLAB script is presented in Appendix A.

As shown in Figure 3.3 (d), even though any connected points fewer than 8 pixels were removed, there were still some isolated points can be seen in the cleaned image. Thus, the crack area computed in MATLAB also included the area of some large air pockets as a result of surface drying. As the crack contours were extracted based on grayscale intensities, any changes in surface color of the specimen or laboratory lighting conditions could cause the fluctuations of the results computed in MATLAB.

3.8.2 VIC-2D

VIC-2D is an easy to use image analysis software based on DIC. It can measure in-plane strains from 50 microstrain to 2000% strain of every data point within the measurement area (VIC-2D Reference Manual, 2009). The images were first opened in the VIC-2D software. The image taken at the beginning of the experiment was set as the reference image. An area of interest (AOI) was then selected on the reference image. The subset size controls the size of each data point that is used to track the displacement between images. Each data point is separated from the next by the

step size (VIC-2D Reference Manual, 2009). The default subset size is 21, and the default step size is 5. According to Sutton et al. (2009), to ensure accurate correlation results, each data point (subset size \times subset size) should contain at least three speckles, and the step size should be roughly $\frac{1}{4}$ of the subset size. In this project, the subset size and the step size were set as 63 and 15, respectively. Figure 3.5 shows the partial enlargement view of a speckled image with a grid of 63 \times 63 pixels. As shown in Figure 3.5, each data point contained at least 3 speckles. In case that the wet surface and the wind may break down the speckle pattern, incremental correlation was chosen, which each image was correlated to the previous image rather than the reference image.

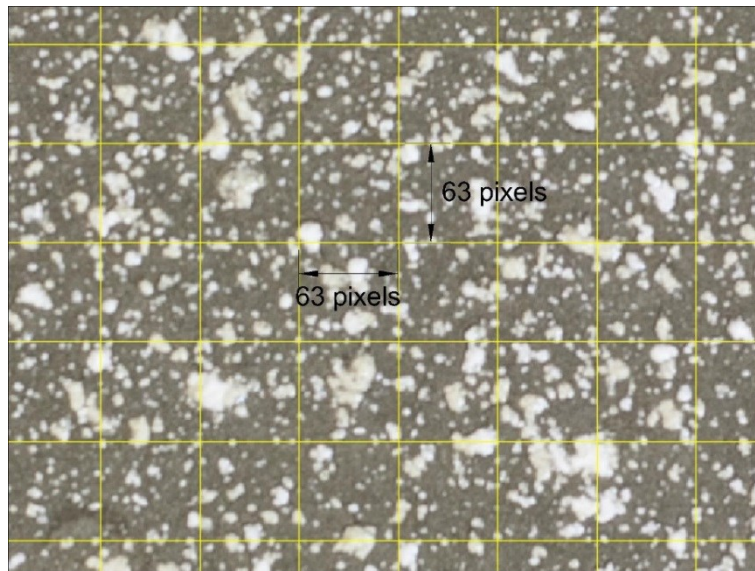


Figure 3.5. Partial enlarged view of a speckled image with a grid of 63 \times 63 pixels.

4 RESULTS AND DISCUSSION

4.1 Introduction

In this chapter, the results of the water evaporation tests are presented first. The water evaporation rates of concrete calculated by mass loss and the water evaporation equation (Equation 2) are compared. The effect of the spray paint on the water evaporation rate of concrete is discussed. Second, the DIC analysis results and crack areas computed in MATLAB are presented. A set of image analysis results by both techniques is used to explain the process of plastic shrinkage cracking. The effects of air temperature, wind velocity, w/c, and substrate roughness on plastic shrinkage cracking are discussed. Finally, a set of DIC analysis results is used to discuss the reasons that no cracking occurred in the concrete specimens prepared conforming to ASTM Standard C1579.

4.2 Evaluation of the water evaporation equation

In this section, the water evaporation rates of the concrete specimen (325×215×60 mm) without spray paint were calculated by mass loss and the water evaporation equation (Equation 2), respectively. The value calculated by mass loss is the actual water evaporation rate of concrete for each 30-minute time interval, while the value calculated by the water evaporation equation is based on simultaneous air and concrete temperatures, relative humidity, and wind velocity recorded every 30 minutes. The results are presented in Figure 4.1. The details on the environmental variables and the water evaporation rates for the concrete specimens with and without spray paint are presented in Appendix B (see Tables B.1 and B.2).

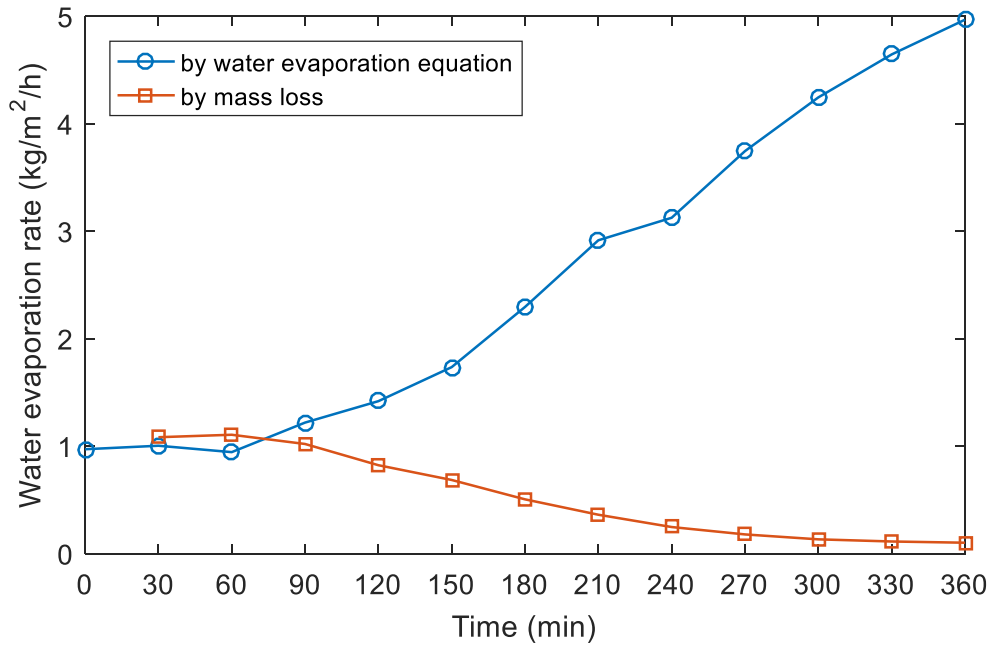


Figure 4.1. Water evaporation rates calculated by mass loss and the water evaporation equation in the first 6 hours.

Bakhshi and Mobasher (2011) divided the early age drying of cement-based materials into two stages (stage I and stage II). In stage I, the cement-based materials had a constant water evaporation rate, while stage II was an decreasing water evaporation rate period. As shown in Figure 4.1, the water evaporation rates calculated by both methods were almost constant and similar in the first 90 minutes after starting the experiment, indicating the concrete specimen was in stage I drying. After that, the actual water evaporation rate dropped gradually, indicating the concrete specimen entered stage II drying period. However, the water evaporation rate calculated by the water evaporation equation increased significantly over time.

The actual water evaporation rate decreased over time because the water content in the concrete surface reached a critical value (Bakhshi and Mobasher, 2011). Figure 4.2 shows the air and

concrete temperatures that were monitored during the experiment. As shown in Figure 4.2, the concrete specimen began to increase in temperature due to the heated air approximately 90 minutes after starting the experiment. According to the water evaporation equation (Equation 2), concrete temperature is positively correlated with the water evaporation rate; therefore, a rise in concrete temperature increased the values calculated by the water evaporation equation after 90 minutes.

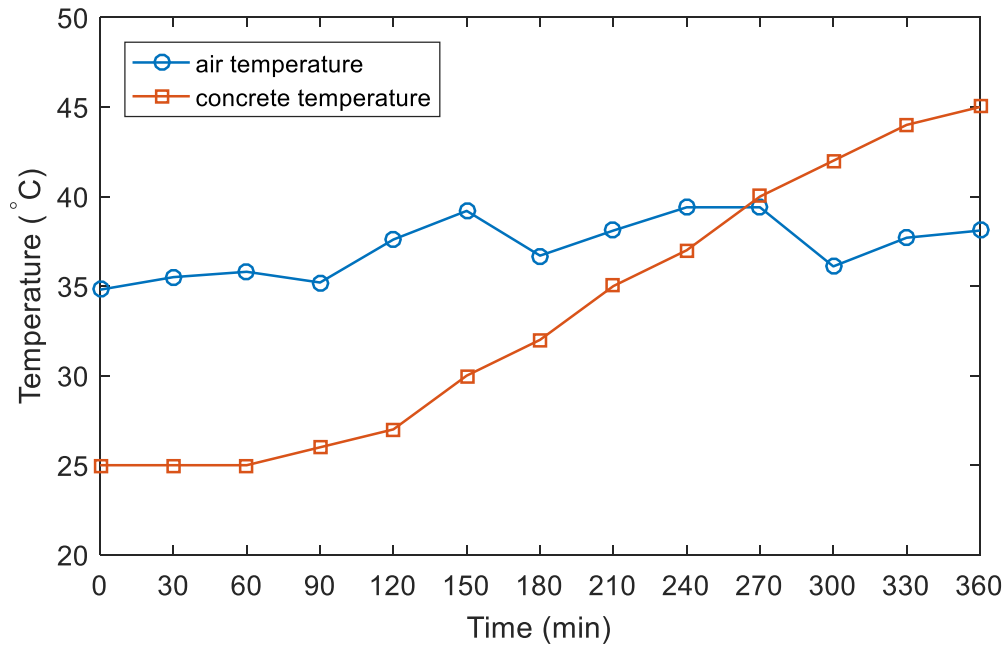


Figure 4.2. Air and concrete temperatures in the first 6 hours.

It is also worth mentioning that the concrete temperature had no apparent change in the first 90 minutes. In the experiment, the measurements of concrete temperature were taken by a dial pocket thermometer. It is widely accepted that water has higher specific heat capacity than concrete; therefore, it took time to heat the concrete specimen in the beginning of the experiment due to the presence of water. Another reasonable explanation could be the temperature rise caused by the hot air and cement hydration was offset by the temperature drop caused by surface water evaporation.

As a result, a rise in concrete temperature not only caused invalid water evaporation rates calculated by the water evaporation equation, but also indicated that there was less water to evaporate from the concrete surface at this time.

4.3 Effect of spray paint on water evaporation rate

The results of the water evaporation rates of the concrete specimens with and without spray paint calculated by mass loss, as a function of time, are presented in Figure 4.3.

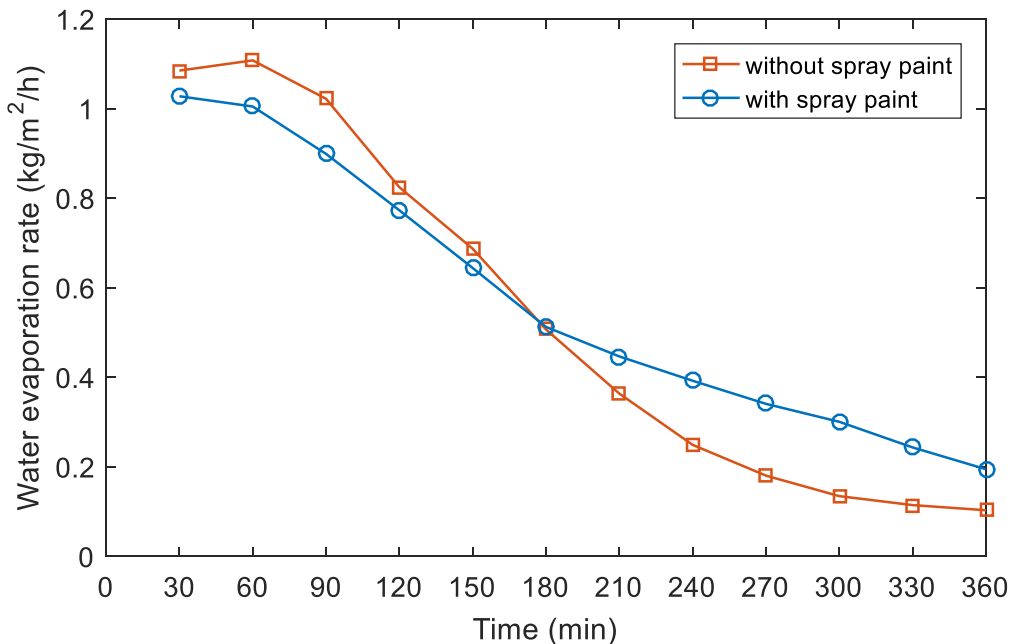


Figure 4.3. Water evaporation rates of the concrete specimens with and without spray paint in the first 6 hours.

As shown in Figure 4.3, the water evaporation rate of the concrete specimen with spray paint was slightly lower than that of the concrete specimen without spray paint in the first 180 minutes after starting the experiment. As discussed in section 2.4.1, when the water evaporation rate of concrete exceeds 1 kg/m²/h, plastic shrinkage cracking is likely to occur. Compared with the water

evaporation rate of the concrete specimen without spray paint that was higher than $1 \text{ kg/m}^2/\text{h}$ in the first 90 minutes, the decrease in the water evaporation rate during this time could reduce the likelihood of plastic shrinkage cracking in the concrete specimen with spray paint.

After 180 minutes, the water evaporation rate of the concrete specimen with spray paint began to exceed the water evaporation rate of the concrete specimen without spray paint. In the first 6 hours, the percentages of total mass loss for the concrete specimens with and without spray paint were 2.96% and 2.79%, respectively. The percentages of mass loss in the first 180 minutes to the total mass loss for the concrete specimens with and without spray paint were 71.71% and 82.05%, respectively.

Even though the spray paint increased the total amount of water evaporated from the concrete surface, it somewhat delayed the water evaporation in the first 180 minutes after starting the experiment. According to Slowik et al. (2008), the risk of plastic shrinkage cracking reaches its maximum when air starts to penetrate the gaps between the solid particles near the top surface of concrete. Thus, a delay in water evaporation which may delay the time of air penetration could also reduce the likelihood of plastic shrinkage cracking in the concrete specimen with spray paint.

4.4 Evaluation of the process of plastic shrinkage cracking

In this section, the image analysis results by MATLAB and VIC-2D of the cement paste specimen with a w/c of 0.40 are presented and discussed in order to investigate the process of plastic shrinkage cracking. The average air temperature, relative humidity, and wind velocity during the experiment were $42.5 \text{ }^\circ\text{C}$, 14.9%, and 9.1 m/s , respectively.

Figure 4.4 shows the crack area of the cement paste specimen during the experiment. In the experiment, the first crack occurred at 28 minutes after starting the experiment. However, as shown in Figure 4.4, the values of crack area computed in MATLAB were not zero before the time to first crack, indicating that some large air pockets were formed upon drying before the first crack occurred. After the time to first crack, the crack area increased significantly in the next 12 minutes, growing from 20.59 mm² to 63.44mm². Then, the crack area increased slowly and eventually stabilized. As discussed in section 3.8.1, the reason that the crack area increased at the termination of the experiment could be the changes in surface color of the cement paste specimen upon drying.

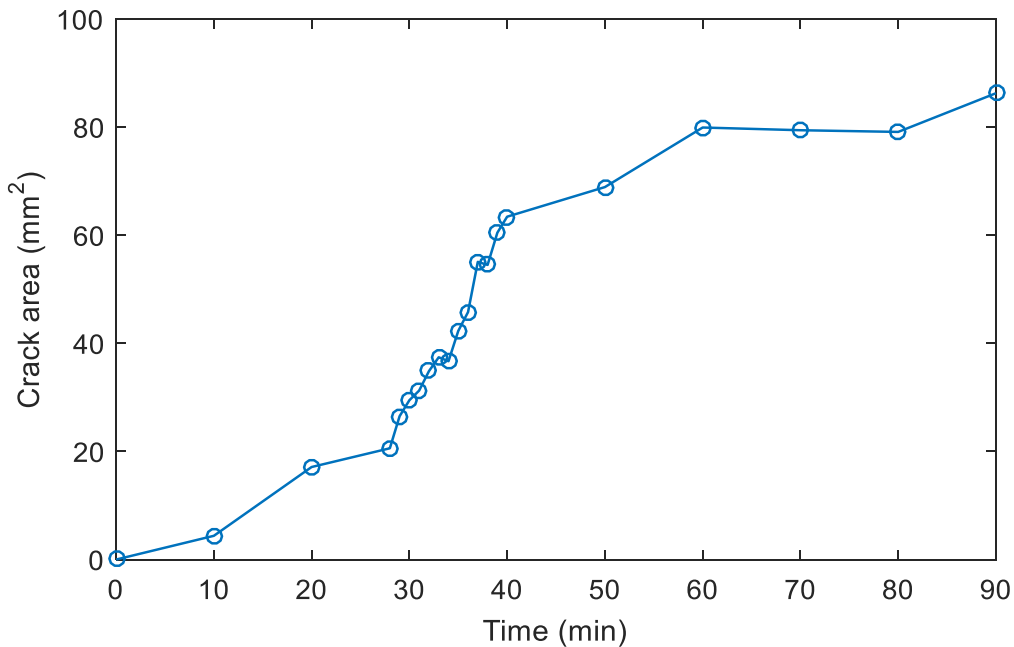


Figure 4.4. Crack area of the cement paste specimen with the w/c 0.40 over time.

In order to investigate the process of plastic shrinkage cracking, a series of image analysis results by VIC-2D is presented and discussed in the following paragraphs. When using DIC to evaluate plastic shrinkage, plastic settlement can be considered as out-of-plane motion, which may cause

false correlations. However, as discussed in the literature review, plastic settlement mainly occurred before plastic shrinkage. In addition, the incremental correlation was chosen in this project. Thus, the effect of plastic settlement on the correlation results is assumed negligible in this project.

In the experiment, the direction of wind flow was parallel to the longer side of the cement paste specimen. The orientation parallel to the wind direction was defined as x-direction, and the orientation perpendicular to the wind direction was defined as y-direction. An arbitrary horizontal line was drawn along the center of the rectangular correlated images. Figures 4.5 to 4.12 show the original images, binary images, contour maps of strains in the x-direction (e_{xx}), and figures showing the e_{xx} of 101 data points on the horizontal line at different points in time throughout the experiment. In the figures, a positive value indicates tensile strain, while negative value indicates compressive strain (VIC-2D Reference Manual, 2009). The size of the images was 3003×2336 pixels. The scale of the images was 17.10 pixels/mm. For the contour maps, the color scale is the same for all images with red indicating maximum tensile strain and purple indicating maximum compressive strain.

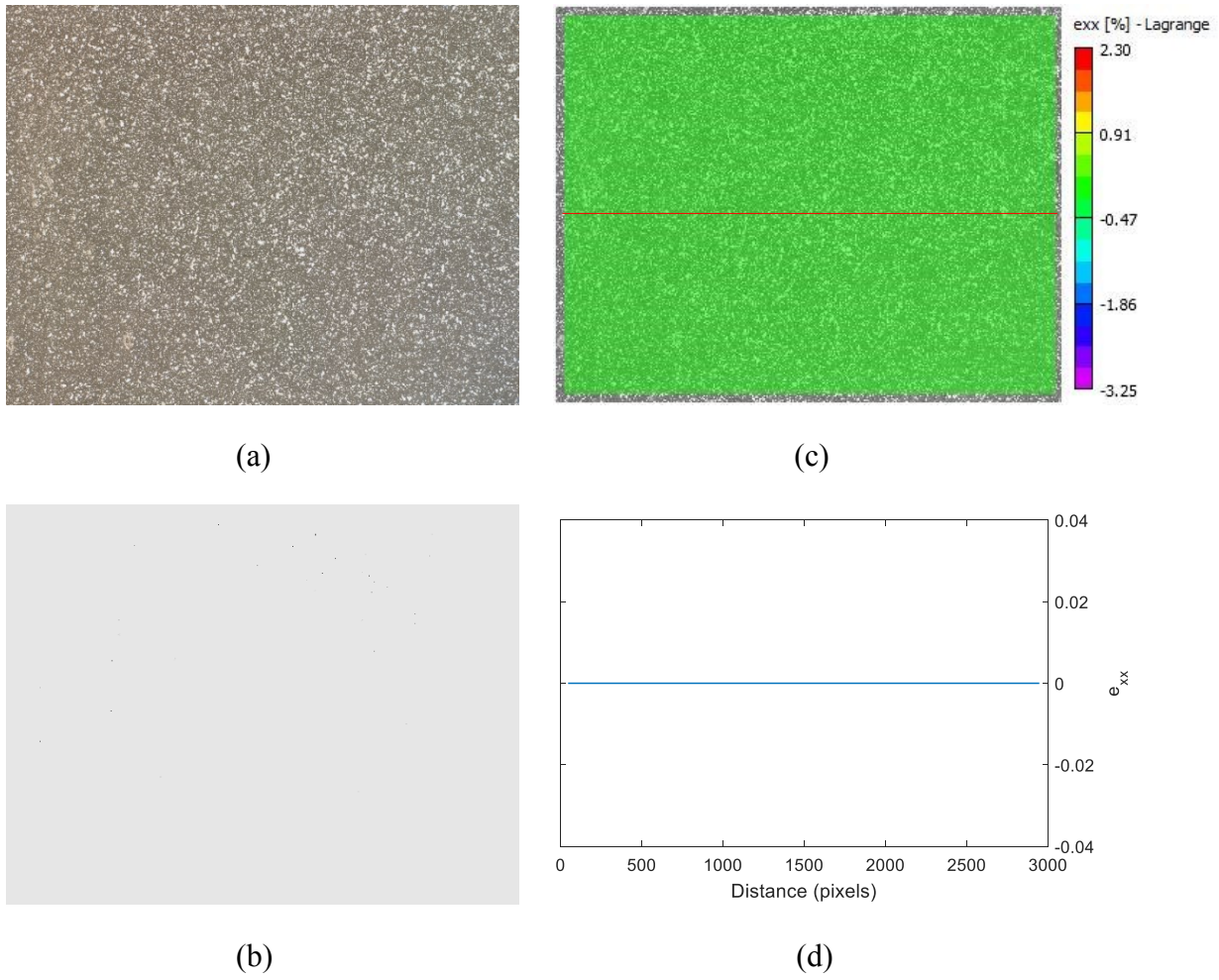


Figure 4.5. Original image (a), binary image (b), contour map of e_{xx} on the cement paste surface (c), and e_{xx} on the horizontal line (d) at the beginning of the experiment.

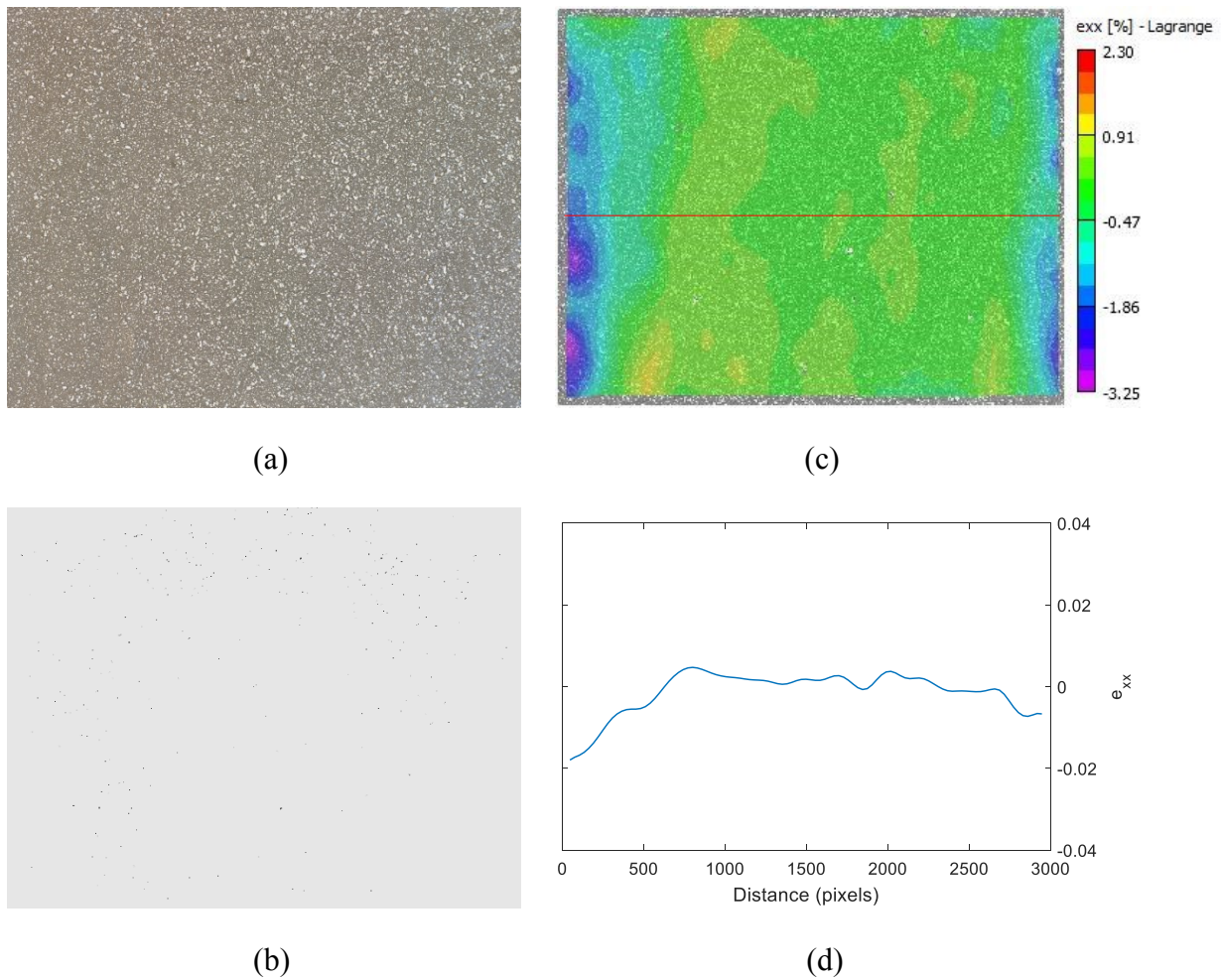


Figure 4.6. Original image (a), binary image (b), contour map of e_{xx} on the cement paste surface (c), and e_{xx} on the horizontal line (d) at 10 minutes after starting the experiment.

As shown in Figure 4.5, at the beginning of the experiment, no strain in the x-direction occurred, and the e_{xx} on the horizontal line were zero. Ten minutes later, as shown in Figure 4.6, the compressive strains in the x-direction accumulated near the two shorter sides of the specimen, indicating that the cement paste began to shrink from the edges of the form. In the meanwhile, some tensile strains in the x-direction can be seen in the middle part of the specimen, indicating that a tensile stress was developed due to the shrinkage difference between the surface and the bottom of the cement paste specimen.

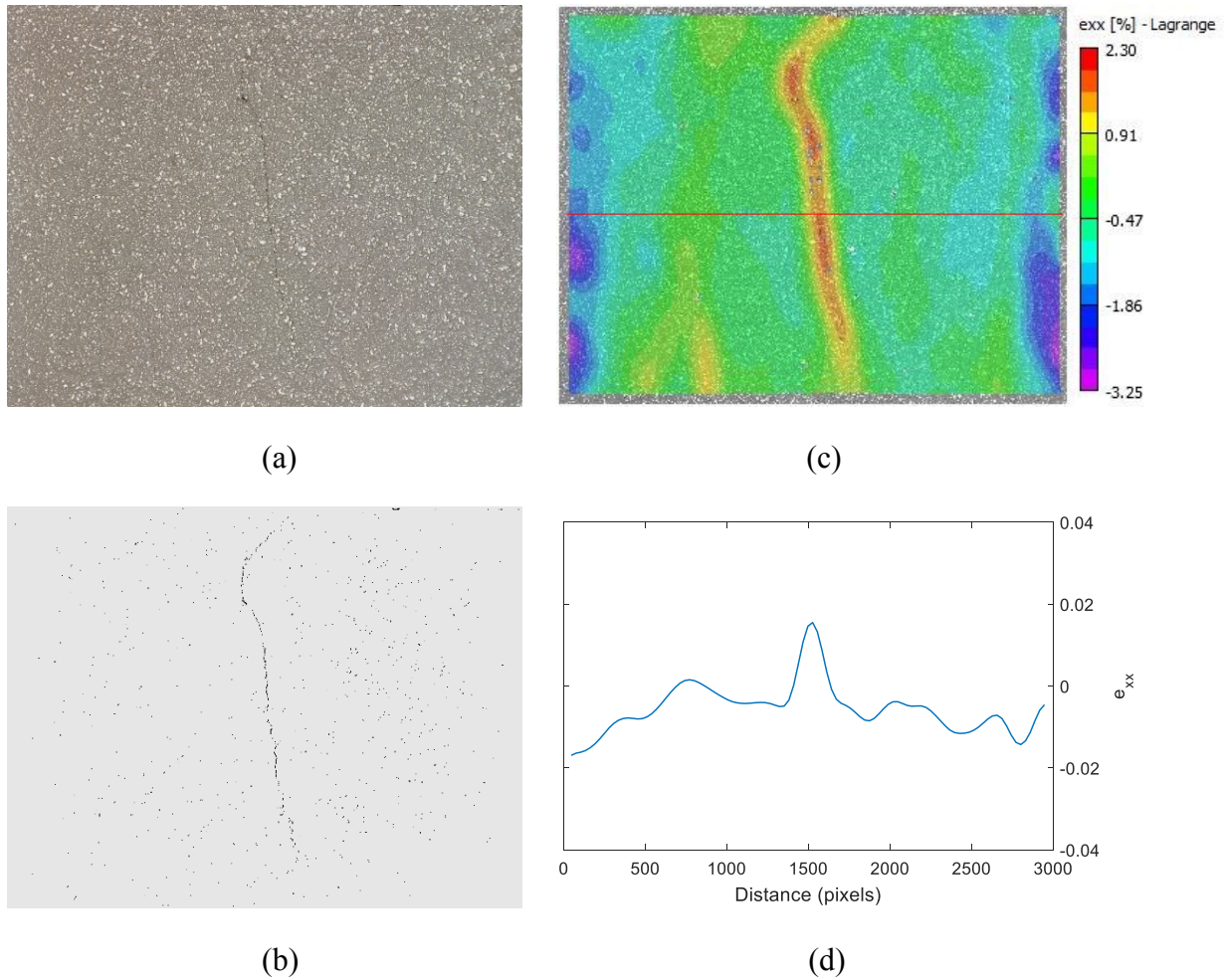


Figure 4.7. Original image (a), binary image (b), contour map of e_{xx} on the cement paste surface (c), and e_{xx} on the horizontal line (d) at 28 minutes after starting the experiment.

As shown in Figure 4.7, more compressive strains in the x -direction accumulated near the two shorter sides of the specimen as a result of further shrinkage. In the experiment, the first surface crack occurred at 28 minutes after starting the experiment. The tensile strains in the x -direction accumulated in the area near the crack, making the crack distinct in the contour map. Accordingly, a peak in e_{xx} occurred on the horizontal line, which corresponded to the crack location. This process can be explained as a strain localization taking place on the specimen surface due to the increasing shrinkage difference between the surface and the bottom of the cement paste specimen.

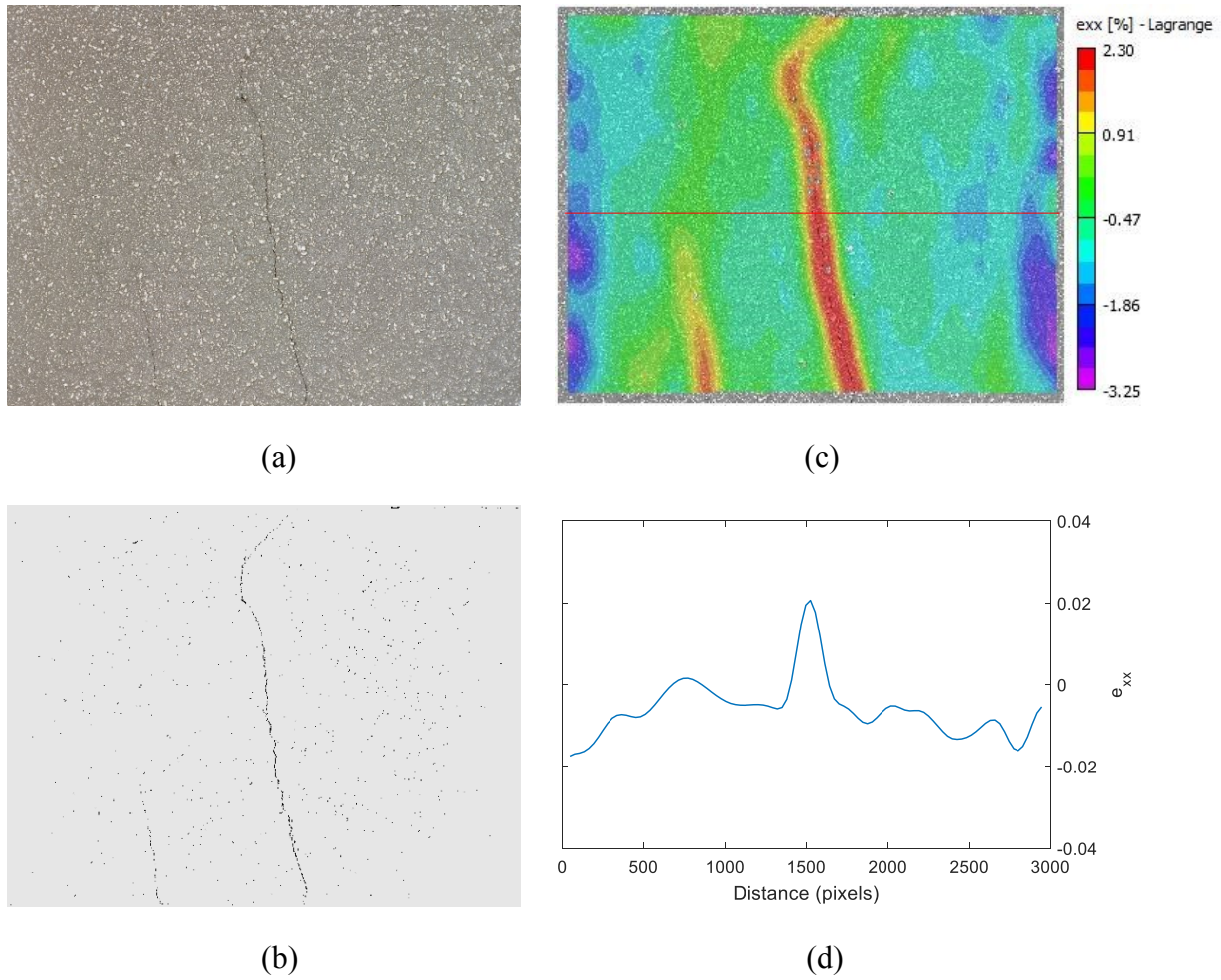


Figure 4.8. Original image (a), binary image (b), contour map of e_{xx} on the cement paste surface (c), and e_{xx} on the horizontal line (d) at 30 minutes after starting the experiment.

After the occurrence of the first crack, the tensile strains in the x-direction continued to accumulate in the area near the crack, and the peak value of e_{xx} on the horizontal line continued to increase. On the lower left part of the cement paste specimen, the second surface crack occurred at 30 minutes after starting the experiment, as shown in Figure 4.8. Although the crack does not intersect with the horizontal line along the center of the image, a small amount of tensile strain can be seen due to its formation (at approximately 750 pixels from the edge).

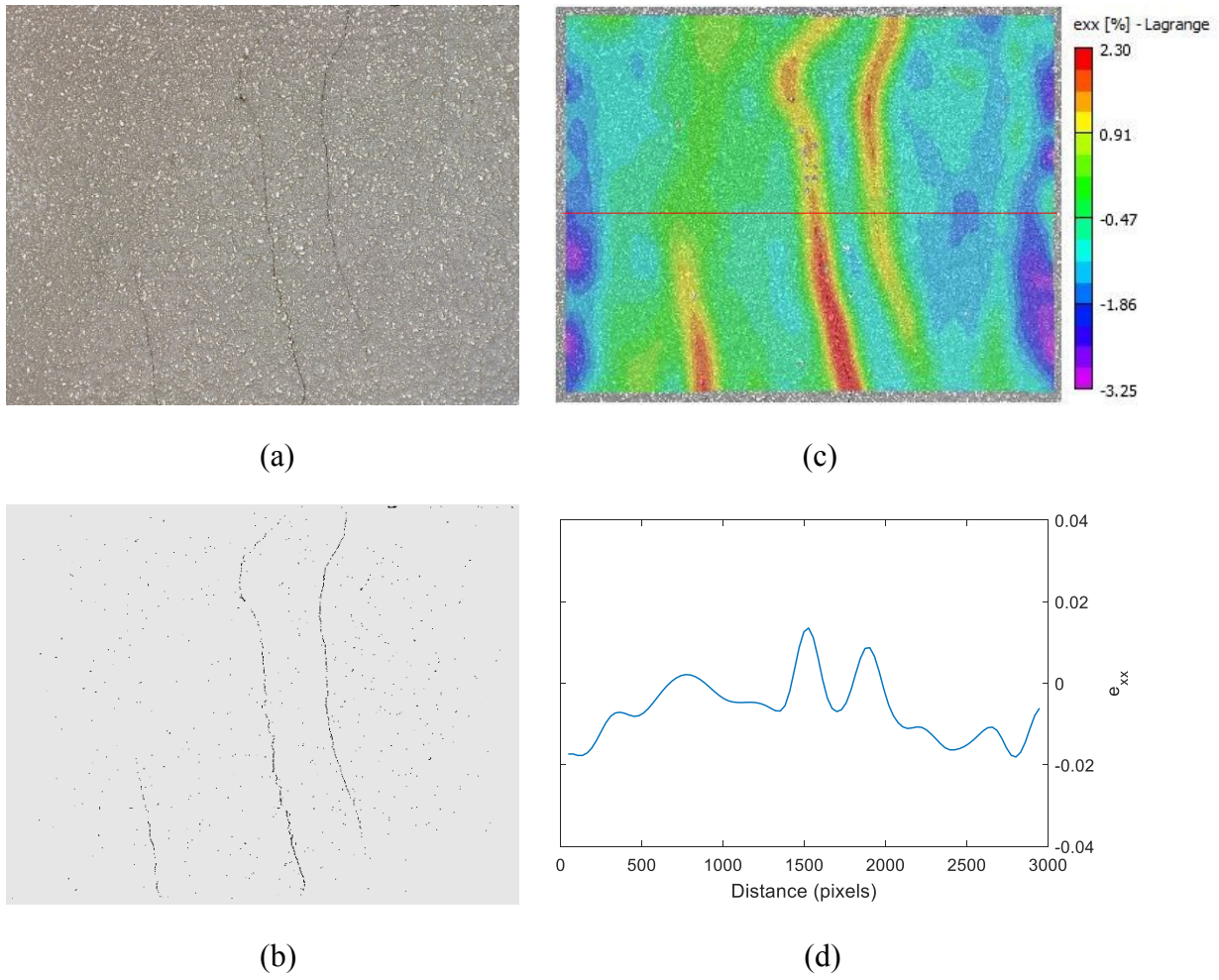


Figure 4.9. Original image (a), binary image (b), contour map of e_{xx} on the cement paste surface (c), and e_{xx} on the horizontal line (d) at 32 minutes after starting the experiment.

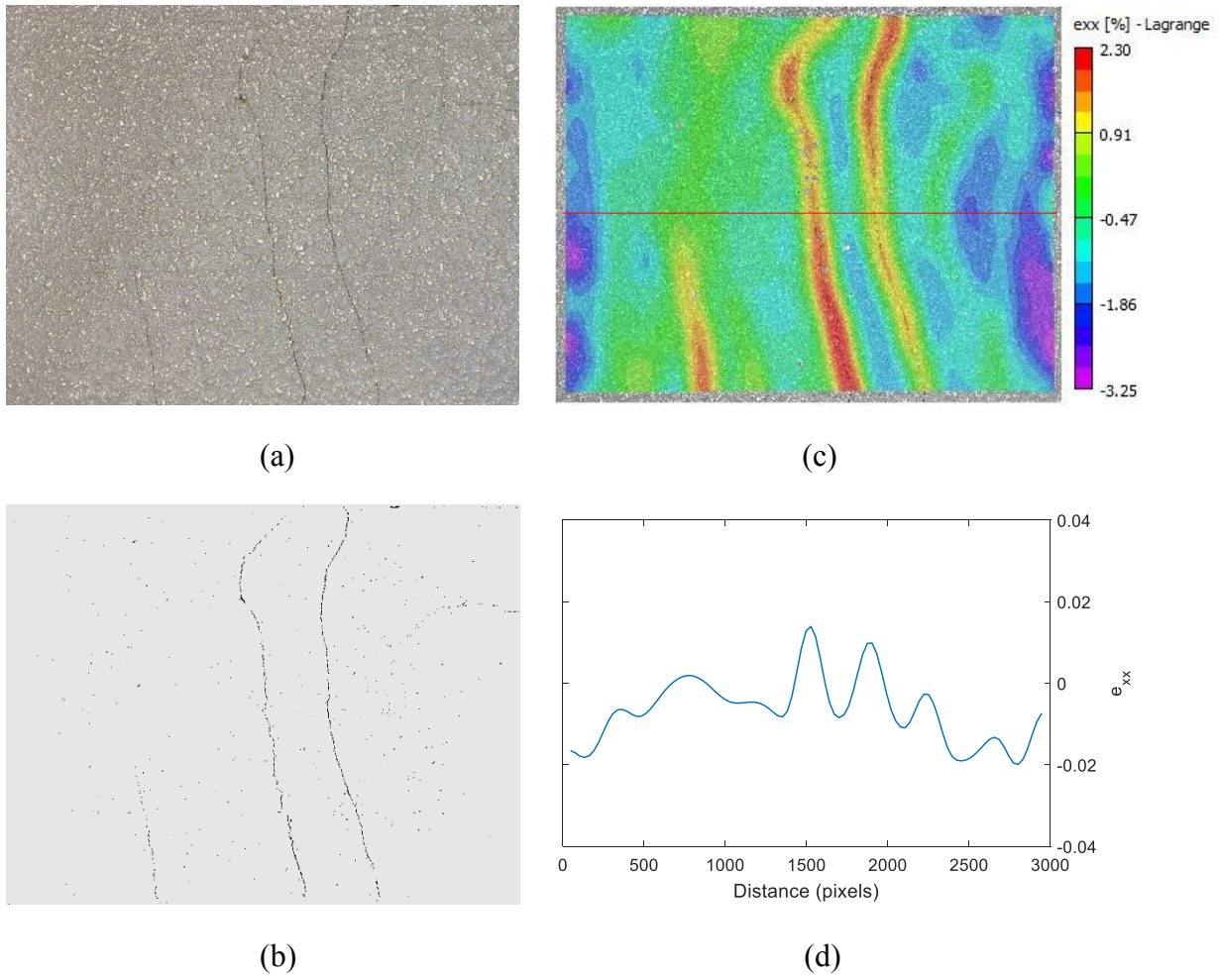


Figure 4.10. Original image (a), binary image (b), contour map of e_{xx} on the cement paste surface (c), and e_{xx} on the horizontal line (d) at 34 minutes after starting the experiment.

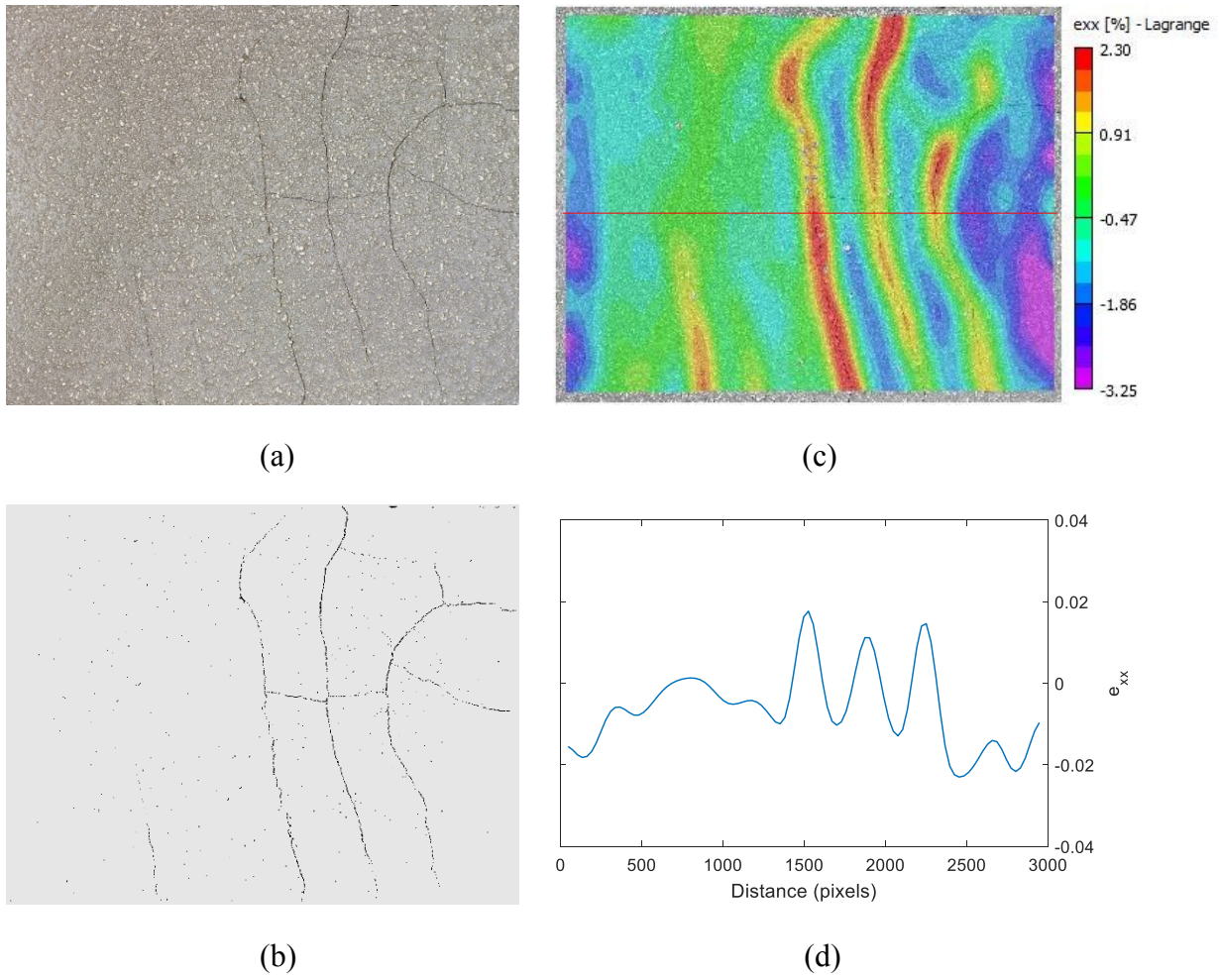


Figure 4.11. Original image (a), binary image (b), contour map of e_{xx} on the cement paste surface (c), and e_{xx} on the horizontal line (d) at 40 minutes after starting the experiment.

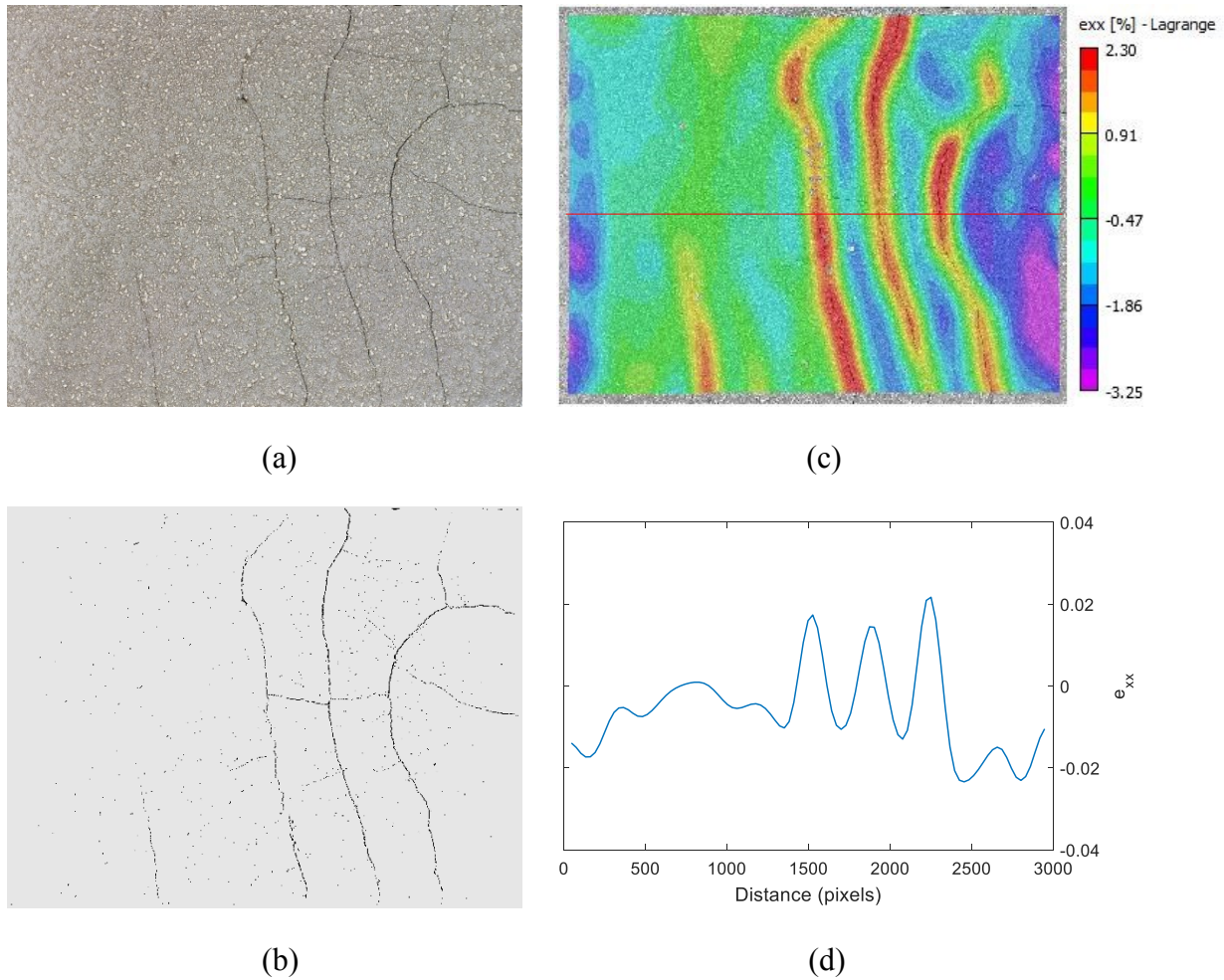


Figure 4.12. Original image (a), binary image (b), contour map of e_{xx} on the cement paste surface (c), and e_{xx} on the horizontal line (d) at 90 minutes after starting the experiment.

As shown in Figures 4.9 and 4.10, the third crack and the fourth crack can be seen in the contour maps at 32 and 34 minutes after starting the experiment, respectively. Accordingly, another two peaks in e_{xx} occurred on the horizontal line. As shown in Figures 4.11 and 4.12, more tensile strains in the x -direction accumulated in the area near the third crack and the fourth crack until the termination of the experiment. It can be noted that crack formation intersecting the horizontal center line resulted in sharp peaks; whereas the crack at the lower left not intersecting the line resulted in a more dispersed peak.

At the termination of the experiment, four peaks in e_{xx} occurred on the horizontal line, which corresponded to the first crack, the second crack, the third crack, and the fourth crack. Figure 4.13 shows the developments of three peak e_{xx} on the horizontal line over time. The second small peak is not shown.

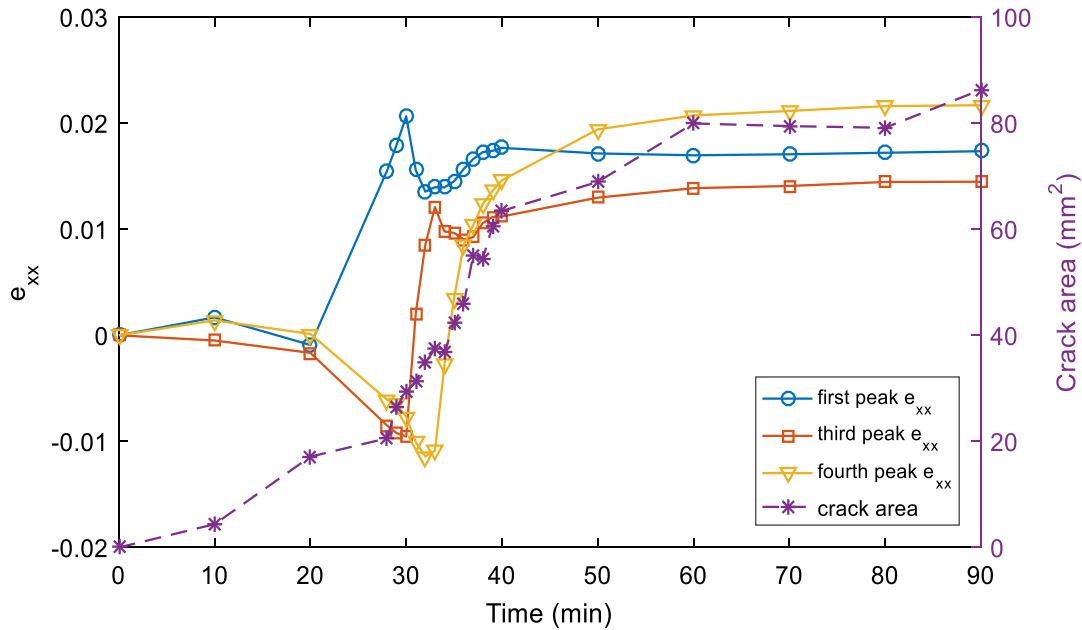


Figure 4.13. Developments of three peak e_{xx} on the horizontal line and crack area over time.

The location of the first peak e_{xx} corresponded to the first crack. After the first crack occurred at 28 minutes, the first peak e_{xx} continued to increase, and reached its highest point at 30 minutes. Then, the first peak e_{xx} decreased slightly, and flattened after 40 minutes.

The location of the third peak e_{xx} corresponded to the third crack. When the first peak e_{xx} began to decrease, the third peak e_{xx} started to increase. The location of the fourth peak e_{xx} corresponded to the fourth crack. The fourth peak e_{xx} then experienced a similar trend. When the third peak e_{xx} began to decrease, the fourth peak e_{xx} started to increase.

Based on the contour maps in Figures 4.5 to 4.12, the compressive strains in the x-direction first accumulated in the area near the both shorter sides of the specimen, indicating that the cement paste began to shrink from the edges upon drying. A strain localization then took place due to the shrinkage difference between the surface and the bottom of the cement paste specimen, which resulted in the first crack. After that, the tensile strains in the x-direction continued to accumulate in the area near the crack; therefore, the first crack became wider and deeper. As shown in Figures 4.4 and 4.13, the crack area increased significantly after the time to first crack, which correlated well to the developments of three peak strains. When the first crack penetrated to a certain depth, the surface of the cement paste specimen was then divided into two independent parts. At this point, the first crack can be considered as the edges of each new part. With continuous drying, each part then repeated the process of the first crack. The tensile strains in the x-direction in the area near the first crack were then offset by the compressive strains in the x-direction caused by shrinkage. Thus, a drop can be seen after the first and third peak e_{xx} reached their highest points. When the cement paste reached a shrinkage limit, the curves of three peak e_{xx} on the horizontal line flattened.

Theoretically, the major principal strain represents the maximum normal strain at a data point. As the tensile strains accumulated mainly in the area near the cracks, the contour map of major principal strains can be used to demonstrate the cracks that occurred in all directions, and the degree of tensile strain accumulation can be used to indicate the crack dimensions, as shown in Figure 4.14.

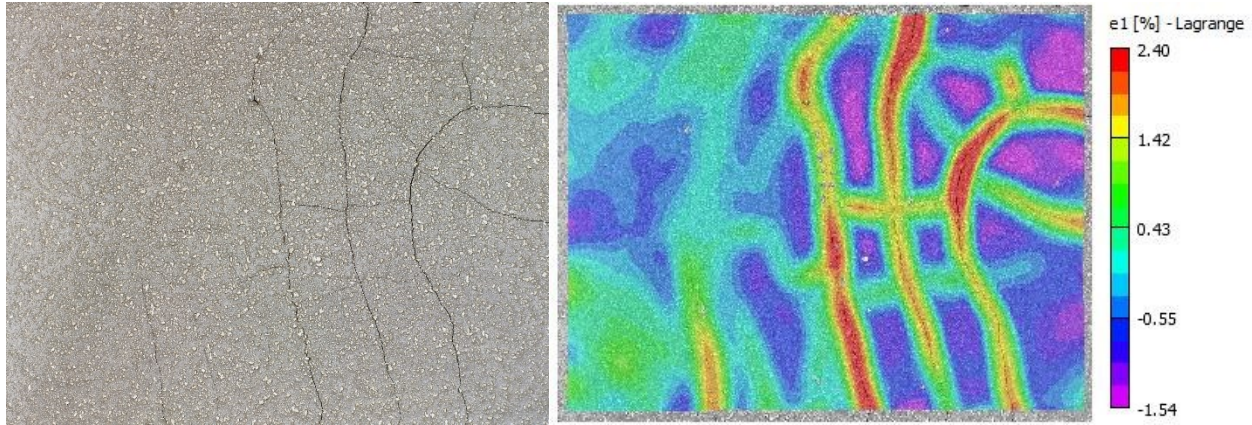


Figure 4.14. Original image and contour map of major principal strains at the termination of the experiment.

4.5 Effect of air temperature on plastic shrinkage cracking

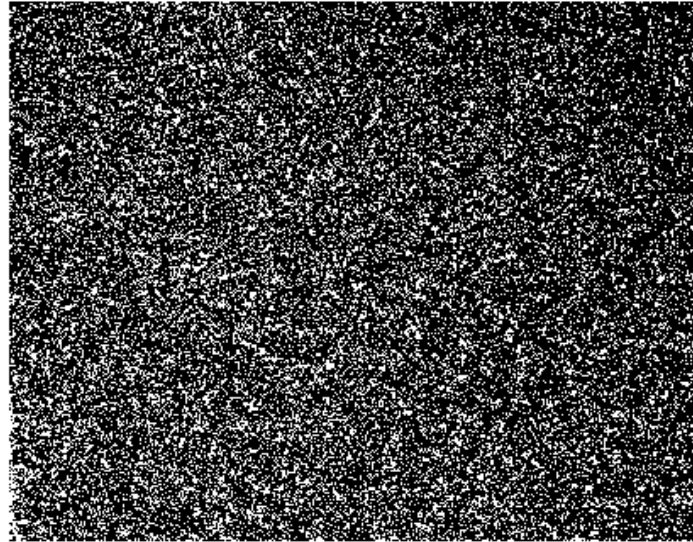
In this set of experiments, the cement paste specimens with the same w/c of 0.45 were tested separately in the environmental chamber with three different air temperatures. Three different air temperatures were selected based on different concrete construction conditions during summer season. The room temperature is the ideal air temperature for concrete construction; the medium temperature is the air temperature when precaution plans should be planned in advance; and the high temperature is intended to simulate the extreme high air temperature encountered in summer. The environmental variables are shown in Table 4.1. The details on the environmental variables and the water evaporation rates for all the cement paste specimens are presented in Appendix B (see Tables B.3 to B.13).

Table 4.1. Average air temperature, relative humidity, and wind velocity during the experiments for the cement paste specimens exposed to three different air temperatures.

Experiment Designation	Air Temperature (°C)	RH (%)	Wind Velocity (m/s)
Room Temperature	23.7	29.0	10.3
Medium Temperature	32.7	21.3	10.1
High Temperature	42.6	11.8	9.8

As the moisture content in the air remains constant, the relative humidity changes as air temperatures change. As shown in Table 4.1, increasing the air temperature in the environmental chamber decreased the relative humidity. As discussed in section 4.2, the specimen can be heated by the hot air during the experiment. According to the water evaporation equation (Equation 2), a rise in air temperature lowers the water evaporation rate of concrete; however, the decrease in relative humidity and increase in concrete temperature as a side effect of increasing air temperature minimize the effect of air temperature on the water evaporation rate of concrete. In this section, a combined effect of air temperature, relative humidity, and cement paste temperature on plastic shrinkage cracking is discussed.

As discussed in section 4.3, the spray paint applied onto the specimen surface may decrease the likelihood of plastic shrinkage cracking. In order to compare the image analysis results between cement paste specimens, the influence of the speckle pattern on the water evaporation rate of the cement paste specimen should be consistent. For each cement paste specimen, the percentage of the speckle pattern coverage at the beginning of the experiment was computed in MATLAB. The level value was selected as 0.70. As shown in Figure 4.15, the white points indicate the speckle pattern, while the black color indicates the cement paste background.



Binary Image (level, 0.70)

Figure 4.15. Binary image of the speckle pattern of the cement paste specimen exposed to the high air temperature at the beginning of the experiment.

The results of the speckle coverages of the cement paste specimens that were exposed to three different air temperatures are presented in Table 4.2. The average speckle coverage and the standard deviation were 25.27% and 1.54%, respectively.

Table 4.2. Speckle coverages of the cement paste specimens exposed to three different air temperatures.

Experiment Designation	Speckle Coverage (%)
Room Temperature	23.82
Medium Temperature	26.89
High Temperature	25.11
Average	25.27
Standard Deviation	1.54

Figure 4.16 shows the crack areas of the cement paste specimens that were exposed to three different air temperatures over time. As shown in Figure 4.16, the crack areas of the cement paste specimens exposed to the room, medium, and high air temperatures began to increase significantly at 62 minutes, 52 minutes, and 37 minutes after starting the experiments, respectively, which were slightly earlier than the time to the first visible crack of 63 minutes, 52 minutes, and 40 minutes. As discussed in sections 3.8.1 and 4.4, this is mainly attributed to some large air pockets that were formed before the first crack.

The crack areas then increased significantly in the following 11 or 12 minutes. Specifically, the crack area of the specimen that was exposed to the room temperature increased from 4.12 mm² to 38.12 mm² in 11 minutes; the crack area of the specimen exposed to the medium air temperature increased from 3.78 mm² to 66.58 mm² in 12 minutes; and the crack area of the specimen exposed to the high air temperature increased from 15.12 mm² to 106.80 mm² in 12 minutes. After the significant increase, the crack area of each specimen almost stabilized until the termination of the experiment.

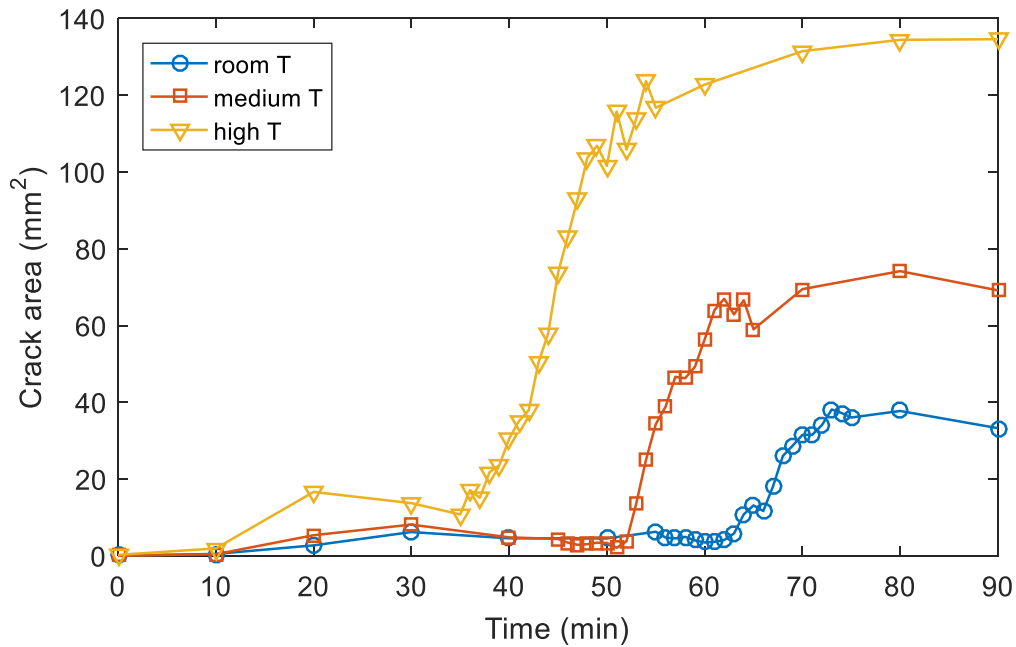


Figure 4.16. Crack areas of the cement paste specimens exposed to three different air temperatures over time.

Based on Figure 4.16, a rise in air temperature decreased the time to first crack, and increased the total crack area on the cement paste surface at the termination of the experiment. Figure 4.17 shows the maximum and minimum strains in the x-direction (e_{xx}) on the cement paste specimens that were exposed to three different air temperatures over time. As mentioned in section 3.8.2, strains were calculated at every data point location within the AOI by VIC-2D; therefore, the maximum and minimum e_{xx} represented the maximum expansion and compression in the x-direction within the data points on the cement paste surface.

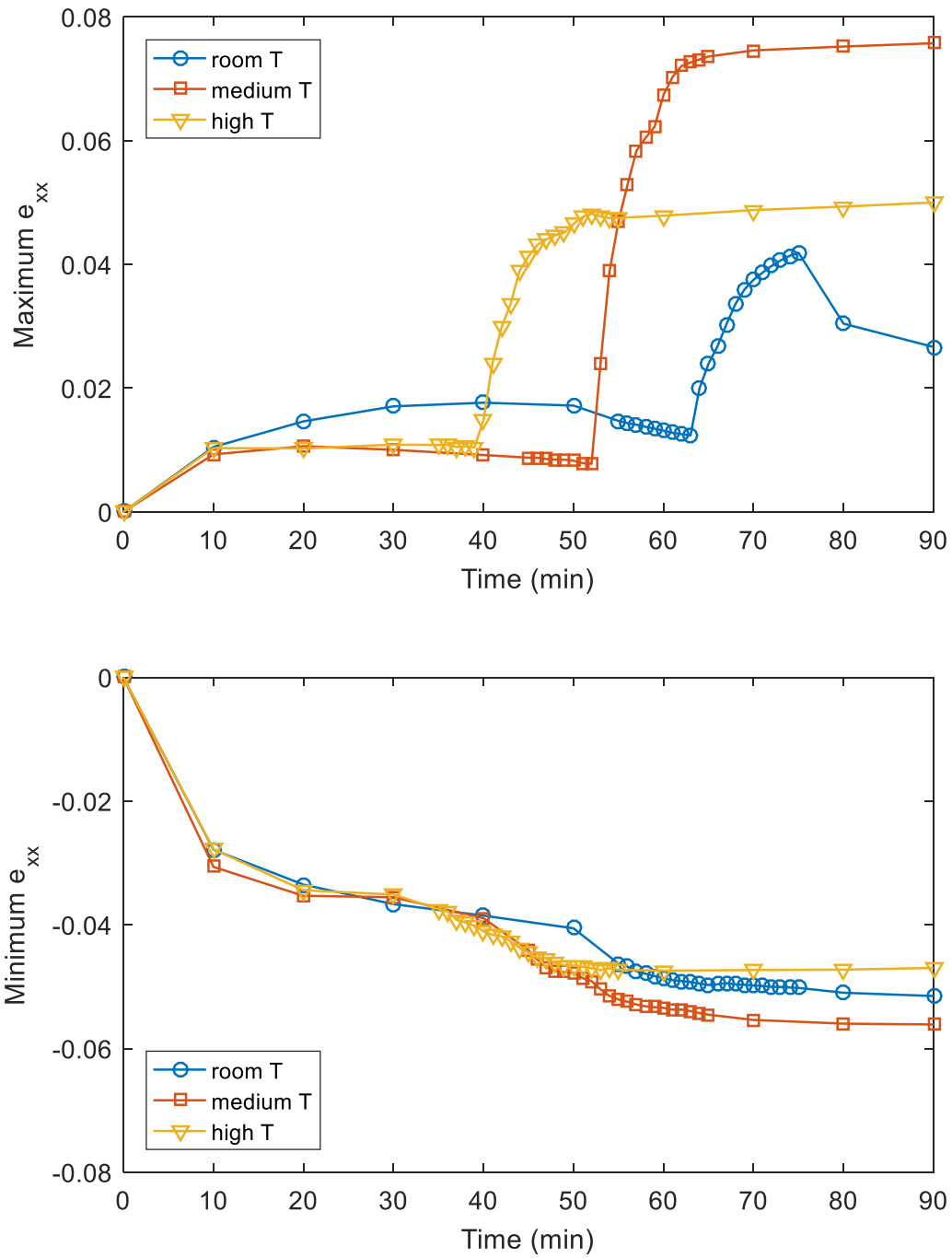


Figure 4.17. Maximum and minimum strains in the x-direction of the cement paste specimens exposed to three different air temperatures over time.

The minimum e_{xx} represents the maximum compressive strain in the x-direction. As shown in Figure 4.17, all the maximum compressive strains in the x-direction on three specimens had a similar significant increase in the first 10 minutes after starting the experiment. After that, all the maximum compressive strains in the x-direction increased slowly. At the termination of the experiments, the maximum compressive strains in the x-direction on the cement paste specimens exposed to the room, medium, and high air temperatures were 5.15%, 5.61%, and 4.70%, respectively.

As the cement paste specimens with the same w/c have the same amount of water content, the maximum contraction capacity (space) between two cement particles caused by surface drying should be the same. As discussed in section 4.2, the temperature of the specimen was not easily affected by the hot air in the beginning of the experiment, and the water evaporation equation was only valid during this period. The water evaporation rates calculated by the water evaporation equation (Equation 2) of the cement paste specimens exposed to the room, medium, and high air temperatures at time zero were 1.72 kg/m²/h, 1.60 kg/m²/h, and 1.89 kg/m²/h, respectively. In addition, as discussed in section 4.4, the compressive strains in the x-direction first accumulated in the area near the edges. The reason that a similar significant increase of the maximum compressive strains in the x-direction (minimum e_{xx}) could be that the water evaporation rates of three cement paste specimens were relatively high and similar in the first 10 minutes after starting the experiments, thus resulting in a similar large contraction between the cement particles in the area near the edges.

However, when air temperature began to affect cement paste temperature, a higher water evaporation rate was expected in the cement paste specimen with a higher temperature, which

increased the total amount of the compressive strains in the x-direction on the cement paste surface, thus increasing the crack area, as shown in Figure 4.18.

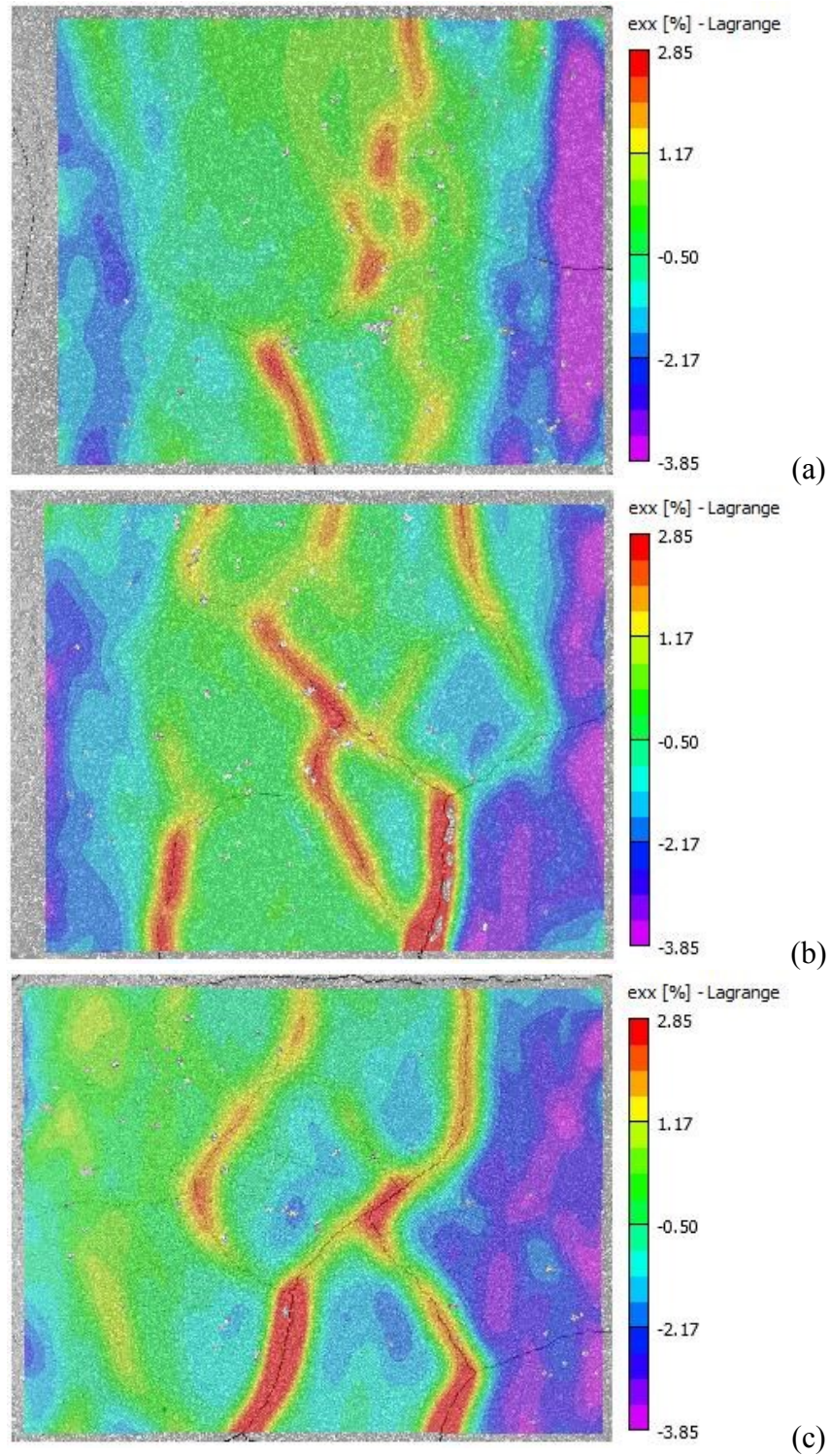


Figure 4.18. Contour maps of e_{xx} of the cement paste specimens exposed to (a) room temperature, (b) medium air temperature, and (c) high air temperature at the termination of the experiments.

The maximum e_{xx} represents the maximum tensile strain in the x-direction. As shown in Figure 4.17, the maximum tensile strains in the x-direction on the cement paste specimens that were exposed to the room, medium, and high air temperatures had a significant increase at 63 minutes, 52 minutes, and 41 minutes after starting the experiments, respectively, which corresponded to the time to first crack. At the termination of the experiments, the maximum tensile strains in the x-direction on the cement paste specimens that were exposed to the room, medium, and high air temperatures were 2.67%, 7.58%, and 5.00%, respectively.

When air temperature began to affect cement paste temperature, a higher water evaporation rate was expected in the cement paste specimen with a higher temperature. The surface of the cement paste specimen that was exposed to the higher air temperature first dried out, which resulted in earlier first crack. However, a rise in cement paste temperature also increased the rate of cement hydration, thus increasing the tensile strength of cement paste to resist deformation, so the maximum tensile and compressive strains in the x-direction on the cement paste specimen that was exposed to the high air temperature were lower than those of the specimen that was exposed to the medium air temperature. Even though the cement paste specimen exposed to the medium air temperature had the highest maximum tensile and compressive strains in the x-direction, the overall shrinkage was less than that of the specimen exposed to the high air temperature, thus having a smaller crack area.

4.6 Effect of wind velocity on plastic shrinkage cracking

The effect of wind velocity on plastic shrinkage cracking is studied in this section. Three cement paste specimens with the same w/c of 0.45 were tested in the environmental chamber only varying the wind velocity. Air temperature and relative humidity varied slightly between experiments. The

average air temperature, relative humidity, and wind velocity during the experiments are shown in Table 4.3.

Table 4.3. Average air temperature, relative humidity, and wind velocity during the experiments for the cement paste specimens exposed to three different wind velocities.

Experiment Designation	Air Temperature (°C)	RH (%)	Wind Velocity (m/s)
Low Wind	39.7	13.1	4.8
Medium Wind	41.1	11.8	7.6
High Wind	42.6	11.8	9.8

The results of the speckle coverages of the cement paste specimens that were exposed to three different wind velocities are presented in Table 4.4. The average speckle coverage and the standard deviation were 25.27% and 1.44%, respectively.

Table 4.4. Speckle coverages of the cement paste specimens exposed to three different wind velocities.

Experiment Designation	Speckle Coverage (%)
Low Wind	26.78
Medium Wind	23.92
High Wind	25.11
Average	25.27
Standard Deviation	1.44

Figure 4.19 shows the crack areas of the cement paste specimens that were exposed to three different wind velocities over time. The time to first crack of three specimens exposed to the low, medium, and high wind velocities were at 85 minutes, 45 minutes, and 40 minutes after starting the experiments, respectively. As shown in Figure 4.19, the crack areas of the cement paste specimens exposed to the medium and high wind velocities began to increase significantly at 42 minutes and 37 minutes after starting the experiment, respectively, which were slightly earlier than the time to first crack. As discussed in section 4.4, this is mainly attributed to some large air pockets that were formed before the first crack.

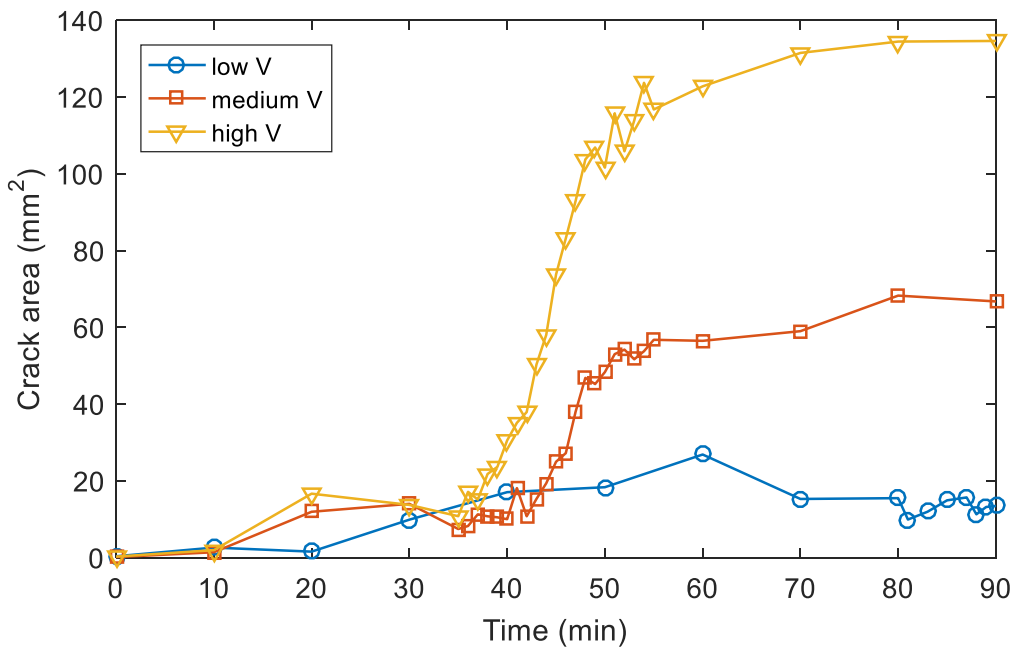


Figure 4.19. Crack areas of the cement paste specimens exposed to three different wind velocities over time.

The crack area of the cement paste specimen that was exposed to the medium wind velocity then increased from 10.77 mm² to 56.74 mm² in 13 minutes, and the crack area of the cement paste

specimen that was exposed to the high wind velocity increased from 15.12mm^2 to 106.80mm^2 in 12 minutes. After the significant increases, the crack areas of the cement paste specimens that were exposed to the medium and high wind velocities almost stabilized until the termination of the experiment.

Unlike the curves of the cement paste specimens that were exposed to the medium and high wind velocities, the crack area of the cement paste specimen exposed to the low wind velocity did not have a significant increase after the time to first crack, and the crack area at the termination of the experiment was only 13.46mm^2 , indicating that the cement paste specimen exposed to the low wind velocity had relatively small and thin visible cracks, as shown in Figure 4.20.



Cleaned Image (low V)

Figure 4.20. Crack contours of the cement paste specimen exposed to the low wind velocity at the termination of the experiment.

Based on Figure 4.19, a drop in wind velocity significantly delayed the time to first crack and decreased the crack area or even prevented the cracking on the cement paste surface at the termination of the experiment.

Figure 4.21 shows the maximum and minimum e_{xx} of the cement paste specimens that were exposed to three different wind velocities. As shown in Figure 4.21, all the maximum compressive strains in the x-direction of three specimens increased significantly in the first 10 minutes after starting the experiment. According to the water evaporation equation (Equation 2), a rise in wind velocity increases the water evaporation rate. The water evaporation rates calculated by the water evaporation equation (Equation 2) of the cement paste specimens that were exposed the low, medium and high wind velocities at time zero were 1.03 kg/m²/h, 1.51 kg/m²/h, and 1.89 kg/m²/h, respectively. Due to the relatively low water evaporation rate of the cement paste specimen that was exposed to the low wind velocity, its maximum compressive strain in the x-direction was the lowest one among the cement paste specimens in the beginning of the experiments. The actual water evaporation rate of the cement paste that was exposed to the low wind velocity may even be lower than the critical 1 kg/m²/h with the influence of the spray paint applied onto its surface, which resulted in small and thin cracks on the cement paste surface.

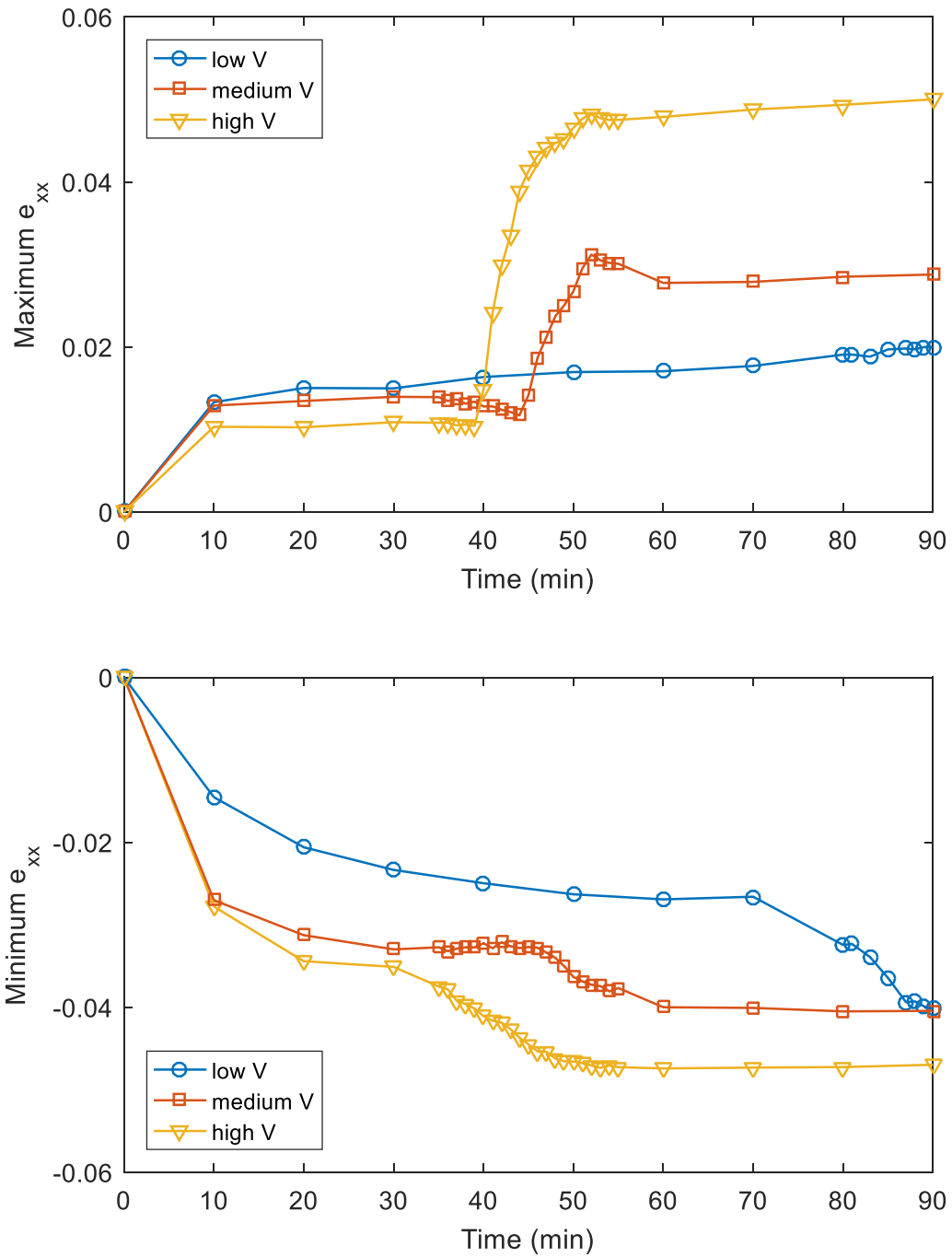


Figure 4.21. Maximum and minimum strains in the x-direction of the cement paste specimens exposed to three wind velocities over time.

As discussed in section 4.5, the cement paste specimens with the same w/c had similar maximum compressive strains on the specimen surface upon drying. At the termination of the experiment, the maximum compressive strains in the x-direction of three specimens that were exposed to the low, medium, and high wind velocities were 4.02%, 4.04%, and 4.70%, respectively. However, a rise in wind velocity increased the total amount of water evaporated from the cement paste specimen, which increased the total amount of compressive strains in the x-direction on the cement paste surface, thus increasing the crack area, as shown in Figure 4.22.

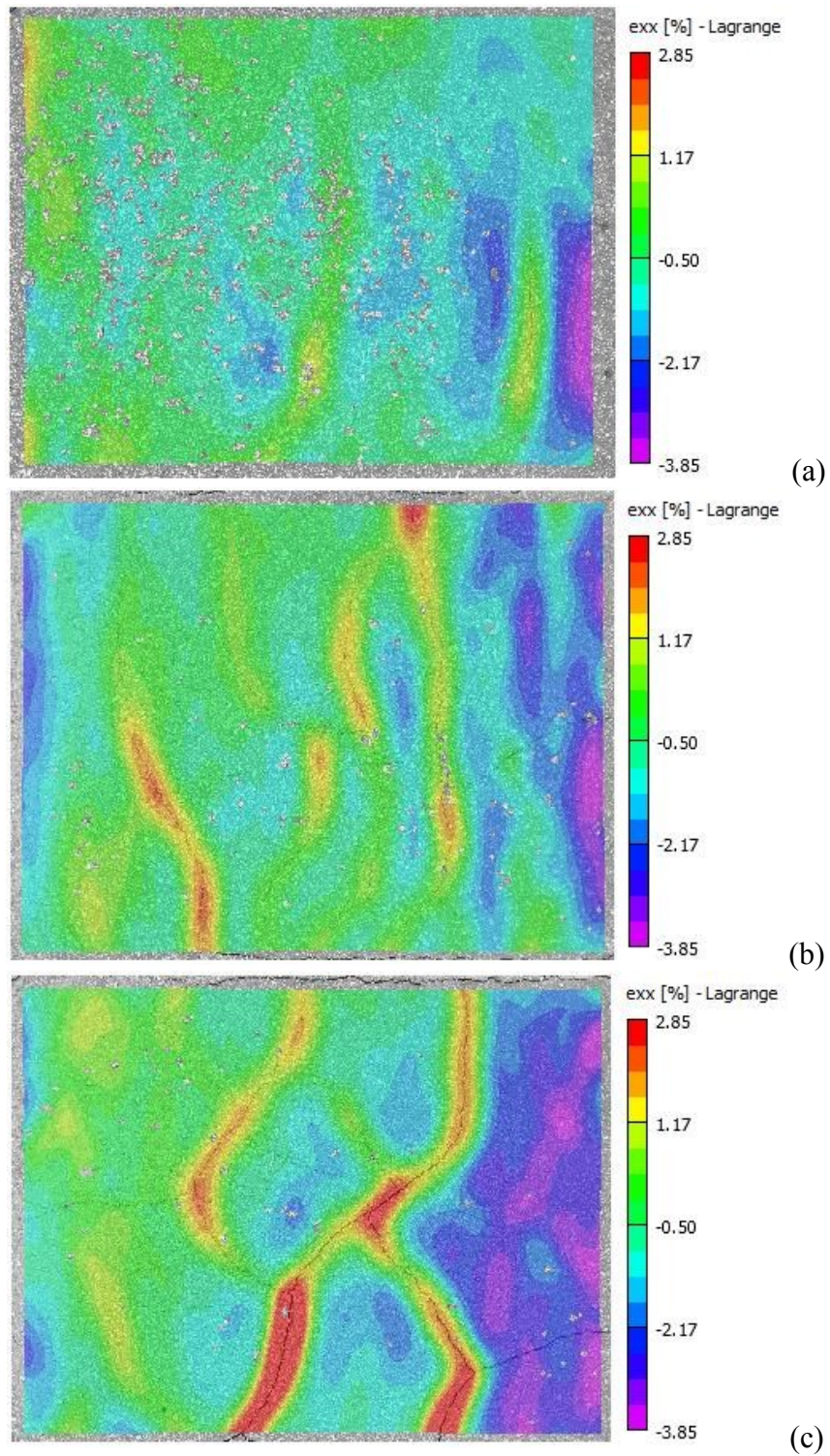


Figure 4.22. Contour maps of e_{xx} of the cement paste specimens exposed to (a) low wind velocity, (b) medium low velocity, and (c) high wind velocity at the termination of the experiments.

The maximum e_{xx} can be used to indicate the cracking formation on the cement paste surface. As shown in Figure 4.21, the maximum e_{xx} on the cement paste specimens that were exposed to the medium and high wind velocities increased significantly at 44 minutes and 39 minutes after starting the experiments, respectively, which corresponded to the time to first crack. The maximum e_{xx} of the cement paste specimen that was exposed to the low wind velocity did not have a significant increase because of the small and thin cracks on the specimen surface.

4.7 Effect of w/c on plastic shrinkage cracking

The cement paste specimens with w/c varying from 0.35 to 0.50 were tested separately in the environmental chamber. The results of the crack areas and DIC analysis are presented and discussed in this section. The average air temperature, relative humidity, and wind velocity during the experiments were 42.9 °C, 14.7%, and 9.4 m/s, respectively. The results of speckle coverages are presented in Table 4.5. The average speckle coverage and the standard deviation were 19.03% and 0.87%, respectively.

Table 4.5. Speckle coverages of the cement paste specimens with different w/c.

Experiment Designation	Speckle Coverage (%)
w/c 0.35	19.16
w/c 0.40	20.20
w/c 0.45	18.20
w/c 0.50	18.56
Average	19.03
Standard Deviation	0.87

Figure 4.23 shows the crack areas of the cement paste specimens with different w/c that were exposed to a uniform drying environment over time. As shown in Figure 4.23, the time to first crack of the cement paste specimens with w/c 0.35, 0.40, 0.45, and 0.50 were at 25 minutes, 28 minutes, 36 minutes, and 40 minutes after starting the experiments, respectively. At the termination of the experiments, the crack areas of the cement paste specimens with w/c 0.35, 0.40, 0.45, and 0.50 were 53.16mm², 86.28mm², 111.8mm², and 145.2 mm², respectively. This is in agreement with the previous research that a rise in w/c delayed the time to first crack and increased the total percentage of crack area (Almusallam et al., 1998).

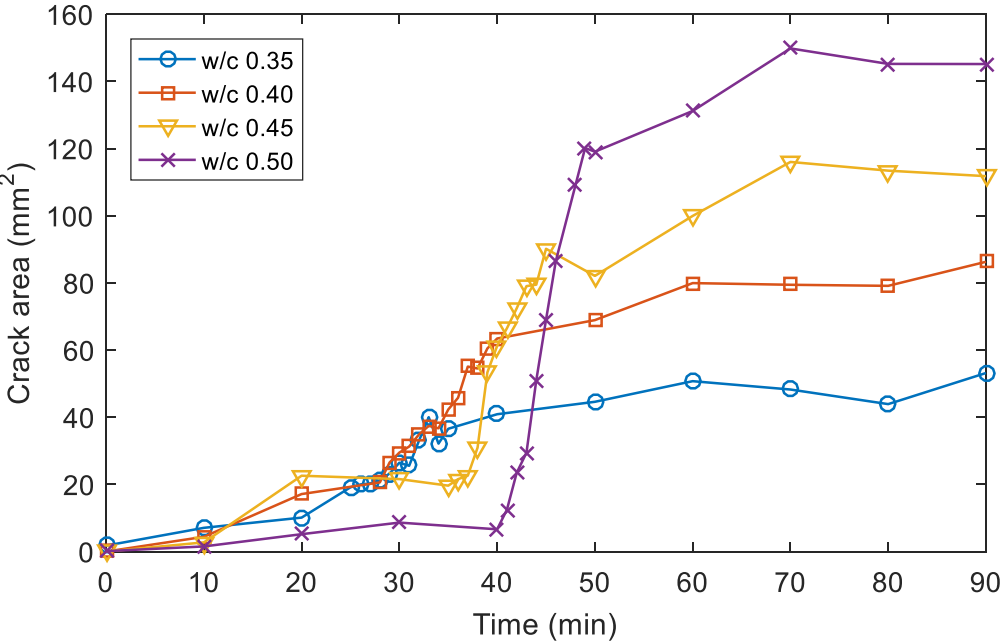


Figure 4.23. Crack areas of the cement paste specimens with different w/c over time.

Figure 4.24 shows the maximum and minimum ϵ_{xx} on the cement paste specimens with different w/c varying from 0.35 to 0.50. As shown in Figure 4.24, the time that the maximum ϵ_{xx} of each specimen began to increase significantly corresponded to the time to first crack. A rise in w/c

increased the maximum tensile and compressive strains in the x-direction on the cement paste surface. At the termination of the experiments, the maximum tensile strains in the x-direction of the cement paste specimens with w/c 0.35, 0.40, 0.45, and 0.50 were 2.70%, 3.15%, 4.68%, and 7.40%, respectively, and the maximum compressive strains in the x-direction were 3.11%, 3.85%, 7.14%, and 7.87%, respectively.

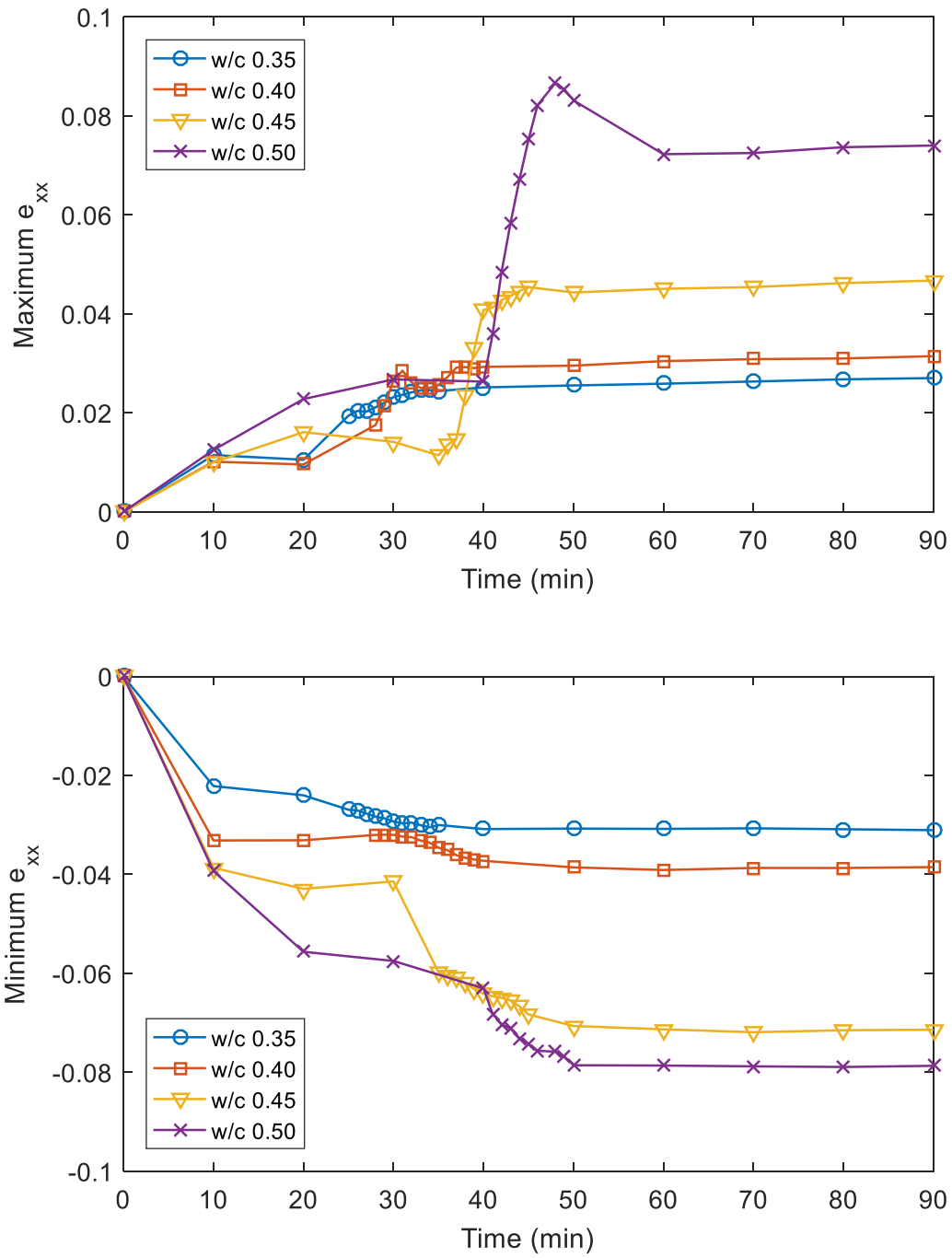


Figure 4.24. Maximum and minimum strains in the x-direction of the cement paste specimens with different w/c over time.

According to the water evaporation equation (Equation 2), the cement paste specimens with different w/c that were exposed to a uniform drying environment had the same water evaporation rate in the beginning of the experiments. However, a rise in w/c increased the maximum contraction capacity (space) between the cement particles, thus increasing the maximum compressive strain on the cement paste surface as drying occurred. It is generally agreed that the bleeding rate of cement paste is determined by cement content, and a rise in w/c increased the bleeding rate. Thus, the surface of the cement paste specimen with lower w/c first dried out, which resulted in earlier first crack. Even though the cement paste specimen with lower w/c cracked earlier, the total amount of water evaporated from the specimen was less than that of the cement paste specimen with higher w/c. In addition, the cement paste specimen with lower w/c had higher tensile strength to resist deformation, which resulted in a smaller crack area on the cement paste surface.

4.8 Effect of substrate roughness on plastic shrinkage cracking

In this set of experiments, the cement paste specimens with the same w/c of 0.45 were cast on three substrate conditions with different roughness, namely without sandpaper, No. 180 sandpaper (fine), and No. 40 sandpaper (coarse). The average diameters of No. 180 and No. 40 sandpaper grit particles are 82 μm and 425 μm , respectively. The cement paste specimens were then tested in a uniform drying environment for 90 minutes. The average air temperature, relative humidity, and wind velocity during the experiments were 42.0 °C, 11.2%, and 9.8 m/s, respectively. The results of speckle coverages are presented in Table 4.6. The average speckle coverage and the standard deviation were 22.41% and 2.43%, respectively.

Table 4.6. Speckle coverages of the cement paste specimens cast on three different substrate conditions.

Experiment Designation	Speckle Coverage (%)
Without Sandpaper	21.72
No. 40 Sandpaper	20.40
No. 180 Sandpaper	25.11
Average	22.41
Standard Deviation	2.43

Figure 4.25 shows the crack areas of the cement paste specimens cast on three different substrate conditions over time. As shown in Figure 4.25, the time to first crack of the cement paste specimens that were cast on duct tape (without sandpaper), No. 180, and No. 40 sandpapers were at 38 minutes, 40 minutes, and 38 minutes, respectively. The crack areas of the cement paste specimens at the termination of the experiments were 105.7 mm², 135.6 mm², and 107.6 mm², respectively.

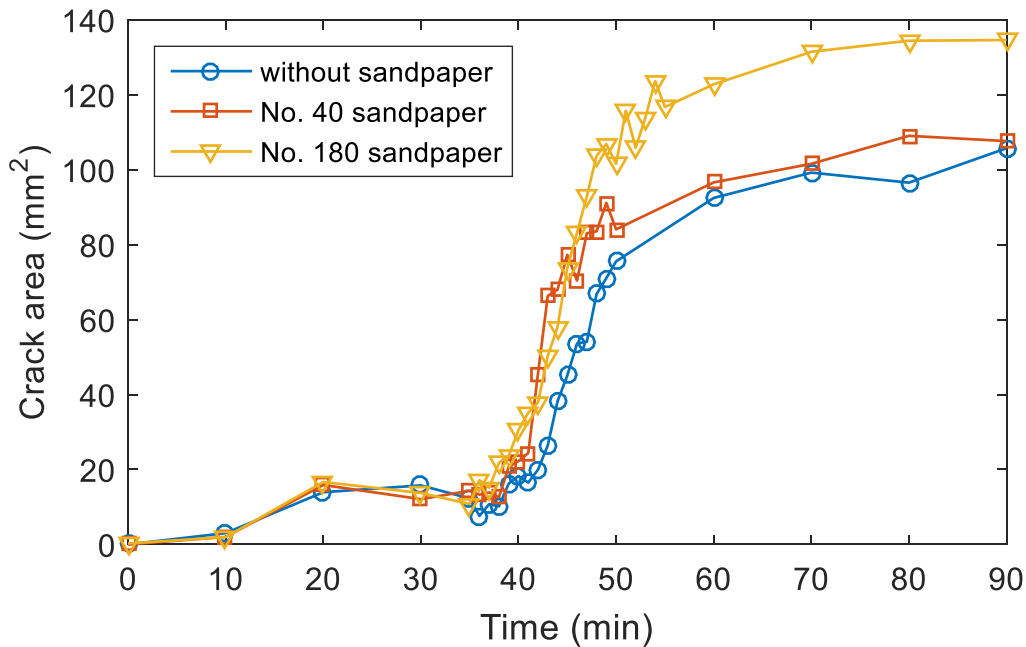


Figure 4.25. Crack areas of the cement paste specimens cast on three different substrate conditions over time.

Theoretically, the cement paste specimens with the same w/c that were exposed to a uniform drying environment had the same water evaporation rate and same amount of water evaporated from the cement paste specimens. According to Slowik et al. (2008), the risk of plastic shrinkage cracking reaches its maximum when air starts to penetrate the gaps between the solid particles. Thus, different substrate roughness did not affect the time to first crack.

As discussed in section 4.4, the cement paste specimen began to shrink from the edges upon drying. A shrinkage difference then existed between the surface and the bottom of the cement paste specimen, which resulted in strain localization and cracking. For the cement paste cast on the duct tape (without sandpaper), the shrinkage difference was only caused by the different evaporation rates between the surface and the bottom of the cement paste specimen. The fine sandpaper that

restrained the shrinkage at the bottom increased the shrinkage difference, thus increasing the crack area. However, the coarse sandpaper provided more restraint higher into the specimen depth, which decreased the shrinkage difference, thus decreasing the crack area.

Figure 4.26 shows the maximum and minimum e_{xx} on the cement paste specimens cast on three different substrate conditions. As shown in Figure 4.26, at the termination of the experiments, the cement paste specimen that was cast on No. 40 sandpaper had the smallest maximum tensile and compressive strains on the cement paste surface, which were 2.87% and 3.41%, respectively. The cement paste specimen that was cast on No. 180 sandpaper had the largest maximum tensile and compressive strains on the cement paste surface, which were 5.00% and 4.70%, respectively. As discussed earlier, the cement paste specimen that was cast on No. 180 sandpaper had a higher shrinkage difference, which resulted in larger maximum tensile and compressive strains as well as a larger crack area. The cement paste specimen that was cast on No. 40 sandpaper had a lower shrinkage difference, which resulted in smaller maximum tensile and compressive strains as well as a smaller crack area.

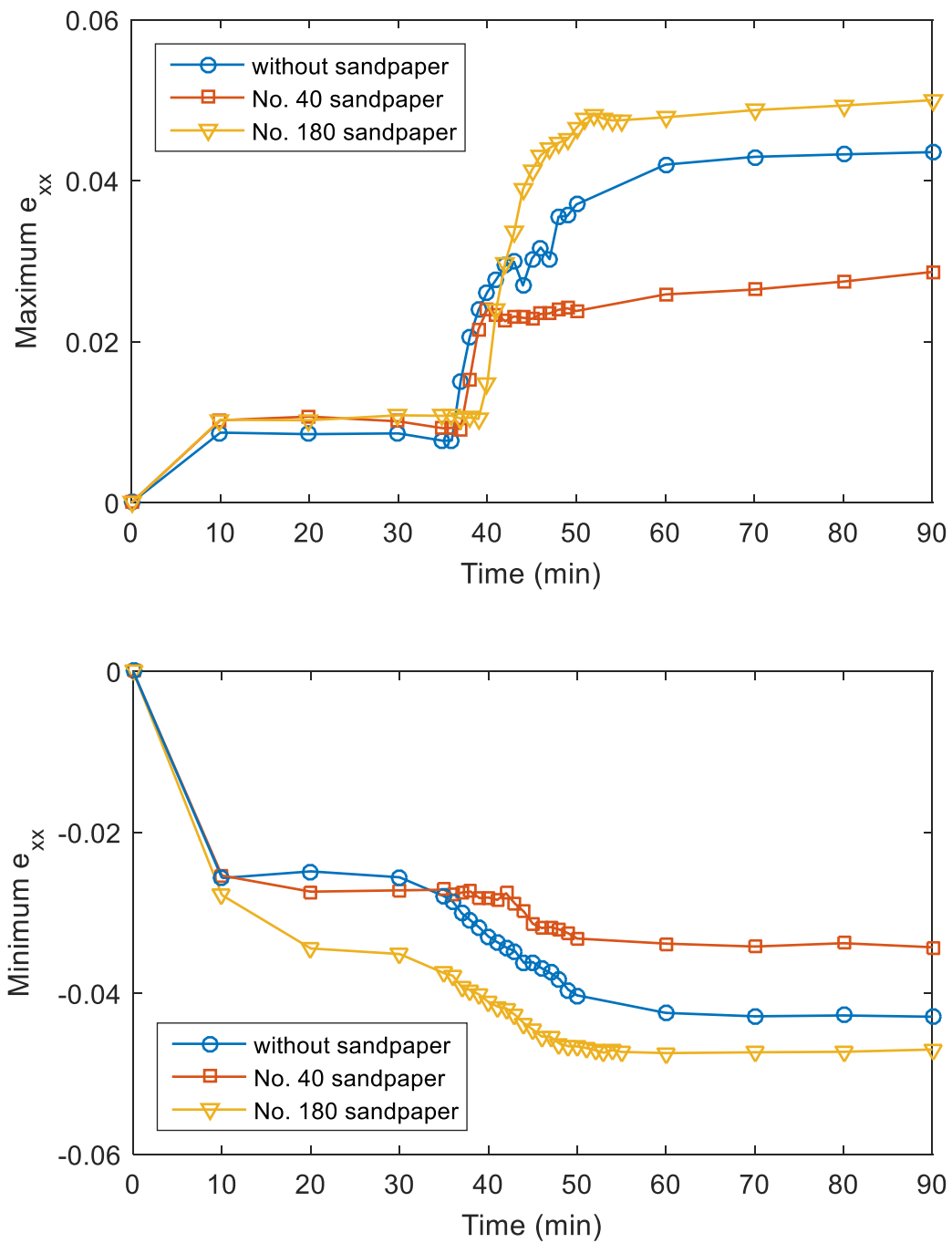


Figure 4.26. Maximum and minimum strains in the x-direction of the cement paste specimens cast on three different substrate conditions over time.

4.9 Evaluation of ASTM Standard C1579 geometry

In order to analyze the reasons that no cracking occurred in the concrete specimens prepared conforming to ASTM Standard C 1579, a set of image analysis results by VIC-2D is presented and discussed in this section. A series of contour maps of strains in the x-direction is presented in Figures 4.27 to 4.30.

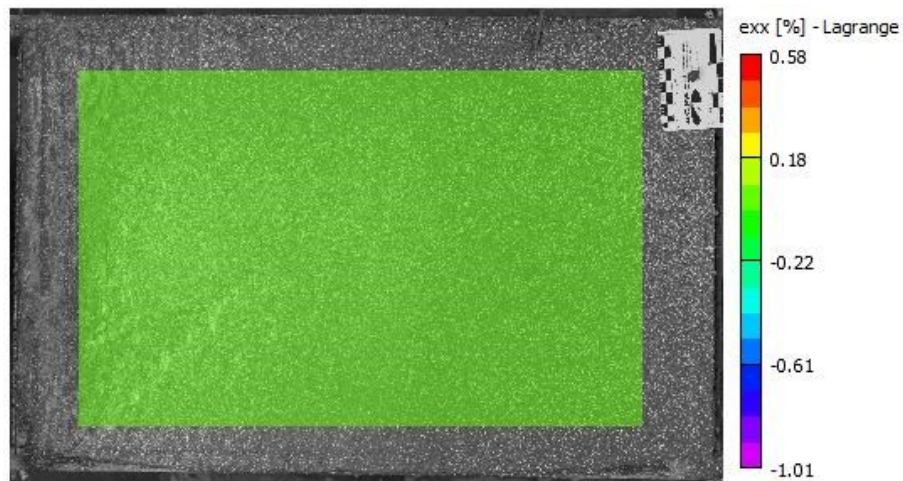


Figure 4.27. Contour map of e_{xx} on the concrete surface at the beginning of the experiment.

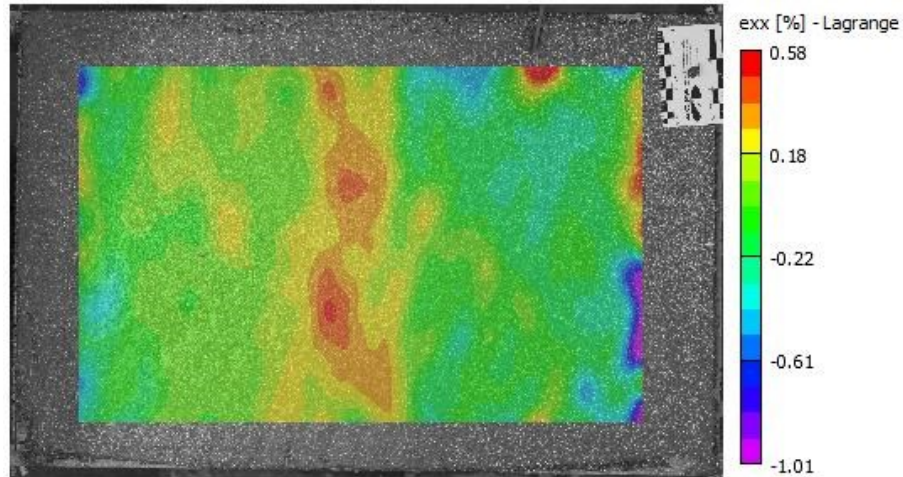


Figure 4.28. Contour map of e_{xx} on the concrete surface at 30 minutes after starting the experiment.

As shown in Figure 4.27, at the beginning of the experiment, no strain in the x-direction occurred. At 30 minutes after starting the experiment, some tensile strains in the x-direction accumulated in the middle of the concrete specimen (above center riser), as shown in Figure 4.28.

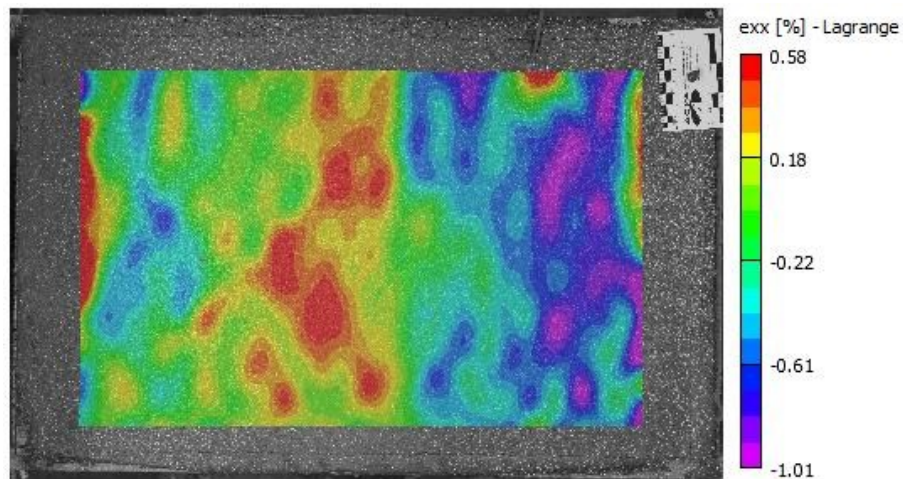


Figure 4.29. Contour map of e_{xx} on the concrete surface at 90 minutes after starting the experiment.

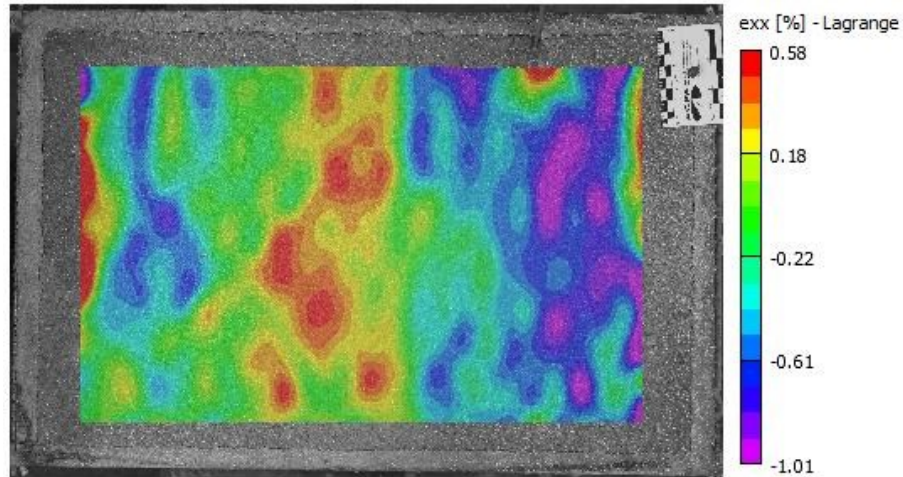


Figure 4.30. Contour map of e_{xx} on the concrete surface at 360 minutes after starting the experiment.

According to ASTM Standard C1579, a stress riser, with the height of 63.5% of the form depth, was placed in the center of the concrete form. The center riser was high enough to be considered as an edge, and effectively divided the whole concrete specimen into two parts. As discussed in section 4.4, the cement paste began to shrink from the edges upon drying, and the compressive strains in the x-direction accumulated in the area near the both shorter sides of the specimen. As to the concrete specimen, each part of the specimen began to shrink from edges after starting the experiment. However, the two parts of the concrete specimen were still connected by the concrete above the center riser, thus developing the tensile strains in this area. This can also explain some tensile strains that accumulated in the area near the two shorter sides of the form, as shown in Figures 4.29 and 4.30. When the concrete specimen was screeded by a straightedge, there was some cement paste left on the four sides of the form, which connected the concrete specimen and the sides of the form.

As shown in Figure 4.30, more compressive strains in the x-direction accumulated in the right part of the specimen at the termination of the experiment due to the fan heaters that were placed to the left of the concrete specimen, which increased the concrete temperature in the left part of the specimen to resist deformation.

According to DIC analysis results, the maximum tensile and compressive strains in the x-direction on the concrete surface were 1.69% and 1.79%, respectively, as shown in Figure 4.31. Even though the tensile strains had accumulated in the middle of the concrete specimen, the maximum tensile and compressive strains in the x-direction on the concrete specimen at the termination of the experiment were much lower compared with the maximum tensile and compressive strains in the x-direction on all cement paste specimens.

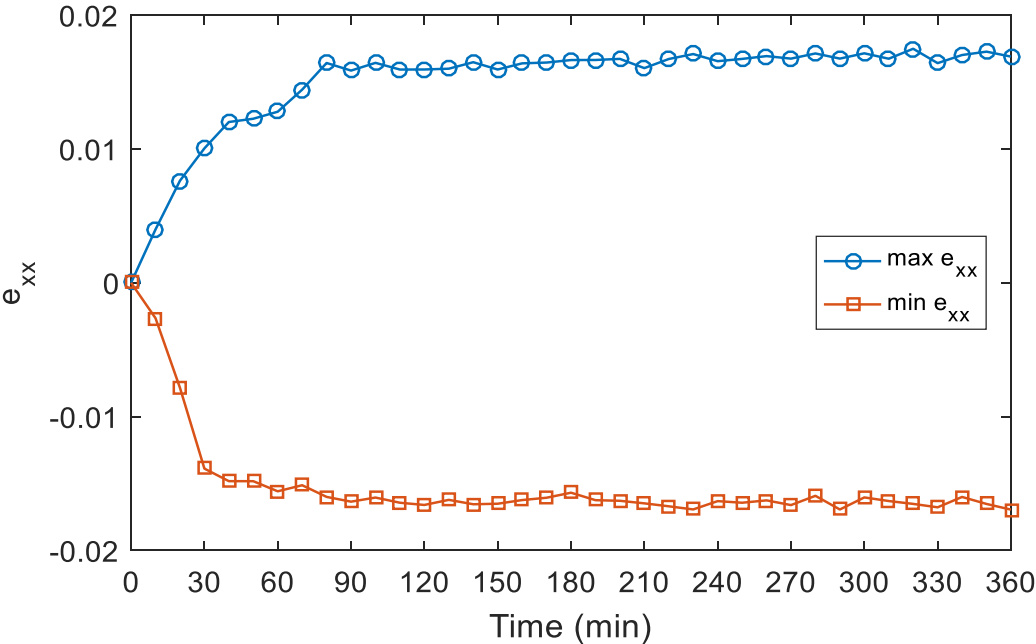


Figure 4.31. Maximum and minimum strains in the x-direction of the concrete specimen over time.

The reason that no cracking occurred on the concrete specimen could be the electrical fan that was used in this experiment. As discussed in section 4.6, a drop in wind velocity significantly delayed the time to first crack and decreased the total crack area. Due to the size of the concrete specimen (560×355×100 mm), the wind generated by the electrical fan cannot fully cover the whole surface area of the concrete specimen. In addition, as discussed in section 4.3, the spray paint applied onto the concrete surface lowered the water evaporation rate and delayed the water evaporation, which could also reduce the likelihood of plastic shrinkage cracking in this experiment.

5 CONCLUSIONS AND FUTURE WORK

5.1 Conclusions

This project applied the DIC technique to evaluate the behavior of plastic shrinkage cracking in cement-based materials. DIC is based on tracking speckle patterns before and after a deformation. In this project, a white spray paint was selected to apply the speckle pattern. As plastic shrinkage cracking is highly dependent on the rapid surface drying, the effect of the spray paint on the water evaporation rate of concrete was first evaluated, and the water evaporation rates calculated by mass loss and the water evaporation equation (Equation 2) were compared. Based on the literature review, plastic shrinkage cracking is influenced by concrete proportions and ingredients as well as its external environment and restraint conditions. Thus, air temperature, wind velocity, w/c, and substrate roughness were chosen as independent variables. Their effects on plastic shrinkage cracking were evaluated by crack areas computed in MATLAB and DIC analysis results. Finally, the geometry in ASTM Standard C1579 was assessed by DIC analysis results. The conclusions are summarized in the following paragraphs:

1. The results calculated by the water evaporation equation (Equation 2) were only valid in stage I drying. The inaccurate results in stage II drying were mainly caused by a rise in concrete temperature that was increased by the hot air in the environmental chamber.
2. The spray paint lowered the water evaporation rate, which may reduce the likelihood of plastic shrinkage cracking. For all the cement paste specimens, the speckle coverage was approximately 25%. However, the standard deviations are low, indicating relative changes due to the variable measured (air temperature, wind velocity, w/c, and substrate roughness) are valid.

3. DIC can provide a series of strain maps that helped to understand the cracking process. The accumulations of tensile and compressive strains can be used to illustrate the cracking intensity and the overall shrinkage, respectively. The evolutions of the maximum tensile and compressive strains can be used to indicate the time to first crack and the shrinkage capacity, respectively. As DIC cannot measure the crack dimensions, the crack area was determined based on the same images using MATLAB functions. The significant increase in crack area corresponded to the developments of several peak strains observed in DIC.
4. The process of plastic shrinkage cracking in the cement paste specimen is well understood by DIC analysis results. First, the cement paste specimen began to shrink from the edges after starting the experiments. Due to the shrinkage difference between the surface and the bottom of the cement paste, a strain localization took place, which resulted in the first crack. After that, the crack became wider and deeper, thus dividing the cement paste specimen into two independent parts. Each new part then repeated the process of the first crack.
5. In this project, due to a drop in relative humidity as a result of increasing air temperature, air temperature had a limited effect on the water evaporation rate in the beginning of the experiments. However, when air temperature began to affect cement paste temperature, the cement paste specimen that was exposed to the air with a higher temperature had a higher water evaporation rate, thus decreasing the time to first crack and increasing the total crack area. Air temperature also affected the rate of cement hydration. The cement paste specimen that was exposed to the air with a higher temperature developed higher tensile strength to resist cracking.

6. Wind velocity is essential to the formation of plastic shrinkage cracking. A drop in wind velocity significantly delayed the time to first crack and decreased the crack area on the cement paste.
7. A rise in w/c increased the water content and shrinkage capacity of the cement paste specimen, thus causing a delay in the time to first crack and a larger crack area, respectively.
8. The crack area is dependent on the shrinkage difference between the surface and the bottom of the specimen. The fine sandpaper restrained the shrinkage at the bottom increased the shrinkage difference, thus increasing the crack area; however, the coarse sandpaper provided more restraint higher into the specimen depth, which decreased the shrinkage difference, thus decreasing the crack area. The substrate roughness had a limited effect on the time to first crack.
9. In ASTM Standard C1579, plastic shrinkage cracking is expected to occur above the center riser. According to DIC analysis results, the center riser in the form worked as an edge which divided the concrete surface into two parts. Each part began to shrink from the edges upon drying. However, the two parts were still connected to each other; therefore, the tensile strains accumulated in this area.

5.2 Suggestions for future work

1. In the form that was adopted from Wang et al. (2001), plastic shrinkage cracking occurred in an irregular random pattern. According to section 4.9, cracking can be induced at predetermined locations by placing dividers in the form with the height less than the form depth.

2. When evaluating the effect of air temperature on plastic shrinkage cracking, a drop in relative humidity as a side effect of increasing air temperature minimized the effect of air temperature on the water evaporation rate; therefore, a humidity controlled environmental chamber should be used to eliminate the effect of the extraneous variable.
3. Due to the size of the form that was adopted from Wang et al. (2001), plastic shrinkage cracking was only evaluated in the cement paste specimens in this project. However, concrete materials are more complicated than cement paste. Further investigation should be conducted on plastic shrinkage cracking in mortar or concrete specimens.
4. According to Qi et al. (2005), the crack area obtained from image analysis were less than the actual crack area. Thus, a correction factor can be established between the results obtained from image analysis measurement and optical measurement in the future work.
5. Plastic settlement can be considered as out-of-plane motion, which may cause the false correlation in 2D-DIC system. A 3D-DIC system is suggested to solve this problem. In addition, plastic settlement and plastic shrinkage can be evaluated at the same time in 3D-DIC system.
6. When evaluating the effect of substrate roughness on plastic shrinkage cracking, crack areas were mainly determined by the shrinkage difference between the surface and the bottom of the cement paste specimen; therefore, further investigation should be conducted to evaluate the effect of the sample depth on plastic shrinkage cracking.
7. Research should be performed to evaluate the risk of plastic shrinkage cracking in concrete materials containing supplementary cementitious materials using image analysis methods.

8. In this project, the spray paint that was applied on the concrete surface reduced and delayed the water evaporation, which may reduce the likelihood of plastic shrinkage cracking. The effects of different types of spray paint on the water evaporation rates of concrete should be studied.

9. According to Slowik et al. (2008), the risk of plastic shrinkage cracking reaches its maximum when air starts to penetrate the gaps between the solid particles. When surface water is dried out, concrete temperature can be easily affected by its external environment. Thus, a relationship can be established between plastic shrinkage cracking and concrete temperature in the future work.

6 REFERENCES

ACI 305R-10. (2010). Guide for hot weather concreting. *American Concrete Institute*, Farmington Hills, MI.

Alam, S., Loukili, A., & Grondin, F. (2012). Monitoring size effect on crack opening in concrete by digital image correlation. *European Journal of Environmental and Civil Engineering*, 16(7), 818-836.

Aldalinsi, M., Ferregut, C., Carrasco, C., Tandon, V., & Alderette, M. (2014). A method to reduce plastic shrinkage cracking of concrete using the re-vibration technique. *Structures Congress 2014*, Boston, MA, April, 1942-1954.

Almusallam, A., Maslehuddin, M., Abdul-Waris, M., & Khan, M. (1998). Effect of mix proportions on plastic shrinkage cracking of concrete in hot environments. *Construction and Building Materials*, 12(6), 353-358.

ASTM Standard C127-15. (2015). Standard Test Method for Density, Relative Density (Specific Gravity), and Absorption of Coarse Aggregate. *ASTM International*, West Conshohocken, PA, DOI: 10.1520/C0127-15, www.astm.org.

ASTM Standard C128-15. (2015). Standard Test Method for Density, Relative Density (Specific Gravity), and Absorption of Fine Aggregate. *ASTM International*, West Conshohocken, PA, DOI: 10.1520/C0128-15, www.astm.org.

ASTM Standard C136/C136M-14. (2014). Standard Test Method for Sieve Analysis of Fine and Coarse Aggregates. *ASTM International*, West Conshohocken, PA, DOI: 10.1520/C0136_C0136M-14, www.astm.org.

ASTM Standard C143/C143M-12. (2012). Standard Test Method for Slump of Hydraulic-Cement Concrete. *ASTM International*, West Conshohocken, PA, DOI: 10.1520/C0143_C0143M-12, www.astm.org.

ASTM Standard C1579-13. (2013). Standard Test Method for Evaluating Plastic Shrinkage Cracking of Restrained Fiber Reinforced Concrete (Using a Steel Form Insert). *ASTM International*, West Conshohocken, PA, DOI: 10.1520/C1579-13, www.astm.org.

ASTM Standard C192/C192M-14. (2014). Standard Practice for Making and Curing Concrete Test Specimens in the Laboratory. *ASTM International*, West Conshohocken, PA, DOI: 10.1520/C0192_C0192M-14, www.astm.org.

ASTM Standard C29/C29M-09. (2009). Standard Test Method for Bulk Density ("Unit Weight") and Voids in Aggregate. *ASTM International*, West Conshohocken, PA, DOI: 10.1520/C0029_C0029M-09, www.astm.org.

ASTM Standard C305-14. (2014). Standard Practice for Mechanical Mixing of Hydraulic Cement Pastes and Mortars of Plastic Consistency. *ASTM International*, West Conshohocken, PA, DOI: 10.1520/C0305-14, www.astm.org.

ASTM Standard C33/C33M-13. (2013). Standard Specification for Concrete Aggregates. *ASTM International*, West Conshohocken, PA, DOI: 10.1520/C0033_C0033M-13, www.astm.org.

- Bakhshi, M., & Mobasher, B. (2011). Experimental observations of early-age drying of Portland cement paste under low-pressure conditions. *Cement and Concrete Composites*, 33(4), 474-484.
- Balaguru, P. (1994). Contribution of fibers to crack reduction of cement composites during the initial and final setting period. *ACI Materials Journal*, 91(3), 280-288.
- Banthia, N., Azzabi, M., & Pigeon, M. (1995). Restrained shrinkage tests on fiber reinforced cementitious composites. *ACI Special Publication, SP 155: Testing of Fiber Reinforced Concrete*. Editors: David J Stevens, Nemy Banthia, Vellore S. Gopalaratnam, and Peter C. Tatnall; SP 155-7, 137-151.
- Banthia, N., & Gupta, R. (2007). Test method for evaluation of plastic shrinkage cracking in fiber-reinforced cementitious materials. *Experimental Techniques*, 31(6), 44-48.
- Banthia, N., & Gupta, R. (2009). Plastic shrinkage cracking in cementitious repairs and overlays. *Materials and Structures*, 42(5), 567-579.
- Banthia, N., Yan, C., & Mindess, S. (1996). Restrained shrinkage cracking in fiber reinforced concrete: A novel test technique. *Cement and Concrete Research*, 26(1), 9-14.
- Banthia, N., & Gupta, R. (2006). Influence of polypropylene fiber geometry on plastic shrinkage cracking in concrete. *Cement and Concrete Research*, 36(7), 1263-1267.
- Barazzetti, L., & Scaioni, M. (2009). Crack measurement: Development, testing and applications of an automatic image-based algorithm. *ISPRS Journal of Photogrammetry and Remote Sensing*, 64(3), 285-296.

Bentur, A., & Kovler, K. (2003). Evaluation of early age cracking characteristics in cementitious systems. *Materials and Structures*, 36(3), 183-190.

Bentz, D. P. (2008). A review of early-age properties of cement-based materials. *Cement and Concrete Research*, 38(2), 196-204.

Berke, N., & Dallaire, M. (1994). Effect of low addition rates of polypropylene fibers on plastic shrinkage cracking and mechanical properties of concrete. *ACI Special Publication, SP 142: Fiber Reinforced Concrete Developments and Innovations*. Editors, James I. Daniel and Surendra P. Shah; SP 142-02, 19-41.

Bjøntegaard, Ø, Hammer, T., & Sellevold, E. (1998). Cracking in high performance concrete before setting. *International Symposium on High Performance and Reactive Powder Concrete*, Sherbrooke, QC, August, 332-348.

Boulekbache, B., Hamrat, M., Chemrouk, M., & Amziane, S. (2015). Failure mechanism of fibre reinforced concrete under splitting test using digital image correlation. *Materials and Structures*, 48(8), 2713-2726.

Canadian Climate Normals 1981-2010 Station Data. (2015). Retrieved from http://climate.weather.gc.ca/climate_normals/results_1981_2010_e.html?stnID=5415&autofwd=1

Choi, S., & Shah, S. (1997). Measurement of deformations on concrete subjected to compression using image correlation. *Experimental Mechanics*, 37(3), 307-313.

Corr, D., Accardi, M., Graham-Brady, L., & Shah, S. (2007). Digital image correlation analysis of interfacial debonding properties and fracture behavior in concrete. *Engineering Fracture Mechanics*, 74(1), 109-121.

Correlated Solutions, Inc. (2009). VIC-2D Reference Manual.

Gao, P., Zhang, T., Luo, R., Wei, J., & Yu, Q. (2014). Improvement of autogenous shrinkage measurement for cement paste at very early age: Corrugated tube method using non-contact sensors. *Construction and Building Materials*, 55, 57-62.

Gencturk, B., Hossain, K., Kapadia, A., Labib, E., & Mo, Y. (2014). Use of digital image correlation technique in full-scale testing of prestressed concrete structures. *Measurement*, 47, 505-515.

Kosmatka, S. H., Panarese, W. C., & Portland Cement Association. (2002). Design and control of concrete mixtures. 7th Canadian edition, Ottawa, ON.

Kraai, P. P. (1985). A proposed test to determine the cracking risk potential to drying shrinkage of concrete. *Concrete Construction*, 30(9), 775-778.

Leemann, A., Nygaard, P., & Lura, P. (2014). Impact of admixtures on the plastic shrinkage cracking of self-compacting concrete. *Cement and Concrete Composites*, 46, 1-7.

Mauroux, T., Benboudjema, F., Turcry, P., Ait-Mokhtar, A., & Deves, O. (2012). Study of cracking due to drying in coating mortars by digital image correlation. *Cement and Concrete Research*, 42(7), 1014-1023.

Mehta, P. K., & Monteiro, P. J. (2006). *Concrete: Microstructure, properties, and materials*. 3rd edition, McGraw-Hill, New York.

Mindess, S., & Diamond, S. (1980). A preliminary SEM study of crack propagation in mortar. *Cement and Concrete Research*, 10(4), 509-519.

Mora, J., Gettu, R., Olazabal, C., Martin, M. A., & Aguado, A. (2000). Effect of the incorporation of fibers on the plastic shrinkage of concrete. *RILEM Symposium on Fibre-Reinforced Concretes*, Lyon, France, September, 705-714.

Mora-Ruacho, J., Gettu, R., & Aguado, A. (2009). Influence of shrinkage-reducing admixtures on the reduction of plastic shrinkage cracking in concrete. *Cement and Concrete Research*, 39(3), 141-146.

Naaman, A. E., Wongtanakitcharoen, T., & Hauser, G. (2005). Influence of different fibers on plastic shrinkage cracking of concrete. *ACI Materials Journal*, 102(1), 49-58.

Ong, K. G., & Myint-Lay, K. (2006). Application of image analysis to monitor very early age shrinkage. *ACI Materials Journal*, 103(3), 169-176.

Qi, C., Weiss, J., & Olek, J. (2003). Characterization of plastic shrinkage cracking in fiber reinforced concrete using image analysis and a modified weibull function. *Materials and Structures*, 36(6), 386-395.

Qi, C., Weiss, J., & Olek, J. (2005). Statistical significance of the restrained slab test for quantifying plastic cracking in fiber reinforced concrete. *Journal of ASTM International*, 2(7), 1-18.

Rahmani, T., Kiani, B., Bakhshi, M., & Shekarchizadeh, M. (2012). Application of different fibers to reduce plastic shrinkage cracking of concrete. *7th RILEM International Conference on Cracking in Pavements*, Delft, Netherlands, June, 635-642.

Rose des vents, Montréal P. E. Trudeau, Annuel 1971-2000. (n.d.). Retrieved from http://www.climat-quebec.qc.ca/htdocs/data_fixe/rose_des_vents/RDVG_7025250.pdf

Saliba, J., Rozière, E., Grondin, F., & Loukili, A. (2011). Influence of shrinkage-reducing admixtures on plastic and long-term shrinkage. *Cement and Concrete Composites*, *33*(2), 209-217.

Scanlon, J. M. (1987). Controlling concrete during hot and cold weather. *ACI Special Publication, SP 104*: Lewis H. Tuthill International Symposium: Concrete and Concrete Construction. Editor, Grant T. Halvorsen; SP 104-13, 241-259.

Shaeles, C. A., & Hover, K. C. (1988). Influence of mix proportions and construction operations on plastic shrinkage cracking in thin slabs. *ACI Materials Journal*, *85*(6), 495-504.

Slowik, V., Schmidt, M., & Fritzsche, R. (2008). Capillary pressure in fresh cement-based materials and identification of the air entry value. *Cement and Concrete composites*, *30*(7), 557-565.

Soroushian, P., & Ravanbakhsh, S. (1998). Control of plastic shrinkage cracking with specialty cellulose fibers. *ACI Materials Journal*, *95*(4), 429-435.

Sutton, M. A., Orteu, J., & Schreier, H. W. (2009). Image correlation for shape, motion and deformation measurements. Springer, New York, DOI: 10.1007/978-0-387-78747-3.

Turcry, P., & Loukili, A. (2006). Evaluation of plastic shrinkage cracking of self-consolidating concrete. *ACI Materials Journal*, 103(4), 272-279.

Uno, P. J. (1998). Plastic shrinkage cracking and evaporation formulae. *ACI Materials Journal*, 95(4), 365-375.

Wang, K., Shah, S. P., & Phuaksuk, P. (2001). Plastic shrinkage cracking in concrete materials-influence of fly ash and fibers. *ACI Materials Journal*, 98(6), 458-464.

Wittmann, F. (1976). On the action of capillary pressure in fresh concrete. *Cement and Concrete Research*, 6(1), 49-56.

Yokoyama, K., Hiraishi, S., Kasai, Y., & Kishitani, K. (1994). Shrinkage and cracking of high-strength concrete and flowing concrete at early ages. *ACI Special Publication, SP 148: 4th CANME/ACI International Conference on Superplasticizers and Chemical Admixtures in Concrete*. Editor, V.M. Malhotra; SP 148-14, 243-258.

APPENDIX A

The MATLAB script developed to determine the crack area is presented in this section.

```
%% read image
I = imread('90.tif');
figure, imshow(I);
title('a. Original Image');
%% convert RGB image to grayscale image
Igray = rgb2gray(I);
figure, imshow(Igray);
title('b. Grayscale image');
%% convert grayscale image to binary image
level = 0.30;
Ithres = im2bw(Igray, level);
figure, imshow(Ithres);
title('c. Binary Image')
%% image morphological operation
Icomp = imcomplement(Ithres);
Iclean = bwareaopen(Icomp, 8);
figure, imshow(Iclean);
title('d. Cleaned Image')
%% calculate crack area
CrackPixels = bwarea(Iclean);
CalibrationArea = 50; % mm2
CalibrationPixels = 14613;
CrackArea = CrackPixels*CalibrationArea/CalibrationPixels; % mm2
```

APPENDIX B

The environmental variables and the water evaporation rates for each experiment are presented in this section.

Table B.1. Air and concrete temperatures, relative humidity, wind velocity, the mass of concrete, and the water evaporation rates calculated by mass loss and the water evaporation equation during the experiment for the concrete specimen without spray paint.

Time (min)	Air T (°C)	Concrete T (°C)	RH (%)	Wind V (m/s)	Mass of Concrete (g)	Evaporation Rate by Mass Loss (kg/m ² /h)	Evaporation Rate by Equation (kg/m ² /h)
0	34.8	25	35.4	9.8	7978.4	-	0.97
30	35.5	25	33.9	10.0	7940.5	1.08	1.01
60	35.8	25	34.0	9.6	7901.8	1.11	0.95
90	35.2	26	32.9	10.1	7866.1	1.02	1.22
120	37.6	27	28.4	10.1	7837.3	0.82	1.42
150	39.2	30	28.1	9.6	7813.3	0.69	1.74
180	36.7	32	28.9	10.2	7795.6	0.51	2.30
210	38.1	35	26.5	10.3	7782.9	0.36	2.92
240	39.4	37	25.5	9.7	7774.2	0.25	3.13
270	39.4	40	26.9	9.9	7767.9	0.18	3.75
300	36.1	42	30.9	10.0	7763.2	0.13	4.25
330	37.7	44	27.6	9.7	7759.2	0.11	4.65
360	38.1	45	26.3	9.8	7755.6	0.10	4.97

Table B.2. Air and concrete temperatures, relative humidity, wind velocity, the mass of concrete, and the water evaporation rates calculated by mass loss and the water evaporation equation during the experiment for the concrete specimen with spray paint.

Time (min)	Air T (°C)	Concrete T (°C)	RH (%)	Wind V (m/s)	Mass of Concrete (g)	Evaporation Rate by Mass Loss (kg/m ² /h)	Evaporation Rate by Equation (kg/m ² /h)
0	33.1	24	35.1	10.2	7988.1	-	0.99
30	35.0	24	33.6	10.4	7952.2	1.03	0.95
60	34.8	25	33.3	10.3	7917.1	1.00	1.10
90	36.3	26	31.4	9.9	7885.7	0.90	1.19
120	36.5	27	30.1	9.8	7858.7	0.77	1.37
150	38.7	28	28.3	10.3	7836.2	0.64	1.54
180	37.5	29	27.5	10.4	7818.3	0.51	1.83
210	36.2	31	30.6	10.5	7802.7	0.45	2.13
240	36.8	33	30.2	9.9	7789.0	0.39	2.35
270	35.2	35	30.5	10.4	7777.1	0.34	2.93
300	38.2	37	25.8	10.3	7766.6	0.30	3.35
330	37.3	38	27.6	10.3	7758.1	0.24	3.53
360	38.1	39	27.5	10.4	7751.3	0.19	3.74

Table B.3. Environmental variables and the water evaporation rates calculated by the water evaporation equation during the experiment for the cement paste specimen exposed to the room temperature.

Time (min)	Air T (°C)	Cement Paste T (°C)	RH (%)	Wind V (m/s)	Evaporation Rate by Equation (kg/m ² /h)
0	23.6	24.2	28.5	10.3	1.72
30	23.6	13.7	28.7	10.4	0.51
60	23.7	13.6	29.2	10.0	0.47
90	23.7	14.9	29.7	10.5	0.60

Table B.4. Environmental variables and the water evaporation rates calculated by the water evaporation equation during the experiment for the cement paste specimen exposed to the medium air temperature.

Time (min)	Air T (°C)	Cement Paste T (°C)	RH (%)	Wind V (m/s)	Evaporation Rate by Equation (kg/m ² /h)
0	33.2	24.5	21.0	10.2	1.60
30	33.3	15.3	20.7	10.2	0.51
60	32.5	15.4	21.9	10.0	0.50
90	31.8	19.1	21.7	9.9	0.91

Table B.5. Environmental variables and the water evaporation rates calculated by the water evaporation equation during the experiment for the cement paste specimen cast on No. 180 sandpaper, and exposed to the high air temperature and high wind velocity.

Time (min)	Air T (°C)	Cement Paste T (°C)	RH (%)	Wind V (m/s)	Evaporation Rate by Equation (kg/m ² /h)
0	43.2	26.2	10.9	9.6	1.89
30	41.4	21.1	12.7	9.8	1.20
60	42.5	27.5	11.9	9.8	2.08
90	43.2	30.4	11.5	10.0	2.59

Table B.6. Environmental variables and the water evaporation rates calculated by the water evaporation equation during the experiment for the cement paste specimen exposed to the low wind velocity.

Time (min)	Air T (°C)	Cement Paste T (°C)	RH (%)	Wind V (m/s)	Evaporation Rate by Equation (kg/m ² /h)
0	39.9	26.5	12.6	4.6	1.03
30	39.3	17.9	13.1	4.8	0.48
60	39.9	18.1	12.1	4.9	0.51
90	39.6	18.7	14.4	4.7	0.47

Table B.7. Environmental variables and the water evaporation rates calculated by the water evaporation equation during the experiment for the cement paste specimen exposed to the medium wind velocity.

Time (min)	Air T (°C)	Cement Paste T (°C)	RH (%)	Wind V (m/s)	Evaporation Rate by Equation (kg/m ² /h)
0	40.3	25.9	12.2	7.6	1.51
30	40.7	21.3	11.9	7.6	1.03
60	42.6	25.1	11.3	7.6	1.41
90	40.7	30.3	11.6	7.6	2.06

Table B.8. Environmental variables and the water evaporation rates calculated by the water evaporation equation during the experiment for the cement paste specimen with the w/c of 0.35.

Time (min)	Air T (°C)	Cement Paste T (°C)	RH (%)	Wind V (m/s)	Evaporation Rate by Equation (kg/m ² /h)
0	44.3	23.9	14.3	9.1	1.28
30	43.6	22.5	14.2	9.4	1.17
60	44.3	29.3	13.2	9.0	2.06
90	42.7	32.8	15.4	9.8	2.74

Table B.9. Environmental variables and the water evaporation rates calculated by the water evaporation equation during the experiment for the cement paste specimen with the w/c of 0.40.

Time (min)	Air T (°C)	Cement Paste T (°C)	RH (%)	Wind V (m/s)	Evaporation Rate by Equation (kg/m ² /h)
0	43.2	23.3	14.6	9.1	1.23
30	42.0	20.9	15.1	9.3	0.98
60	42.2	26.5	14.7	9.1	1.67
90	42.5	30.4	15.3	9.0	2.17

Table B.10. Environmental variables and the water evaporation rates calculated by the water evaporation equation during the experiment for the cement paste specimen with the w/c of 0.45.

Time (min)	Air T (°C)	Cement Paste T (°C)	RH (%)	Wind V (m/s)	Evaporation Rate by Equation (kg/m ² /h)
0	42.5	23.3	14.9	9.1	1.24
30	42.3	21.5	15.5	9.2	1.01
60	43.7	25.5	14.8	8.9	1.45
90	42.5	31.3	15.3	9.2	2.36

Table B.11. Environmental variables and the water evaporation rates calculated by the water evaporation equation during the experiment for the cement paste specimen with the w/c of 0.50.

Time (min)	Air T (°C)	Cement Paste T (°C)	RH (%)	Wind V (m/s)	Evaporation Rate by Equation (kg/m ² /h)
0	43.0	23.6	15.3	9.1	1.23
30	42.5	22.6	14.5	9.2	1.18
60	42.2	25.0	13.7	9.6	1.59
90	43.7	30.3	15.2	9.5	2.23

Table B.12. Environmental variables and the water evaporation rates calculated by the water evaporation equation during the experiment for the cement paste specimen cast on duct tape.

Time (min)	Air T (°C)	Cement Paste T (°C)	RH (%)	Wind V (m/s)	Evaporation Rate by Equation (kg/m ² /h)
0	40.2	25.9	11.9	9.8	1.90
30	40.9	21.1	12.9	9.6	1.18
60	39.1	27.6	11.9	9.7	2.16
90	40.7	29.8	11.5	9.9	2.53

Table B.13. Environmental variables and the water evaporation rates calculated by the water evaporation equation during the experiment for the cement paste specimen cast on No. 40 sandpaper.

Time (min)	Air T (°C)	Cement Paste T (°C)	RH (%)	Wind V (m/s)	Evaporation Rate by Equation (kg/m ² /h)
0	40.4	25.1	11.7	9.8	1.80
30	42.1	21.1	10.9	9.9	1.29
60	43.3	26.0	11.0	9.8	1.89
90	42.0	31.3	11.3	9.5	2.66